Disordered Granular Crystals



Alejandro Javier Martínez Ulloa
St Catherine's College
University of Oxford

Supervised by
Prof. Mason A. Porter

A thesis submitted for the degree of
Doctor of Philosophy

Trinity 2018

To my son Gaspar, my parents Alicia and Carlos, and my aunt Marta

Acknowledgements

I would like to thank my supervisor, Prof. M. A. Porter, for his encouragement, patience, support, and enthusiasm all along this crazy journey called D.Phil. Also, to Prof. P. G. Kevrekidis, from the Department of Mathematics and Statistics at University of Massachusetts (Amherst, USA), for helpful discussions and suggestions. I deeply appreciate his always very assertive and sharp comments. I am also thankful of Prof. Jinkyu Yang, Dr. Eunho Kim and Hiromi Yasuda from the William E. Boeing Department of Aeronautics & Astronautics at University of Washington (USA), for collaborating with this project and contributing with the experimental verification of some of the results of this thesis; Dr. Ch. Skokos, from the Department of Mathematics and Applied Mathematics at University of Cape Town (South Africa); Prof. S. Flach, from the Institute for Basic Science Daejeon (South Korea); Prof. A. Pikovsky, from the Department of Physics and Astronomy at Potsdam University (Germany); and Prof. M. I. Molina, from the Department of Physics at University of Chile (Chile), for suggesting useful references. I thank Prof. C. Daraio and Dr. C. Chong for hosting me during my visit to ETH in Zürich (Switzerland).

In a more personal branch, I would like to thank many good friends that were around during this process. I will start with Vladimirs, which is the closest friend I made during my time in Oxford. Everything began with our pints at Lamb & Flag and then reached its pinnacle with “wake me up before you go-go”. Sewook should also

be thanked here, I guess, so I thank him and wish him the best back in South Korea. Yair, Diego, and Gonzalo shared with me the same story. It was somehow fun, even though we were under a lot of stress. I thank John for being there, always open to talk about anything. Friends from Chile, there are many and I missed them a lot during my time in Oxford. Chago, Pedro, Pablo, Caro, Nico, and Memo, all of them have a special place in my life.

This work was supported partially by CONICYT (BCH72130485/2013).

Papers

The papers published during the period of the D.Phil. are enlisted below, as well as articles already submitted to scientific journals. Also, it is described which chapter of the present dissertation is based on each paper(s).

Articles directly related with the present dissertation:

1. **A. J. Martínez**, P. G. Kevrekidis, and M. A. Porter, "Superdiffusive Transport and Energy Localization in Disordered Granular Crystals", Physical Review E **93** (2), 022902 (2016). (Chapter 4 and Appendix A are based on this paper.)
2. **A. J. Martínez**, H. Yasuda, E. Kim, P. G. Kevrekidis, M. A. Porter, and J. Yang, "Scattering of waves by impurities in precompressed granular chains", Physical Review E **93** (5), 052224 (2016). (Chapter 3 is based on the theoretical part of this paper and Appendix B shows the experimental part.)
3. E. Kim, **A. J. Martínez**, S. E. Phenisee, J. Yang, M. A. Porter, and P. G. Kevrekidis, "Direct measurement of superdiffusive energy transport in disordered granular chains", Nature Communications **9**, 640 (2018). (Chapter 4 is based on the theoretical part of this paper and Appendix C shows the experimental part.)
4. **A. J. Martínez**, P. G. Kevrekidis, and M. A. Porter, "Quasiperiodic Granular Chains and Hofstadter Butterflies", Phil. Trans. Roy. Soc. A 376, 20170139 (2018), special issue on Nonlinear Energy Transfer in Dynamical and Acoustical Systems. (Chapter 5 is based on this paper.)

5. C. Chong, M. Molerón, **A. J. Martínez**, P. G. Kevrekidis, M. A. Porter, C. Daraio, "Nonlinear Excitations in Magnetic Lattices with Long-Range Interactions", New J. Phys. 21, 063032 (2019). (A simplify version of Appendix D is used in this paper.)

Articles produced during the D.Phil., but associated with other projects not directly related to the present dissertation:

1. **A. J. Martínez**, M. I. Molina, S. K. Turitsyn, and Y. S. Kivshar, "Nonlinear multi-core waveguiding structures with balanced gain and loss", Physical Review A **91** (2), 023822 (2015).
2. **A. J. Martínez** and Y. Zárate, "Spatial storage of discrete dark solitons", Journal of Optics **17** (4), 045506 (2015). Selected as paper of the week by Journal of Optics.

Conference proceedings:

1. D. Fuentealba, I. Soto, K. Liu, **A. J. Martínez**, "Tracking system with VLC for underground mine using multi-agent systems", First South American Colloquium on Visible Light Communications (SACVLC) (2017).

Abstract

Phenomena related to disorder and nonlinearity have been studied in many different context in physics, from condensed-matter physics to optics, with a substantial potential for applications. In particular, in mechanical systems, one can think of "smart" materials that adapt their properties, such as thermal conductivity or wave-transmission properties, depending on external stimuli, such as changes in pressure. It is the aim of this dissertation study transport and localization properties of one-dimensional disordered and quasiperiodic granular crystals as a function of an external precompression on the system. To archive this, we first study the scattering problem of a single impurity in a homogeneous granular chain and we demonstrate the existence of analogs to quantum resonances.

We then study spreading of initially localized excitations. We thereby investigate localization phenomena in strongly nonlinear systems, which are fundamentally different from such phenomena in linear and weakly nonlinear systems. We conduct a thorough comparison of wave dynamics in chains with three different types of disorder: an uncorrelated (Anderson-like) disorder and two types of correlated disorders (which are produced by random dimer arrangements). We find that, in most of the cases studied the behavior of the second moment m_2 and the inverse participation ratio P^{-1} for large times are given by $m_2 \sim t^{\gamma}$ and $P^{-1} \sim t^{-\eta}$. However, for low levels of precompression and initial perturbations on the displacement of the particles, we find out that there is not a clear trend for the second

moment. For an Anderson-like uncorrelated disorder, we find some regimes in the parameter space where a transition from subdiffusive ($\gamma < 1$) to superdiffusive ($\gamma > 1$) dynamics emerges depending on the amount of precompression in the chain. By contrast, for the correlated disorders, we find that the dynamics is superdiffusive for any precompression level. Additionally, for large precompression, the inverse participation ratio decreases slowly and the dynamics leads to partial localization around the initial wave. This localization phenomenon does not occur in the sonic vacuum regime, which yields that spontaneous localization is no longer possible.

We also study quasipediodic granular crystals, in particular, localization of waves in strongly precompressed granular chains induced by quasiperiodicity. We propose three different set-ups, inspired by the Aubry–André (AA) model, of quasiperiodic chains; and we use these models to compare the effects of on-site and off-site quasiperiodicity. When there is purely on-site quasiperiodicity, which we implement in two different ways, we show for a chain of spherical particles that there is a localization transition (as in the original AA model). However, we observe no localization transition in a chain of cylindrical particles in which we incorporate quasiperiodicity in the distribution of contact angles between adjacent cylinders by making the angle periodicity incommensurate with that of the chain. For each of our three models, we compute the Hofstadter spectrum and the associated Minkowski–Bouligand fractal dimension, and we demonstrate that the fractal dimension decreases as one approaches the localization transition (when it exists). We also show, using the chain of cylinders as an example, how to recover the Hofstadter spectrum from the system dynamics. Finally, in a suite of numerical computations, we demonstrate localization and also that there exist regimes of ballistic, superdiffusive, diffusive and subdiffusive transport.

Contents

1 INTRODUCTION **1**

1.1 Overview 1

1.2 Hertzian interaction 3

1.3 A brief introduction to Anderson localization 5

1.3.1 Anderson localization in the discrete Schrödinger equation 7

1.3.2 Breaking of Anderson localization due to weak nonlinearity 8

1.3.3 Anderson localization in other lattice models with on-site potentials 10

1.4 Outline of the dissertation 11

2 PRELIMINARY CONCEPTS IN GRANULAR CRYSTALS **13**

2.1 Linear, weakly nonlinear, and strongly nonlinear regimes 15

2.1.1 "Linear" regime ($\Delta_n \gg |u_{n-1} - u_n|$) 15

2.1.2 "Weakly nonlinear" regime ($\Delta_n > |u_{n-1} - u_n|$) 16

2.1.3 "Strongly nonlinear" regime ($\Delta_n \lessapprox |u_{n-1} - u_n|$) 17

2.2 Solitary waves 18

3 IMPURITIES IN GRANULAR CRYSTALS **20**

3.1 Introduction 20

3.2 Scattering between linear waves and impurities 21

3.3 Multiple impurities 27

3.4 Conclusions 31

4 DISORDERED GRANULAR CRYSTALS **33**
4.1 Types of disorder . . . 34
4.2 Correlations . . . 36
4.2.1 Anderson-like . . . 37
4.2.2 Random dimer model 1 . . . 38
4.2.3 Random dimer model 2 . . . 39
4.3 Physical parameters . . . 40
4.4 Numerical results . . . 40
4.4.1 Diagonalization of Eq. (2.12) . . . 41
4.4.2 Spreading and partial localization due to disorder and nonlinearity . . . 46
4.4.3 Energy distribution and second moment . . . 48
4.4.3.1 Displacement-perturbation initial conditions . . . 52
4.4.3.2 Velocity-perturbation initial conditions . . . 54
4.4.4 Transport arising from nonlinearity . . . 56
4.5 Conclusions . . . 59

5 QUASIPERIODIC GRANULAR CRYSTALS **70**
5.1 Introduction . . . 70
5.2 A brief review of the Aubry–André model . . . 71
5.3 Adding quasiperiodicity to granular chains . . . 73
5.3.1 On-site quasiperiodicity: two different variants of the AA model using spherical particles . . . 75
5.3.1.1 Model Ia: $\bar{\beta} \neq 0$ and $\bar{\alpha}_2 = \bar{\gamma} = 0$ . . . 75
5.3.1.2 Model Ib: $\bar{\gamma} \neq 0$ and $\bar{\alpha}_2 = \bar{\beta} = 0$ . . . 76
5.3.2 Off-site quasiperiodicity: the AA model with cylindrical particles . . . 77
5.3.2.1 Model II: $\bar{\alpha}_2 \neq 0$ and $\bar{\beta} = \bar{\gamma} = 0$ . . . 77
5.4 Linear approximation . . . 80
5.4.1 Linear spectrum and localization transition . . . 80
5.5 Hofstadter butterfly . . . 83

5.5.1 Recovering a Hofstadter butterfly from dynamics 85
5.6 Energy transport and localization 88
5.7 Conclusions 90

6 CONCLUSIONS AND FUTURE WORK 91

A SYMPLECTIC NUMERICAL INTEGRATION SCHEME 95
A.1 Comparison between $SABA_2C$ and a fourth-order Runge-Kutta . 99

B RAMSAUER–TOWNSEND EFFECT: EXPERIMENTS ON GRANULAR CRYSTALS 102
B.1 Numerical simulations 102
B.2 Experimental setup and diagnostics 106
B.3 Comparison between analytical, numerical, and experimental results 107

C TRANSPORT ON DISORDERED GRANULAR CRYSTALS: EXPERIMENTAL RESULTS 110

D DRIVEN DAMPED MAGNETIC CHAINS 117
D.1 Equations of motion 117
D.2 Physical quantities and estimation of the magnitude of the interactions 120

Bibliography 122

List of Figures

1.1 Example of a granular crystal with an impurity (marked with a red arrow). 2
1.2 Schematic of the contact interaction between two elastic spheres. . 5
1.3 Examples of different linear modes for the RDM1 model in Eq. (1.2). Panels (a), (b), and (d) correspond to localized states, whereas (c) is the extended mode in this system. 8

2.1 Dispersion relation (solid red curve) and group velocity (dashed blue curve) as a function of k for a homogeneous chain. We measure both quantities in units of $\sqrt{B/m}$. 17

3.1 Schematic of a homogeneous granular chain with (a) one impurity and (b) two contiguous impurities (i.e., a double impurity). The incident wave is characterized by I, the reflected wave is characterized by R, and the transmitted wave is characterized by T. We label the identities of the particles with integers. We calculate the parameters $B_{ij} = \frac{3}{2}A_{ij}^{2/3}F_0^{1/3}$ from the static precompression and the interactions between adjacent particles. 22
3.2 (a,c) Transmission and (b,d) reflection coefficients for the scattering of a plane wave in a chain with impurities as a function of the wavenumber k and the radius ratio α. We show examples for (a,b) a single impurity and (c,d) a double impurity. We describe the physical parameters of the particles in the chain in Table B.1. 24

3.3 Reflection coefficient $|R_{(ii)}|^2$ for a double impurity. The red dashed curves indicate the points at which the reflection coefficient is exactly 0. The resonant wavenumber k_r is given by Eq. (3.5). The blue dashed line highlights the critical value α_c. The system has a Ramsauer–Townsend (RT) resonance at wavenumber $k = \pm k_r$ for $\alpha > \alpha_c$. 26

3.4 Schematic of a host homogeneous granular chain with multiple double impurities. The incident wave is (I), the reflected wave is (R), and the transmitted wave is (T). We highlight impurities in turquoise boxes, and we indicate the scattering region with the dashed box. 28

3.5 (a) Space-time contour plot of the normalized velocity for a homogeneous chain with $N = 200$ particles and an excitation frequency of 3.0 kHz. (b) The same as panel (a), but with five double impurities located at positions $n = 50$, $n = 72$, $n = 90$, $n = 96$, and $n = 118$. The radius ratio is $\alpha = 1.5$, and arrows indicate the position of the impurities. Panels (c)–(e) show the velocity at particle $n = 130$ for excitation frequencies of (c) 2.0 kHz, (d) 3.0 kHz, and (e) 3.8 kHz. The black curves are associated with the homogeneous chain [panel (a)], and the red curves are associated with the chain with the impurities [panel (b)]. 30

4.1 Physical set-up related to Eq. (2.1) with boundary conditions given by Eqs. (4.1) and (4.2). 34

4.2 Examples of different types of disordered chains. (A) Anderson-like model, (RDM1) random dimer model 1, and (RDM2) random dimer model 2. The vertical dashed lines are for visual guidance to separate adjacent dimers from each other. 36

4.3 Correlation function $\rho_{n,n'}$ as a function of distance between particles for the three types of disordered granular chains: (a) Anderson-like model, (b) random dimer model 1, and (c,d) random dimer model 2. The gray curves show 100 realizations for $N = 100$ particles, and the black curves give the mean values. In panels (a)–(c), we use $q = 1/2$; in panel (d), we use $q = 4/5$. The horizontal dashed lines in panel (d) show the analytical value for the long-range correlation given by Eq. (4.11). 38

4.4 Linear spectrum and inverse participation ratio P^{-1} for different types of disorder with probability parameter $q = 0.5$ and size parameter $\xi = 0.5$. As usual, (A), (RDM1), and (RDM2) denote the Anderson-like, random dimer model 1, and random dimer model 2, respectively. The insets show examples of linear modes for both high and low frequencies. The dashed lines mark the cutoff frequency $f_i = \frac{1}{2\pi}\sqrt{\frac{4B_{ii}}{m_i}}$ associated with a homogeneous chain and the cutoff frequency $f_{bi} = \frac{1}{2\pi}\sqrt{\frac{2B_{12}}{m_i}}$ for a diatomic chain, where $m_3 = m_1 m_2/(m_1 + m_2)$. Using the parameter values described in Sec. 4.3 and $F_0 = 10$ N, we obtain $f_1 \approx 18.09$ kHz, $f_2 \approx 45.58$ kHz, $f_{b1} \approx 11.95$ kHz, $f_{b2} \approx 33.81$ kHz, and $f_{b3} \approx 35.86$ kHz. . . . 42

4.5 Inverse participation ratio (averaged over 100 chain configurations) as a function of the ratio $\xi = R_2/R_1$ and the mode number for different types of disordered chains and different values of the probability parameters q. The black regions are associated with delocalized waves. 43

4.6 (Left) On-site force as a function of time and (right) force distribution of particles for various amounts of precompression when we apply an excitation that consists of an initially localized displacement to the center of a homogeneous granular chain. In the left panels, the black curves give the force for particle 601, the blue curves give the force for particle 631, and the red curves give the force for particle 661. The chain has $N = 1201$ particles. For each example, the initial condition is $u_n = 10^{-1} \times \delta_{n,601}$ μm. For the right panels, we give the force in Newtons at time $t = 10^{-2}$ s. In each row, the two panels show results for a chain with the same specified precompression strength. 62

4.7 (Left) On-site force as a function of time and (right) force distribution of particles for various amounts of precompression when we apply an excitation that consists of an initially localized displacement to the center of an Anderson-like chain with a particle-size parameter of $\xi = 0.8$. In the left panels, the black curves give the force for particle 601, the blue curves give the force for particle 631, and the red curves give the force for particle 661. The chain has $N = 1201$ particles. For each example, the initial condition is $u_n = 10^{-1} \times \delta_{n,601}$ μm. For the right panels, we give the force in Newtons at time $t = 10^{-2}$ s. In each row, the two panels show results for a chain with the same specified precompression strength. 63

4.8 (First and third columns) Absolute values of the spatiotemporal energy distributions and (second and fourth columns) spectral density for the dynamics of an initially localized displacement perturbation $\{u_n(0), \dot{u}_n(0)\}_I = \{\alpha\, \delta_{n,801}, 0\}$, with $\alpha = 10^{-1}$ μm, for different amounts of precompression. The first two columns are for a homogeneous chain, and the last two columns are for an Anderson-like chain. Each chain has $N = 1601$ particles, though we only show the central 1201 particles in our plots of spatiotemporal energy distributions. For each example, the integration time is $T_{\max} = 10^{-2}$ s, and we give the force in units of Newtons. For each row, all panels are for a chain with the same specified precompression strength. 64

4.9 (First and third columns) Absolute values of the spatiotemporal energy distributions and (second and fourth columns) spectral density for the dynamics of an initially localized velocity perturbation $\{u_n(0), \dot{u}_n(0)\}_{II} = \{0, \beta\, \delta_{n,801}\}$, with $\beta = 8 \times 10^{-3}$ m/s, for different amounts of precompression. The first two columns are for a homogeneous chain, and the last two columns are for an Anderson-like chain. Each chain has $N = 1601$ particles, though we only show the central 1201 particles in our plots of spatiotemporal energy distributions. For each example, the integration time is $T_{\max} = 10^{-2}$ s, and we give the force in units of Newtons. For each row, all panels are for a chain with the same specified precompression strength. 65

4.10 Averaged energy distribution for different levels of precompression ($F_0 = 0$, 0.1, and 10 N) at $t = 10^{-2}$ s for Anderson-like chains. We averaged the energy profiles over 100 realizations and they are shown in log-scale, for $\xi = 0.5$, $q = 0.5$, and $N = 2501$. (a) displacement-perturbation initial condition: $\{u_n(0), \dot{u}_n(0)\}_I = \{\alpha\,\delta_{n,1251}, 0\}$, with $\alpha = 10^{-1}$ μm, and (b) velocity-perturbation initial condition: $\{u_n(0), \dot{u}_n(0)\}_I = \{0, \beta\,\delta_{n,1251}\}$, with $\beta = 8 \times 10^{-3}$ m/s. Dashed lines are the exponents for the exponential growth at the edge of the energy distribution. 66

4.11 Log-log plots of (left) the second moment and (right) IPR as a function of time. Each row is associated with a certain type of disorder (or lack thereof): "h" for a homogeneous chain, "A" for the Anderson-like chain, RDM1, and RDM2. In each panel, the colors and labels indicate different amounts of precompression F_0: (a, dashed black) 10 N, (b, solid red) 0.5 N, (c, dotted cyan) 0.1 N, (d, dash-dotted pink) 0.01 N, and (e, solid purple) 0 N. To guide the eye, we show slopes of 2 (ballistic transport) and 1 (diffusive transport) for the second moment $\tilde{m}_2$ and slopes of 0 and -1 for the IPR P^{-1}. In all cases, we use chains with $N = 2501$ spheres, and the initial condition is $\{u_n(0), \dot{u}_n(0)\}_I = \{\alpha\,\delta_{n,1251}, 0\}$, with $\alpha = 10^{-1}$ μm. For the Anderson-like, RDM1, and RDM2 chains, we use the parameter values $\xi = 0.5$ and $q = 0.5$, and we average over 500 different realizations of a disordered configuration in each case. The insets in the second, third, and fourth rows show the (discretized) logarithmic derivative of the second moment for $t \in [1, 10]$ ms. In the last row, we show exponents γ and η that we obtain for $t \in [4, 10]$ ms by fitting the data using the relations $\tilde{m}_2 \sim t^{\gamma}$ and $P^{-1} \sim t^{-\eta}$. 67

4.12 Log-log plots of (left) the second moment and (right) the IPR as a function of time. Each row is associated with a certain type of disorder (or lack thereof): "h" for a homogeneous chain, "A" for the Anderson-like chain, RDM1, and RDM2. In each panel, the colors and labels indicate different amounts of precompression F_0: (a, dashed black) 10 N, (b, solid red) 0.5 N, (c, dotted cyan) 0.1 N, (d, dash-dotted pink) 0.01 N, and (e, solid purple) 0 N. To guide the eye, we show slopes of 2 (ballistic transport) and 1 (diffusive transport) for the second moment $\tilde{m}_2$ and slopes of 0 and -1 for the IPR P^{-1}. In all cases, we use chains with $N = 2501$ spheres, and the initial condition is $\{u_n(0), \dot{u}_n(0)\}_{II} = \{0, \beta\,\delta_{n,1251}\}$, with $\beta = 8 \times 10^{-3}$ m/s. For the Anderson, RDM1, and RDM2 chains, we use the parameter values $\xi = 0.5$ and $q = 0.5$, and we average over 500 different realizations of a disordered configuration in each case. The insets in the second, third, and fourth rows show the (discretized) logarithmic derivative of the second moment for $t \in [1, 10]$ ms. In the last row, we show exponents γ and η that we obtain for $t \in [4, 10]$ ms by fitting the data using the relations $\tilde{m}_2 \sim t^{\gamma}$ and $P^{-1} \sim t^{-\eta}$. 68

5.1 Schematics of (a) model Ia and (b) model Ib. 75

5.2 (a) Interaction coefficient α_n for model II as a function of the contact angle ϕ_n between adjacent cylinders. In panels (b) and (c), we show the contact-angle distributions for two cases: (i) $\bar{\alpha}_1 = 3$ and $\bar{\alpha}_2 = 1$ and (ii) $\bar{\alpha}_1 = 3$ and $\bar{\alpha}_2 = 3$. We use arrows to represent the mapping process that we describe in the text. 78

5.3 (Top) Linear spectrum as a function of the quasiperiodicity parameter and (bottom) inverse participation ratio. We show our results for model Ia in the left column and for model Ib in the right column. 81

5.4 (Left) Localization transition as a function of $\bar{\beta}$ for the fundamental mode in model Ia. (Right) Inverse participation ratio P^{-1} as a function of $\bar{\alpha}_2 \in [0, 2]$ and $\bar{\alpha}_1 = 3$ for model II with $N = 100$ cylindrical particles. 83

5.5 Linear spectrum, in the form of a Hofstadter butterfly, as a function of ξ for (left) model Ia, (center) model Ib, and (right) model II. 84

5.6 (a) Example of the box-counting process that we use to compute the fractal dimension for model Ia and $\bar{\beta} = 2$. (b) Minkowski–Bouligand fractal dimension D_M as a function of the quasiperiodic parameter $\bar{\beta}$, $\bar{\gamma}$, and $\bar{\alpha}_2$ for models Ia, Ib, and II, respectively. We use the parameter value $\bar{\alpha}_1 = 3$ for model II. 85

5.7 Energy absorbed in model II for (top) $\bar{\alpha}_2 = 1$ and (bottom) $\bar{\alpha}_2 = 2$ (bottom panels). We use the parameter value $\bar{\alpha}_1 = 3$ in all cases. We show the absorbed energy on a linear scale in the left panels and on a logarithmic scale in the right panels. High intensity corresponds to large absorbed energy and hence frequencies in the pass band of the system, while low intensity, respectively, corresponds to frequencies in the band gaps of the system. 87

5.8 Diffusion exponent γ for (a) model Ia, (b) model Ib, and (c) model II as a function of the quasiperiodic parameters and ξ. 89

A.1 Average computation time over 100 realizations for a displacement initial condition in granular crystals with Anderson-like disorder. 101

A.2 Total energy as a function of time for (a) $SABA_2C$ and (b) RK4. 101

B.1 (a) Space-time contour plot of particle velocity profiles in a host 63-particle chain in which a double impurity has been inserted between particles -2 and $+1$. We use $\alpha = 1.5$ and the parameters in Table B.1 for this numerical simulation. Arrows (1) and (2) indicate the regions that we consider for the calculation of the transmission coefficient. These regions are not affected by the plane waves that reflect from the left or right walls. We also show velocity profiles for particles (b) $n = -27$ and (c) $n = +3$. The dots indicate the maximum and minimum peaks of oscillatory velocity profiles, and the domains of (1) and (2) correspond to the temporal regions marked with (1) and (2) in panel (a). 104

B.2 Schematic of the experimental setup for a granular chain with a single impurity. In the inset, we show an image of the experimental setup. 105

B.3 Transmission of plane waves in a granular chain with impurities. The radius ratio of the impurity radius to the host particle radius in the host chain is (left) $\alpha = 0.7$ and (right) $\alpha = 1.5$. Results for chains with (top) a single impurity and (bottom) a double impurity. 108

C.1 Schematic of the experimental setup. The inset shows details of the boundary condition in the front of a granular chain. 111

C.2 Wave propagation in homogeneous and disordered chains. Spatiotemporal distributions of particle velocities in (a–c) a homogeneous chain and (d–f) a disordered chain with static precompressions of (a, d) 0 N, (b, e) 10 N, and (c, f) 50 N. 111

C.3 Experimental observation of Anderson-like localization. Normalized kinetic energy profile, averaged between 1.5 ms and 3.5 ms, for different levels of precompression. In the inset, we show the kinetic energy on a logarithmic scale when the static precompression is 50 N. The dashed line shows the slope associated with $e^{-0.54i}$, where i denotes particle number. 113

C.4 Inverse participation ratio (P^{-1}) of the kinetic energy in homogeneous (blue curves) and disordered (red curves) chains for (a) linear and (b) nonlinear regimes. In both cases, we compare numerical calculations (dashed curves) with experimental data (solid curves). 114

C.5 Exponents (γ) of the second moment m_2 of kinetic energy as a function of precompression strength. The exponents 1 and 2 (horizontal dashed lines) represent diffusive and ballistic transport, respectively. The diamond, triangular, and square marks are based on experimental data obtained, respectively, from a homogeneous tungsten-carbide (WC) chain, a homogeneous aluminum (Al) chain, and a mean over five disordered chains. We mark the numerical data with circles. We do computations for homogeneous chains (blue circles), the five disordered chains (hollow red circles), and 100 randomly generated disordered chains (red circles with error bars). 115

D.1 (a) Scheme for the chain of magnets. (b) Scheme for the interaction between the magnetic field generated by the current on the wire and the magnets in the chain. 118

D.2 Magnetic driving. 119

D.3 Total force at $t = 0$ over a magnet with equilibrium position (before driving) exactly below to the wire and between two fixed magnets positioned at $x = -\delta_0$ and $x = \delta_0$. 120

D.4 Force map as a function of time and the position for a magnet between two fixed magnets positioned at $x = -\delta_0$ and $x = \delta_0$. (a) Hamiltonian case. (b) Forced case. 120

Chapter 1

INTRODUCTION

1.1 Overview

Granular crystals, as their name suggests, are systems similar to crystalline solids, but they are made from macroscopic grains instead of atoms or molecules. Even though they are not restricted to be one-dimensional (1D), one already gets interesting phenomena in 1D granular crystals. This consists of closely packed chains of elastically colliding particles (see Fig. 1.1). Because of the contact interaction between particles, the dynamics are characterized by a strongly nonlinear response, and the system provides a paradigmatic example for the investigation of chains of strongly nonlinear oscillators. This has motivated a significant number of studies of the interplay between nonlinearity and discreteness [121, 142] and it has inspired the exploration of a diverse set of coherent structures, including traveling waves, breathers, and dispersive shock waves [73, 142]. In this context, the use of ultrasonic sources has shown remarkable results at generating traveling waves and other type of structures at harmonic and subharmonic frequencies [32, 33, 34, 60]. Numerous potential engineering applications have been explored using granular crystals [132]. A few examples include shock and energy absorbing layers [24, 41, 55], sound-focusing devices and delay lines [147], actuators [76], vibration absorption layers [52], sound scramblers [26, 122], and acoustic switches and logic gates [98]. Furthermore, in the context of three-dimensional (3D) elastic networks, localization of ultrasonic waves has

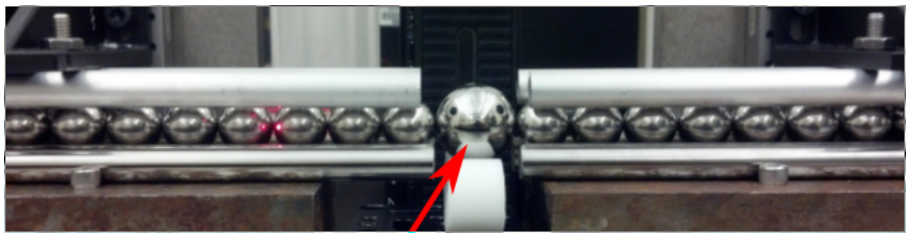


Figure 1.1: Example of a granular crystal with an impurity (marked with a red arrow).

been detected [58], showing the possibility to adapt fundamental results from condensed-matter physics into mechanical systems. Moreover, because one can model granular chains as a type of Fermi–Pasta–Ulam (FPU) lattice, they have also been employed in studies of phenomena such as equipartition (see, e.g., [149, 159]).

Additionally, because of the advances in materials engineering, granular crystals can be created from numerous material types and sizes, which leads to significant versatility and makes their properties extremely tunable [22, 25, 121, 142]. They thus provide an excellent testbed for investigating the effects of structural and material heterogeneities on nonlinear wave dynamics. Some of the recent studies in granular crystals involve the role of defects [50, 56], interfaces between two different types of particles [24, 122], decorated and/or tapered chains [29, 49], chains of diatomic and triatomic units [52, 115, 130, 131], and quasiperiodic and random configurations [17, 41, 146].

For these reasons, the study of disordered granular crystals is also becoming increasingly popular. Important themes in such studies have been transport properties of wavepackets and solitary waves and the interplay between disorder (especially in the context of Anderson localization), discreteness, and nonlinearity [2, 107, 128, 156]. These themes are also relevant to a wide variety of other nonlinear lattice models [38, 88]. To achieve a thorough understanding of such phenomena, it is crucial to consider the scattering properties of waves when they encounter impurities or other inhomogenities.

Note that, the word *crystal* traditionally refers to a periodic structure, but in

this thesis we will use the term *granular crystal* (or simply *granular chain*) in a more general way for systems that can be either periodic or aperiodic, composed by spherical grains interacting through a Hertzian force (although in Chapter 5 we also discuss the case of cylindrical particles), and such that their dynamics are restricted to 1D.

In the following section, we describe a derivation of the force between colliding particles, which is the base of any study in granular crystals. Then, we introduce the concept of Anderson localization and discuss it in its original formulation and also applied in other lattice models.

1.2 Hertzian interaction

Contact interactions have been a subject of research for over a century [70]. In 1882, it was Heinrich Hertz who first described the stress at the contact of two elastic and curved solids [129]. Hertz established that, to solve the problem, it was necessary to find the distribution pressure transmitted between the bodies. This distribution has to be such that the resulting elastic displacements on the surface of the solids satisfy

$$u_1 + u_2 = d - Ax^2 - By^2 \ \text{(within the contact area)}, \tag{1.1}$$

$$u_1 + u_2 > d - Ax^2 - By^2 \ \text{(outside the contact area)}, \tag{1.2}$$

where u_1 and u_2 are the displacements relative to the undeformed bodies, d is the absolute deformation, and A and B are geometric parameters. For spherical particles $A = B = \frac{1}{2}\left(\frac{1}{R_1} + \frac{1}{R_1}\right)$. In Fig. 1.2, we show a schematic for two interacting spheres. Considering small deformations (i.e., $d \ll a$, where a is the characteristic contact length as shown in Fig. 1.2), and assuming that the contacting particles are spherical, it is possible to estimate the mean contact pressure $\bar{p}$ acting symmetrically on each solid by

$$\frac{\bar{p}(1-\nu_1)}{E_1} + \frac{\bar{p}(1-\nu_2)}{E_2} \propto a\left(\frac{1}{R_1} + \frac{1}{R_2}\right), \tag{1.3}$$

where E_1 and E_2 are the elastic moduli, and ν_1 and ν_2 are the Poisson ratios. Hertzian theory gives a pressure distribution of $p(r) = \bar{p}\,[1-(r/a)^2]^{1/2}$. Thus, the total load per unit axial length P is

$$P = \int_0^a p(r)\, 2\pi r\, dr = \frac{2}{3}\bar{p}\,\pi a^2\,. \tag{1.4}$$

Combining equations (1.3) and (1.4), it is possible to estimate the contact area a and the mean pressure $\bar{p}$ as

$$a \;\propto\; \left[\frac{P}{E_1 E_2}\left(\frac{E_1(1-\nu_2^2)+E_2(1-\nu_1^2)}{1/R_1+1/R_2}\right)\right]^{1/3}, \tag{1.5}$$

$$\bar{p} \;\propto\; \left[P E_1^2 E_2^2\left(\frac{1/R_1+1/R_2}{E_1(1-\nu_2^2)+E_2(1-\nu_1^2)}\right)^2\right]^{1/3}, \tag{1.6}$$

which show that both quantities grow as the cube root of the load. More importantly for us, for spheres, it is also possible to estimate the absolute deformation d by

$$d \propto \left[\left(\frac{P}{E_1 E_2}\right)^2\left(\frac{\left[E_1(1-\nu_2^2)+E_2(1-\nu_1^2)\right]^2}{1/R_1+1/R_2}\right)\right]^{1/3}, \tag{1.7}$$

which grows proportionally to the load to the power of 2/3. This is what is known as the *Hertzian law* [70] for contact interactions.

From here, we can estimate the repulsive force F between elastic objects. To illustrate a Hertzian interaction, the magnitude of F between an elastic plate and an elastic sphere of radio R is given by

$$F = \frac{4}{3}\,\langle E\rangle\, R^{1/2} d^{3/2}\,, \tag{1.8}$$

where $\langle E\rangle = \frac{E_1 E_2}{(1-\nu_1^2)E_2+(1-\nu_2^2)E_1}$.

Although Hertz's work represented significant progress on rigid-body descriptions of the contact interactions, its theory includes some simplifications and restrictions that must be taken into consideration. Considering the significant dimension of the contact area as a, the relative radius of curvature as R, the significant radii of each body as R_1 and R_2, and the significant dimension of the absolute deformation as d, the assumptions made in the Hertz theory are

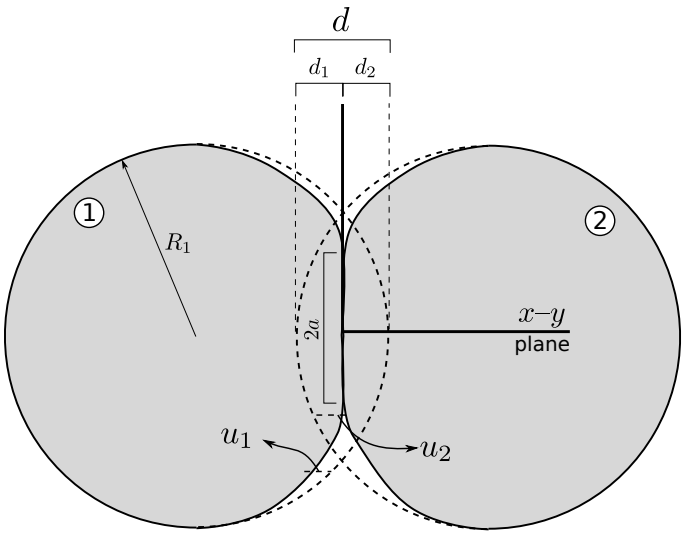


Figure 1.2: Schematic of the contact interaction between two elastic spheres.

as follows: (i) the surfaces are continuous and non-conforming; (ii) the strains are small enough so the interactions are elastic, which requires $a \ll R$; (iii) each solid can be considered as an elastic half-space, which implies that $a \ll R_{1,2}$ and $a \ll d$; (iv) the surfaces are frictionless. It is important to notice that Hertz theory only takes into account elastic interactions, which leads to three additional assumptions: (v) the surfaces are non-adhesive, (vi) dissipative effects are not considered, and (vii) energy that dissipates into internal degrees of freedom can be neglected.

1.3 A brief introduction to Anderson localization

Wave propagation in disordered media has been the subject of extensive research for at least half a century [1], starting especially with the seminal article by Philip W. Anderson[1] in the context of condensed-matter physics [3]. In this context, an electron immersed in a perfect crystal — i.e., a perfectly periodic potential with no defects — behaves in such a way that its wave function can be considered

[1]P. W. Anderson, with N. Mott and J. van Vleck, was awarded the 1977 Nobel Prize in Physics for his work on the electronic structure of magnetic and disordered systems.

a periodic function of space, with the same period of the crystal. This leads to the conductance of electrons. However, if the crystal has imperfections, the translational invariance is broken, and scattering appears due to the defects; this decreases the conductivity. Additionally, counterintuitive phenomena emerge when there is a random distribution of defects, which can be understood as a randomly distributed external potential acting on the electron. In particular, P. W. Anderson showed theoretically that the diffusion of waves is curtailed in linear media that contain sufficient randomness induced by defects or impurities. Electrons become spatially localized, and the conductivity can even vanish. This effect depends on several specific aspects of the disorder and the systems. Thus, not all disordered systems have all of their electronic states localized, and it was Sir N. Mott, in the 1960s, who introduced the notion of a "mobility edge", which separates the region of localized and extended states in the linear spectrum. This mobility edge can arise from different mechanisms: finite-size effects, correlations of the disorder, dimension of the system, among others.

Some of the most prominent recent studies of wave propagation in disordered media have generalized the ideas of P. W. Anderson to weakly nonlinear settings [8, 21, 31, 46, 48, 141, 135]. However, our main goal in this thesis departs somewhat from this thread, as we seek to investigate transport and localization in *strongly nonlinear* media. This is a key challenge in the study of nonlinear chains [84, 116, 144]. In general, localization in strongly nonlinear systems can be fundamentally different than localization in linear and weakly nonlinear systems [128]. There are numerous types of disorder, and — as we illustrate in this thesis — it matters whether the disorder is uncorrelated (as in the original Anderson model) or correlated. Moreover, there are multiple types of possible correlations in disordered arrangements, and we illustrate using randomized arrangements of dimers that seemingly small differences in disorder can have a large impact on the dynamics of wave propagation.

1.3.1 Anderson localization in the discrete Schrödinger equation

In the simplest approximation (called the tight-binding approximation [72]), the wavefunction associated with an electron in a lattice can be described by a discrete Schrödinger (DS) equation. In the case of a one-dimensional lattice, it can be written as [72]

$$-i\frac{d\psi_n}{dt} = \epsilon_n\psi_n + (\psi_{n+1} + \psi_{n-1})\,, \tag{1.9}$$

where $\psi_n(t)$ is the probability amplitude of finding the excitation in the site n at time t and ϵ_n is the called *site energy* on the nth site. Equation (1.9) has an associated eigenvalue problem of the form

$$E_m\Psi_m = \Lambda\Psi_m\,, \tag{1.10}$$

which plays the role of a time-independent DS equation. The quantities E_m are the energy levels ($m \in \{1,\ldots,N\}$) (i.e., the linear spectrum), and $\Psi_m = \{\psi_1^{(m)},\ldots,\psi_N^{(m)}\}$ is the eigenfunction (also called *linear mode*) associated with the energy E_m, $\Lambda_{n,m} = \epsilon_n\delta_{n,m} + \delta_{n+1,m} + \delta_{n-1,m}$, and N is the total number of sites in the system. We say that a mode is *exponentially localized* (or simply *localized*) when $|\psi_n| \leq Ce^{-|n|\lambda}$ as $n \to \infty$ (with $\lambda > 0$ and C a real number). In this context, *Anderson localization* corresponds to the linear phenomenon where, given ϵ_n distributed in a totally random way (uncorrelated), all of the linear modes Ψ_m of Eq. (1.10) become exponentially localized as $N \to \infty$. The tail of the modes satisfy $\psi_n \sim e^{-\lambda_E|n-n_0|}$ (with $\lambda_E > 0$ for all E) as $n \to \infty$, and they are called *Anderson modes*. This implies that the corresponding dynamics, given any initially localized condition, are given by the superposition of only few of these Anderson modes. Consequently, the probability amplitude remains localized.

Dunlap et. al. [30] introduced a *random dimer model* (RDM1, according to terminology in Chapter 4), which consists of a random selection of the site energy ϵ_n. However, instead of individually setting the value for each site of the lattice,

pairs of adjacent sites (dimers) are constrained to have the same site energy.[2] The most interesting aspect of this slightly different type of disorder, in comparison with Anderson disorder, is that most of the linear modes of equation (1.10) are spatially localized, as Anderson modes, and only one of them is extended. We show an example of this phenomenon in Fig. 1.3. This has as consequence that any initial condition that has this extended mode as one of its components will transport energy across the lattice.

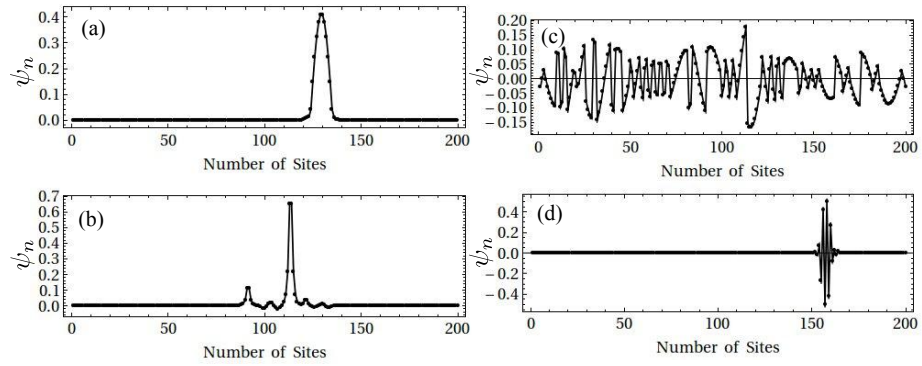


Figure 1.3: Examples of different linear modes for the RDM1 model in Eq. (1.2). Panels (a), (b), and (d) correspond to localized states, whereas (c) is the extended mode in this system.

1.3.2 Breaking of Anderson localization due to weak nonlinearity

Depending on the system, nonlinearity can arise in many different ways. In particular, the case of Eq. (1.9) with a cubic nonlinearity[3] has been researched extensively in the context of disordered nonlinear lattices as a prototypical model for the study of competition between discreteness, disorder, and nonlinearity [4, 38, 42, 69, 87, 88, 127, 152, 153] during the last decades. This has been mainly because of the vast number of physical systems that can be described by such equations, in optics, condensed matter, and more [72]. This

[2]In Chapter 4, we give a detailed discussion of the construction rule, and the correlation properties of this type of disorder and all other types of disorder that we examine in this thesis.

[3]In this case, the dynamics depends on the norm $|\psi_n|^2$ of the wavefunction.

case illustrates the effect of weak nonlinearity in disordered chains. The discrete nonlinear Schrödinger (DNLS) equation is given by [72]

$$-i\frac{d\psi_n}{dt} = \epsilon_n\psi_n + (\psi_{n+1} + \psi_{n-1}) + |\psi_n|^2\psi_n\,, \tag{1.11}$$

and it is known for supporting nonlinear localized solutions in the form of *discrete solitons*.[4] These solutions exist above a certain nonlinear threshold [118] in both disordered and homogeneous lattices, so they can be excited dynamically only for certain initial conditions, such as when the amplitude is large enough and through a phenomenon called *self-trapping*. Thus, one can expect that Eq. (1.11) has solutions that exhibit dynamical localization at low amplitudes due to Anderson-like localization, and at high amplitudes as well due to self-trapping dynamics. However, the situation is much more complicated for waves with intermediate amplitudes. When the nonlinearity is small enough — i.e. before self-trapping occurs — even when the site energies are distributed completely at random (as in the Anderson case), a breaking of Anderson localization can be observed. By this, we mean that the energy is no longer completely trapped in the form of Anderson modes, energy spreads slowly because of the interactions between Anderson modes induced from the nonlinearity. To understand this, we expand $\psi_n(t)$ into eigenfunctions, $\psi_n(t) = \sum_{m=1}^{N}\phi_{n,m}\Phi_m(t)$, with $\phi_{n,m} \in \mathbb{R}$. Using the fact $\langle\phi_m|\phi_l\rangle = \sum_{n=1}^{N}\phi_{n,m}\phi_{n,l} = \delta_{m,l}$, we write Eq. (1.11) as

$$i\frac{d\Phi_\nu}{dt} + E_\nu\Phi_\nu + \sum_{\nu_1\nu_2\nu_3} I_{\nu\nu_1\nu_2\nu_3}\Phi^*_{\nu_1}\Phi_{\nu_2}\Phi_{\nu_3} = 0\,, \tag{1.12}$$

where E_ν is the eigenvalue associated with the eigenfunction ϕ_ν, and the overlap integral is

$$I_{\nu\nu_1\nu_2\nu_3} = \sum_n \phi_{n,\nu}\phi_{n,\nu_1}\phi_{n,\nu_2}\phi_{n,\nu_3}\,. \tag{1.13}$$

From Eq. (1.12), we note that the interaction depends on the overlap between different eigenfunctions; this is described by the overlap integral. Thus, unless $I_{\nu\nu_1\nu_2\nu_3} = 0$ for all $\{\nu, \nu_1, \nu_2\,\nu_3\}$, there will always be some fraction of energy

[4] A discrete soliton is a nonlinear solution of Eq. (1.11) of the form $\psi_n(t) = \phi_n e^{-\mathrm{i}\omega t}$, with $\omega = \omega(\{\phi_n\}) \in \mathbb{R}$ and ϕ_n exponentially localized.

spreading between different modes of the system as a consequence of the presence of nonlinearity.

1.3.3 Anderson localization in other lattice models with on-site potentials

Another lattice model that has been popular in the literature of discrete nonlinear disordered lattices is the one known as Klein-Gordon lattice (KG). In 1D, the equations of motion read as

$$\frac{d^2\psi_n}{dt^2} = -\bar{\epsilon}_n\psi_n + (\psi_{n+1} + \psi_{n-1} - 2\psi_n)\,. \tag{1.14}$$

Interestingly, the eigenvalue problem for this model is equivalent to the one stated in Eq. (1.10). Consequently, the results obtained for DS equations can be mapped to KG straightforwardly. Similarly as with DS lattices, many results for KG lattices in its nonlinear form:

$$\frac{d^2\psi_n}{dt^2} = -\bar{\epsilon}_n\psi_n - \psi_n^3 + (\psi_{n+1} + \psi_{n-1} - 2\psi_n)\,, \tag{1.15}$$

have been found, such as breaking of Anderson localization, emergence of weak and strong chaos, among others [38, 88].

Furthermore, in a strongly nonlinear chain the interactions between different elements are given by nonlinear functions that vanish in the linear limit. Most of the work on this type of system has been done for periodic chains —examples of this are monoatomic or diatomic chains— and just a few articles discuss disordered situation. For example, Mulansky et. al. examined energy spreading in a kind of strongly nonlinear disordered lattices with local linear and nonlinear potentials [117]. They studied the scaling properties of the energy spreading numerically and with partial differential equation (PDE) approximations. However, they do not observe any phenomena similar to Anderson localization. Additionally, Ponson et. al. studied the transmission of waves along granular chains in the presence of correlated disorder [128]. In this case, the transmission depends strongly on the type and specific properties of the disorder. Moreover, below a

certain level of disorder, the energy is carried mainly by solitary waves; by contrast, above this level, the transmitted force saturates and the energy is carried by a train of small waves. In this case, they only observe transport, but nothing as Anderson localization.

1.4 Outline of the dissertation

The remainder of this thesis is organized as follows. In Chapter 2, we introduce preliminary concepts, different dynamical regimes, and solutions that are well-known for homogeneous granular crystals. In Chapter 3, we analyze the scattering process between linear plane waves and impurities, and we state its connection with transport in disordered linear systems. We also demonstrate that it is possible to construct a classical analog of the Ramsauer–Townsend effect, corresponding to a quantum resonance in electronic systems, in granular crystals. In Chapter 4, we introduce three different types of disorder and study their correlation properties. We describe the fundamental equations that characterize a disordered granular chain with Hertzian interactions, and we discuss different approximations that depend on the amount of precompression in the system. We present our numerical results, describe the fundamental differences between each type of disorder, and discuss the properties of the linear spectrum and the different types of impurity-like modes that appear for each type of disorder. We show that surface modes are supported by the system and that their frequencies are isolated in the spectrum. We also study the transport and localization properties for both linear and nonlinear waves for each type of disorder, and we show that localization is no longer possible in a strongly nonlinear regime. Chapters 5 is devoted to the study of a different kind of granular crystals, which are neither ordered nor disordered, called *quasiperiodic crystals*. These chains are generated by setting one of the physical parameters to be modulated in space, with a modulation period incommensurable with the natural period of the crystal. In particular, we study different variants of quasiperiodic granular crystals

inspired in the Aubry–André model. We consider different plausible experimental set-ups. We show that localization transitions, where linear modes transition from being extended to being localized, can arise for specific parameters. Additionally, variants of the Hofstadter butterfly are observed, this illustrates the fractal nature of the frequency spectrum. We also analyze transport properties by studying the effects of nonlinearity over the different localization regimes. We conclude in Chapter 6, where we also discuss future challenges in granular crystals.

Finally, we include four appendices. In Appendix A, we expose our symplectic algorithm and compare it with traditional a Runge-Kutta algorithm. Appendices B and C are dedicated to experimental measures of the results presented in Chapters 3 and 4. In Appendix D, we discuss a different model, where elastic particles are replaced by magnetic dipoles, and we discuss its equations of motion and physical parameters.

Chapter 2

PRELIMINARY CONCEPTS IN GRANULAR CRYSTALS

As introduced in Chapter 1, a 1D granular crystal composed of N spherical beads can be described as a chain of nonlinear coupled oscillators with Hertzian interactions between each pair of particles [121, 142]. The system is thus modeled using the following equations of motion:

$$m_n\ddot{u}_n = A_n[\Delta_n + u_{n-1} - u_n]_+^{3/2} - A_{n+1}[\Delta_{n+1} + u_n - u_{n+1}]_+^{3/2}\,, \tag{2.1}$$

where u_n is the displacement of the nth particle (where $n \in \{1, 2, \ldots, N\}$) measured from its equilibrium position in the initially compressed chain, m_n is the mass of the nth particle,

$$\Delta_n = \left(\frac{F_0}{A_n}\right)^{2/3} \tag{2.2}$$

is a static displacement for each bead that arises from the static load $F_0 = \text{const}$,

$$A_n = \frac{4E_{n-1}E_n\left(\frac{R_{n-1}R_n}{R_{n-1}+R_n}\right)^{1/2}}{3\left[E_n(1-\nu_{n-1}^2) + E_{n-1}(1-\nu_n^2)\right]}\,, \tag{2.3}$$

and the bracket $[\cdot]_+$ is defined as

$$[x]_+ = \begin{cases} x\,, & \text{if} \quad x > 0 \\ 0\,, & \text{if} \quad x \leq 0 \end{cases}\,. \tag{2.4}$$

The exponent 3/2 and prefactor A_n in Eq. (2.1) are consequences of the elastic nature of the particle interactions and from the spherical geometry [121, 142],

and these come from Eq. (1.8). Other particle shapes, such as ellipsoids [124] and cylindrical particles [75], also have Hertzian interactions.

We consider a chain that is compressed initially by two plates placed at the boundaries. This yields the following boundary conditions:

$$u_0 = \psi_l(t)\,, \tag{2.5}$$

$$u_{N+1} = \psi_r(t)\,. \tag{2.6}$$

In most of the cases, we will consider the plates to be static in time, i.e. $\psi_l(t) = \psi_r(t) = 0$ for all t. However, in some specific points of the thesis, such as Sections 5.5.1 and Appendix B, we apply a periodic driving in one of the boundaries in the form of $\psi_l(t) = d\sin(2\pi ft)$, where d and f, respectively, are the amplitude and frequency of the external driving.

Furthermore, in most cases we will be interested in chains composed of one or two type of particles. For instance, in Chapter 3, we study scattering of waves with impurities. In this case, an impurity is basically a particle, or few particles, that are different from the majority of the particles in the chain. In that case their radii of the particles is different. We call these two types of particles: type-1 and type-2 particles. Thus, the interaction parameter A_n can take one of four possible values (depending on the type of spheres that are in contact). These values are

$$A_n = \begin{cases} A_{11} \equiv \frac{E_1(2r_1)^{1/2}}{3(1-\nu_1^2)}\,, & \text{(type-1, type-1)} \\ A_{12} \equiv \frac{4E_1E_2\left(\frac{r_1r_2}{r_1+r_2}\right)^{1/2}}{3\left[E_1(1-\nu_2^2)+E_2(1-\nu_1^2)\right]}\,, & \text{(type-1, type-2)} \\ A_{22} \equiv \frac{E_2(2r_2)^{1/2}}{3(1-\nu_2^2)}\,, & \text{(type-2, type-2)} \\ \frac{2E_1r_1^{1/2}}{3(1-\nu_1^2)}\,, & \text{(type-1, wall)} \end{cases}, \tag{2.7}$$

where $E_{1,2}$, $\nu_{1,2}$, and $r_{1,2}$ are, respectively, the elastic modulus, the Poisson ratio, and the radii of the type-1 and type-2 particles. The particle masses are m_1 and m_2. We assume that the mechanical properties of the elastic plates at the boundaries are the same as for type-1 particles. The radius of an impurity particle is $r_2 = \alpha r_1$, where $\alpha > 0$ is the ratio between the radii of the two

types of spheres. If we assume that type-1 and type-2 particles have identical densities (i.e., $\rho_1 = \rho_2$), then $\alpha < 1$ implies that the impurities are lighter than the particles in the host homogeneous chain, whereas $\alpha > 1$ implies that the impurities are heavier.

2.1 Linear, weakly nonlinear, and strongly nonlinear regimes

Changing the magnitude of the static load F_0 relative to the displacements $|u_n - u_{n+1}|$ between particles makes it possible to tune the strength of the nonlinearity in Eq. (2.1). To do this, we approximate the force using a power-series expansion, which is suitable for a strongly compressed chain [121]. We thereby distinguish three dynamical regimes, which we now discuss.

2.1.1 "Linear" regime ($\Delta_n \gg |u_{n-1} - u_n|$)

In this regime, we linearize Eq. (2.1) about the equilibrium state in the presence of precompression to obtain

$$m_n \ddot{u}_n = B_n u_{n-1} + B_{n+1} u_{n+1} - (B_n + B_{n+1}) u_i \,, \tag{2.8}$$

where

$$B_n = \frac{3}{2} A_n \Delta_n^{1/2} = \frac{3}{2} A_n^{2/3} F_0^{1/3} \propto R^{1/3}. \tag{2.9}$$

The linear regime corresponds to a chain of coupled harmonic oscillators. We represent the solutions to Eq. (2.8) as complex wavefunctions to obtain a complete set of eigenfunctions of the form $u_n = v_n e^{\mathrm{i}\omega t}$, where ω is the eigenfrequency (so the eigenvalue is $\lambda = -\omega^2$). In the homogeneous case (i.e., for $B_n = B$ and $m_n = m$ for all n), we obtain plane waves $v_n = e^{\mathrm{i}kn}$, and the dispersion relation corresponds to a single acoustic branch, which is given by

$$\omega = 2\pi f = \sqrt{\frac{2B}{m} \left[1 - \cos(k)\right]} \,. \tag{2.10}$$

The frequency satisfies the bounds $\omega \geq \omega_0 = 0$ and $\omega \leq \Omega = \sqrt{\frac{4B}{m}}$, and the group velocity in this homogeneous case is

$$v_g = \frac{\partial \omega}{\partial k} = \sqrt{\frac{B}{2m}} \frac{\sin(k)}{\sqrt{1-\cos(k)}}\,. \tag{2.11}$$

Figure 2.1 shows the dispersion relation and the group velocity for a homogeneous crystal as a function of the wavenumber k. The maximum of the group velocity is $v_g^m = \sqrt{B/m} = \Omega/2$, and it occurs when $k = 0$. The maximum of the group velocity is close to $k = 0$, so low-frequency waves spread faster than high-frequency ones.

When we consider an arbitrary arrangement of spheres in a granular crystal, the eigenvalue problem associated with Eq. (2.8) takes the generic form

$$\lambda \mathbf{v} = \Lambda \mathbf{v}\,, \tag{2.12}$$

where $\lambda = -\omega^2$ is the eigenvalue and $\Lambda = \mathbf{M}^{-1}\mathbf{B}$, where $\mathbf{M}_{i,j} = m_i \delta_{i,j}$ is a diagonal matrix of masses and

$$\mathbf{B}_{i,j} = B_{i+1}\delta_{i,j-1} + B_i \delta_{i,j+1} - [B_i + B_{i+1}]\delta_{i,j}$$

is a tridiagonal symmetric matrix. Both matrices $\mathbf{M}$ and $\mathbf{B}$ have random entries and in general the commutator satisfies $[\mathbf{M}^{-1}, \mathbf{B}] \neq 0$, which implies in general that Λ is a tridiagonal matrix with random entries and that Λ is neither symmetric nor anti-symmetric.

2.1.2 "Weakly nonlinear" regime ($\Delta_n > |u_{n-1} - u_n|$)

In this case, nonlinearity starts getting a role in the dynamics of Eq. (2.1), and Eq. (2.8) no longer describe accurately the temporal evolution of the chain. A better description comes from considering the next terms in the Taylor expansion of the force, this yields

$$m_n \ddot{u}_n = \sum_{i=1}^{3} \left[B_n^{(i)} (u_{n-1} - u_n)^i - B_{n+1}^{(i)} (u_n - u_{n+1})^i \right]\,, \tag{2.13}$$

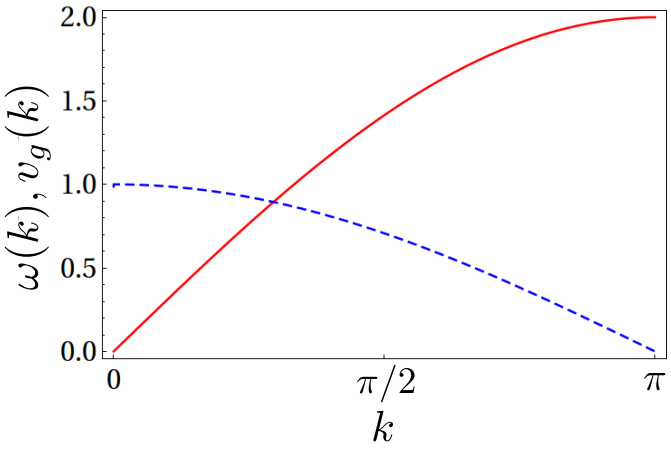


Figure 2.1: Dispersion relation (solid red curve) and group velocity (dashed blue curve) as a function of k for a homogeneous chain. We measure both quantities in units of $\sqrt{B/m}$.

where

$$B_n^{(1)} = B_n \propto R^{1/3}\,, \tag{2.14}$$

$$B_n^{(2)} = \frac{3}{8} A_n^{4/3} F_0^{-1/3} \propto R^{2/3}\,, \tag{2.15}$$

$$B_n^{(3)} = -\frac{3}{48} A_n^2 F_0^{-1} \propto R\,. \tag{2.16}$$

This amounts to a particular case of the Fermi–Pasta–Ulam (FPU) model [36]. One interesting feature of this regime is that — in absence of disorder and due to the specific relation between the parameters $B_n^{(1)}$, $B_n^{(2)}$, and $B_n^{(3)}$ in Eq. (2.14) — localized solutions [14] do not exist. This phenomenon was discussed in reference [150] based on consideration of modulational instabilities (MI). In essence, a MI is one of the generic mechanisms of spontaneous localization due to nonlinearity. However, to have a MI one needs $3B^{(1)}B^{(3)} - 4B^{(2)} > 0$, which is not satisfied in the present case. Nevertheless, introducing defects in the system leads to the emergence of localization in both the linear and weakly nonlinear regime. [150]

2.1.3 "Strongly nonlinear" regime ($\Delta_n \lessapprox |u_{n-1} - u_n|$)

When the precompression is sufficiently weak, one can no longer approximate Eq. (2.1) by truncating a Taylor expansion. In general, for materials in which the

sound speed goes to 0 or remains very low, it is not reasonable to use a standard linear approximation as a starting point for a perturbative analysis [121]. This is particularly interesting from the point of view of transport and localization theory in nonlinear disordered systems, because most of the research in the field has focused on the influence of nonlinearity of disordered systems in which the linear spectrum is initially either full or partially full of localized modes, such as Anderson modes [38, 88]. Consequently, understanding the interplay between disorder and nonlinearity in the sonic-vacuum limit, where the equations of motion are

$$m_n\ddot{u}_n = A_n[u_{n-1} - u_n]_+^{3/2} - A_{n+1}[u_n - u_{n+1}]_+^{3/2}, \tag{2.17}$$

brings interesting theoretical challenges. As a starting point to developing a theory for transport and localization in granular crystals, we will nevertheless start by focusing our efforts in a traditional way — by extending the linear theory to the nonlinear regime.

2.2 Solitary waves

It is well-known that Eq. (2.1) supports a particular type of localized solution, called solitary waves. This waves corresponds to pulses of energy that travel across the chain such that $u_n(t) = W(n - ct)$ for certain function W that defines the shape of the wave and c is the speed. Existence of this type of solution was proved by R.S. MacKay [105] in 1999, after experimental observations by Coste, Falco, and Fauve [22] in 1997 suggested it. The proof is based on the existence theorem for solitary waves on lattices, developed originally by Friesecke and Wattis [151], and it consists in minimizing the kinetic energy subject to given potential energy.

A first approximation of this solitary wave was made in 1986 by Lazaradi and Nesterenko [92]. Even though this is not necessarily the ultimate theory about solitary waves in granular crystals, it helps to generate intuition. This follows a standard procedure in discrete models and it uses a long-wavelength

approximation. By introducing a small parameter ϵ and defining a new variable $U(X,T) \approx u_n(t)$ that approximates the solution of Eq. (2.1). New coordinates are defined as $X = \epsilon n$ and $T = \epsilon t$, thus differences can be converted into partial derivatives through a Taylor expansion of U:

$$\begin{aligned} U(\epsilon(n \pm 1), T) &= U(X,T) \pm \epsilon \frac{\partial}{\partial X} U(X,T) + \frac{\epsilon^2}{2} \frac{\partial^2}{\partial X^2} U(X,T) \\ &\pm \frac{\epsilon^3}{3!} \frac{\partial^3}{\partial X^3} U(X,T) + \frac{\epsilon^4}{4!} \frac{\partial^4}{\partial X^4} U(X,T) + \cdots . \end{aligned} \tag{2.18}$$

Because ϵ is small, the wavelength of $U(X,T)$ is large in comparison with the underlying lattice. By plugging (2.18) into (2.1), one can derives a PDE that describes the dynamics of $U(X,T)$. This yields

$$\frac{\partial^2 U}{\partial T^2} = -\frac{\partial}{\partial X} \left\{ \left[-\frac{\partial U}{\partial X} \right]^{3/2} + \frac{\epsilon^2}{12} \left[\frac{\partial^2}{\partial X^2} \left(-\frac{\partial U}{\partial X} \right)^{3/2} - \frac{3}{8} \left(-\frac{\partial U}{\partial X} \right)^{-1/2} \frac{\partial^2 U^2}{\partial X^2} \right] \right\} , \tag{2.19}$$

where we have assume a homogeneous chain with normalized parameters (i.e., $A = m = 1$). This equation admits a solution in the form of a solitary wave. Before writing it down, it is convenient to define the coordinate $\bar{\xi} = X - cT$ and $r(\bar{\xi}) = \frac{\partial U(\bar{\xi},T)}{\partial \bar{\xi}}\Big|_{T=\bar{\xi}}$. In this way, Nesterenko solitary wave takes the form [92]

$$r(\xi) = \begin{cases} \frac{25}{16} \cos^4 \left(\frac{2\bar{\xi}}{\sqrt{10}} \right) & \text{if } |\bar{\xi}| < \sqrt{10}\pi/4 \,, \\ 0 & \text{otherwise} \,, \end{cases} \tag{2.20}$$

which constitutes a compact pulse traveling at speed c across the chain. This type of solutions are commonly excited in granular crystals and it is the main mechanism of transport of energy in uncompressed granular chains.

Chapter 3

IMPURITIES IN GRANULAR CRYSTALS

3.1 Introduction

In Chapter 2, we discussed different dynamical regimes that can be studied using granular crystals by modifying the static load F_0 (precompression). Moreover, we discuss different fundamental solutions, such as solitary waves, that are supported by granular crystals. However, more rich and complex phenomena can also be supported by granular crystals. For instance, granular crystals have been used for the investigation of numerous structural and material heterogeneities on nonlinear wave dynamics. This includes, as mentioned in Chapter 1, the role of defects [50, 56, 68, 106, 138, 143, 150], the scattering from interfaces between two different types of particles [24, 57, 122], chains of diatomic and triatomic units [11, 52, 65, 66, 67, 115, 130, 131], and much more.

When studying wave propagation in complex media, scattering due to inhomogenities results a fundamental topic [112, 123]. This is important when the scales of the waves and those of the inhomogeneities (i.e., impurities or defects)

This chapter is based on a paper published in *Physical Review E* [109]. Experiments in this paper were conducted at the Laboratory for Engineered Materials and Structures, University of Washington, US, by Prof. JK Yang's group.

are comparable, as interactions in such situations can lead to very rich dynamics. Pertinent phenomena include the formation of localized modes [39, 93], Fano resonances [104, 113], cloaking [13, 18], and many other examples of broad interest across numerous branches of physics.

In this chapter, we analyze a simpler setting in which one or a few defects occur within an otherwise homogeneous lattice, called a *host* lattice [150], under strong precompression (i.e., in the context of Eq. (2.8)). To understand how the impurities affect the dynamics of linear waves, we compute analytical expressions for the transmission coefficient and the reflection coefficient associated with the scattering of linear waves. Additionally, we briefly discuss the application of this theory to systems with multiple impurities and illustrate the impact with a specific example.

3.2 Scattering between linear waves and impurities

We start by studying the case of a strong precompression being applied to the system (i.e., $\Delta_n \gg |u_{n-1} - u_n|$). Thus, the nonlinearity is very weak and it can even be neglected. Note that this is equivalent to consider sufficiently small-amplitude vibrations in a granular crystal, but most of our discussions will be based on manipulating F_0[1] because this facilitates quantitative connections with experiments [109], which is discussed in Appendix B.

If one ignores the nonlinearity entirely, we have a harmonic interaction between the particles, so the dynamics can be described by Eq. (2.8). When impurities are introduced into a host chain, localized or resonant linear modes can arise (depending on the characteristics of the impurities [150]). For light impurities (i.e., $\alpha < 1$), one expects localized modes whose frequencies are larger than the upper bound Ω of the linear spectrum. For heavy impurities (i.e., $\alpha > 1$), by

[1]Note that, from Eq. (2.2), we have that $\Delta_n \propto F_0^{2/3}$.

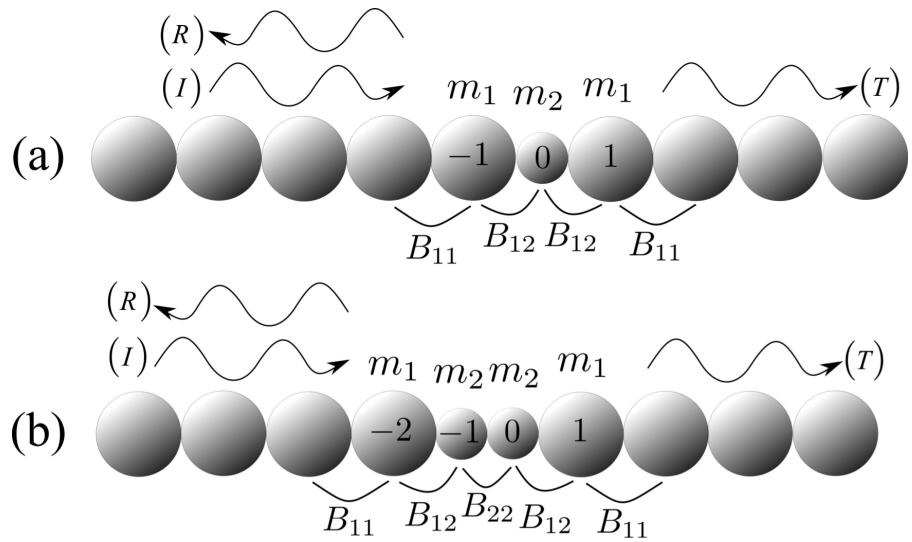


Figure 3.1: Schematic of a homogeneous granular chain with (a) one impurity and (b) two contiguous impurities (i.e., a double impurity). The incident wave is characterized by I, the reflected wave is characterized by R, and the transmitted wave is characterized by T. We label the identities of the particles with integers. We calculate the parameters $B_{ij} = \frac{3}{2}A_{ij}^{2/3}F_0^{1/3}$ from the static precompression and the interactions between adjacent particles.

contrast, one expects impurity modes with frequencies in the linear spectrum, and one thus expects resonant modes with extended linear eigenmodes.

We are interested in studying scattering processes between a plane wave $e^{\mathrm{i}(kn-\omega t)}$ and both single impurities and double impurities in the linear regime. Note that, because of the linearity of the Eq. (2.8), we can examine the displacements by writing them as complex quantities for notational convenience. In Fig. 3.1, we show schematics for chains with single and double impurities. We treat an impurity particle as a perturbation of a host particle: an impurity particle has radius $r_2 = \alpha r_1$, where r_1 is the radius of a host particle in the chain. We focus on $\alpha \in (0, 2]$. The value of the parameter α determines the mass of an impurity and the values of the interaction coefficients A_n between neighboring particles. For double impurities, we consider only the "symmetric" case in which both impurities are the same type of particle (and hence have the same radius).

To solve the scattering problem in the linear regime, we write [112]

$$u_n = \begin{cases} e^{\mathrm{i}(kn-\omega t)} + Re^{-\mathrm{i}(kn+\omega t)}, & \text{if} \quad n \leq 0 \\ Te^{\mathrm{i}(kn-\omega t)}, & \text{if} \quad n > 0 \end{cases}, \tag{3.1}$$

which represents an incident plane wave producing reflected and transmitted waves due to the interaction with the impurity. We thereby define a transmission coefficient $|T|^2$ and a reflection coefficient $|R|^2$. Note that $|R|^2 + |T|^2$ does not require to be equal 1 because both $|T|^2$ and $|R|^2$ are based on the norm of the displacement, which is not a conserved quantity of either Eq. (2.1) or Eq. (2.8). Intuitively, $|T|^2$ and $|R|^2$ are still "complementary" quantities, as a decrease in one is accompanied by an increase in the other (and vice versa). To have $|R|^2 + |T|^2 = 1$ for all parameter values, one would need to instead define $|R|^2$ and $|T|^2$ in terms of the energy density. The total energy is conserved by the dynamics, though it is much harder to measure than other quantities (e.g., velocity [109]). Given Eq. (3.1), the velocity is $\dot{u}_n = -\omega u_n$. Therefore, if we defined $|T|^2$ and $|R|^2$ in terms of $\dot{u}_n$ rather than u_n, we would obtain the same results, because $\dot{u}_n$ and u_n differ only by the constant factor $-\omega$. We therefore define reflection and transmission coefficients in terms of displacement, which allows us to compare analytical results directly not only with computations but also laboratory experiments (see Appendix B).

We substitute the ansatz (3.1) into Eq. (2.8) near the impurities and do a straightforward calculation to obtain the following linear system of equations for T and R:

$$\begin{pmatrix} \beta_{(i),(ii)} & \delta_{(i),(ii)} \\ \eta_{(i),(ii)} & \gamma_{(i),(ii)} \end{pmatrix} \begin{pmatrix} T_{(i),(ii)} \\ R_{(i),(ii)} \end{pmatrix} = \begin{pmatrix} \epsilon_{(i),(ii)} \\ \zeta_{(i),(ii)} \end{pmatrix}, \tag{3.2}$$

where the subscripts (i) and (ii), respectively, indicate chains with single and double impurities.

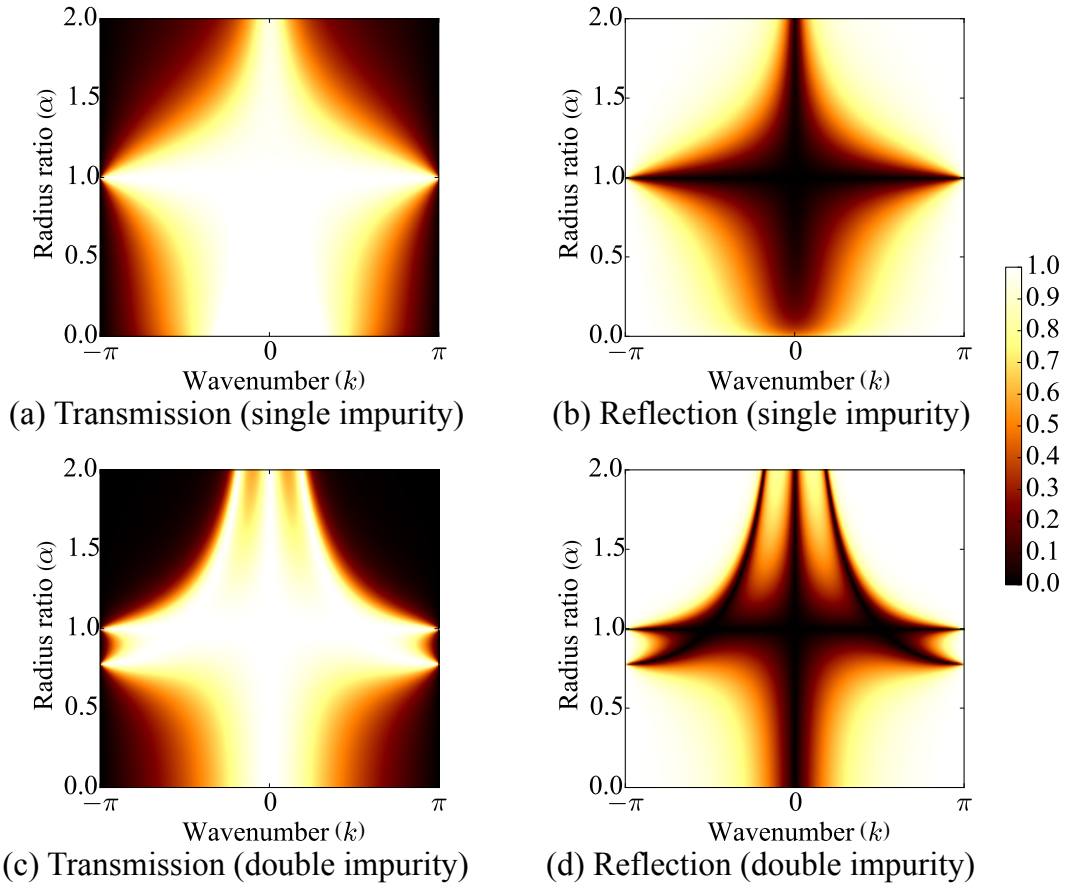


Figure 3.2: (a,c) Transmission and (b,d) reflection coefficients for the scattering of a plane wave in a chain with impurities as a function of the wavenumber k and the radius ratio α. We show examples for (a,b) a single impurity and (c,d) a double impurity. We describe the physical parameters of the particles in the chain in Table B.1.

For a single-impurity chain, the parameters in Eq. (3.2) are

$$\begin{aligned}
\beta_{(i)} &= \bar{\Omega} + B_{12}(2 - e^{\mathrm{i}k})\,, \\
\gamma_{(i)} &= -B_{12}e^{\mathrm{i}k}\,, \\
\delta_{(i)} &= B_{12}e^{-\mathrm{i}k}\,, \\
\eta_{(i)} &= B_{12}\,, \\
\epsilon_{(i)} &= B_{11}e^{2\mathrm{i}k} - (B_{11} + B_{12} + \bar{\Omega})e^{\mathrm{i}k}\,, \\
\zeta_{(i)} &= -B_{11}e^{-2\mathrm{i}k} + (B_{11} + B_{12} + \bar{\Omega})e^{-\mathrm{i}k}\,,
\end{aligned}$$

where $\bar{\Omega} = -\frac{2B_{11}m_2}{m_1}[1-\cos(k)]$. Solving Eq. (3.2) yields the reflection and transmission coefficients:

$$|R_{(i)}|^2 = \left| \frac{B_{11}(B_{11}-B_{12})m_2 - (2B_{11}-B_{12})(B_{11}m_2 - B_{12}m_1)e^{\mathrm{i}k} + B_{11}(B_{11}m_2 - B_{12}m_1)e^{2\mathrm{i}k}}{B_{11}^2 m_2 e^{\mathrm{i}k} + (B_{11}-B_{12})(B_{11}m_2 - B_{12}m_1)e^{3\mathrm{i}k} - B_{11}(2B_{11}m_2 - 2B_{12}m_1 - B_{12}m_2)e^{2\mathrm{i}k}} \right|^2 ,$$
$$|T_{(i)}|^2 = \left| \frac{B_{11}B_{12}m_1(1+e^{\mathrm{i}k})}{B_{11}^2 m_2 + (B_{11}-B_{12})(B_{11}m_2 - B_{12}m_1)e^{2\mathrm{i}k} - B_{11}(2B_{11}m_2 - 2B_{12}m_1 - B_{12}m_2)e^{\mathrm{i}k}} \right|^2 . \tag{3.3}$$

For a double-impurity chain, we follow the same procedure and use the parameters

$$\begin{aligned}
\beta_{(ii)} &= \bar{\Omega} + B_{12}(1-e^{\mathrm{i}k}) + B_{22} \,, \\
\gamma_{(ii)} &= -B_{22}e^{\mathrm{i}k} \,, \\
\delta_{(ii)} &= B_{22}e^{-\mathrm{i}k} \,, \\
\eta_{(ii)} &= B_{22} \,, \\
\epsilon_{(ii)} &= B_{12}e^{2ik} - (B_{12}+B_{22}+\bar{\Omega})e^{\mathrm{i}k} \,, \\
\zeta_{(ii)} &= -B_{12}e^{-2ik} + (B_{12}+B_{22}+\bar{\Omega})e^{-\mathrm{i}k}
\end{aligned}$$

in Eq. (3.2). Note that $\bar{\Omega}$ has exactly the same expression as before. We obtain

$$|R_{(ii)}|^2 = \left| \frac{4\left(B_{12}(B_{12}+B_{22})m_1^2 - 2B_{11}(B_{12}+B_{22})m_1m_2 + 2B_{11}^2m_2^2 + 2B_{11}m_2(B_{12}m_1 - B_{11}m_2)\cos(k)\right)\sin^2(k/2)e^{-2ik}}{\left(B_{12}m_1(e^{\mathrm{i}k}-1) + 2B_{11}m_2 - 2B_{11}m_2\cos(k)\right)\left(B_{12}m_1(e^{\mathrm{i}k}-1) - 2B_{22}m_1 + 2B_{11}m_2 - 2B_{11}m_2\cos(k)\right)} \right|^2 ,$$
$$|T_{(ii)}|^2 = \left| \frac{B_{12}B_{22}m_1^2(1-e^{-2ik})}{\left(B_{12}m_1(e^{\mathrm{i}k}-1) + 2B_{11}m_2 - 2B_{11}m_2\cos(k)\right)\left(B_{12}m_1(e^{\mathrm{i}k}-1) - 2B_{22}m_1 + 2B_{11}m_2 - 2B_{11}m_2\cos(k)\right)} \right|^2 . \tag{3.4}$$

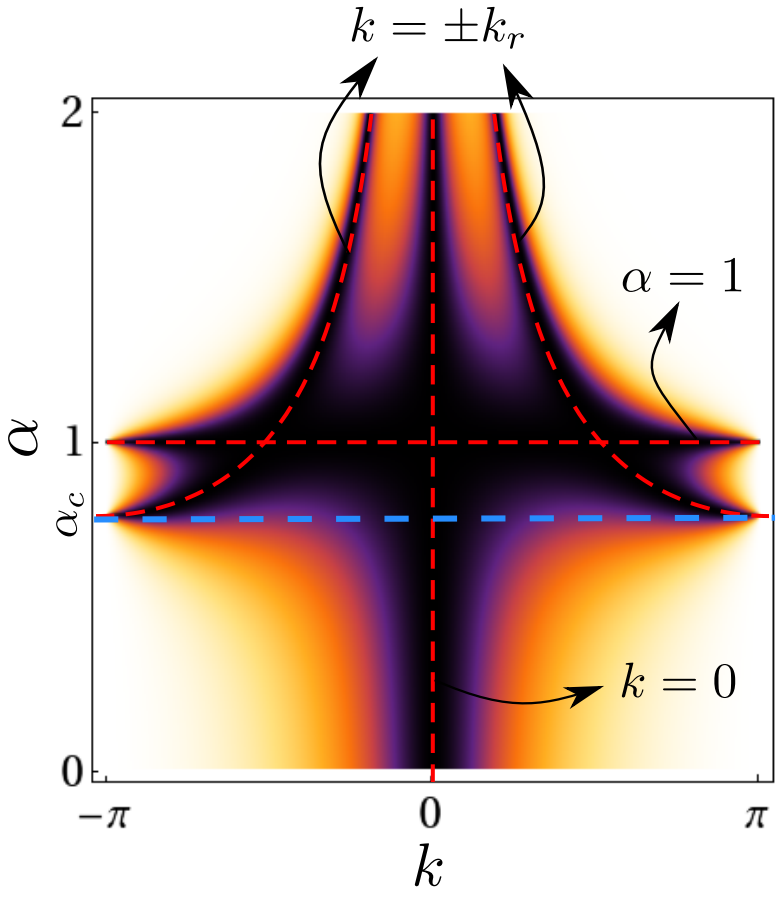


Figure 3.3: Reflection coefficient $|R_{(ii)}|^2$ for a double impurity. The red dashed curves indicate the points at which the reflection coefficient is exactly 0. The resonant wavenumber k_r is given by Eq. (3.5). The blue dashed line highlights the critical value α_c. The system has a Ramsauer–Townsend (RT) resonance at wavenumber $k = \pm k_r$ for $\alpha > \alpha_c$.

In Fig. 3.2, we show the reflection and transmission coefficients as functions of k and α. Observe in panels (b) and (d) that there is a black region of *reflectionless* modes that can traverse either a single impurity or a double impurity almost without modification. For single impurities, the reflection coefficient $|R|^2$ vanishes only when either $\alpha = 1$ or $k = 0$. Similar results were obtained in the context of phonon scattering by a localized equilibrium [138], where *perfect* transmission of phonons across impurities was possible only at $k = 0$. By contrast, for a double impurity, $|R|^2$ vanishes not only when $\alpha = 1$ and $k = 0$ but

also when $k = \pm k_r \neq 0$ when α is larger than some critical value α_c. At these resonant values, a wave can be transmitted completely through the impurities (i.e., there is no scattering), and it experiences only a phase shift. Granular crystals thereby yield an analog of the well-known Ramsauer–Townsend (RT) effect[2]. Hereafter, we use the term "RT resonance" to describe the resonance at $k = \pm k_r$. In our case, one can explicitly write k_r in terms of the physical parameters of the system as

$$k_r = \arccos(\phi) \ , \tag{3.5}$$

where

$$\phi = \frac{B_{12}B_{22}m_1^2 - 2B_{11}B_{22}m_1m_2}{2B_{11}m_2\left[B_{11}m_2 - B_{12}m_1\right]} + \frac{B_{11}\left[m_1^2 - 2m_1m_2 + 2m_2^2\right]}{2m_2\left[B_{11}m_2 - B_{12}m_1\right]} \, .$$

In Fig. 3.3, we show k_r and the other relevant values of the reflection coefficient for a double impurity in terms of the parameter α. To ensure that $k_r \in \mathbb{R}$, we need $\phi \in [-1, 1]$. In terms of α, this implies that the resonant wavenumber k_r exists when $\alpha_c \leq \alpha < \infty$. An interesting feature of k_r is that it can be tuned as a function of α to any value in the interval $[0, \pi]$. In particular, we find that $k_r = \pi$ at $\alpha = \alpha_c$ and $k_r \to 0$ as $\alpha \to \infty$. Consequently, one can tune the frequency of the RT resonance to any value in the transmission band $(0, \Omega]$ of the host granular chain.

3.3 Multiple impurities

An interesting application of the RT resonance, which we discussed in Sec 3.2 for scattering with a double impurity, is its extension to systems with multiple double impurities. In particular, it is interesting to examine systems in which

[2]An RT resonance is a prototypical mechanism that enables scattering transparency in quantum mechanics [139]. In its most recognizable form, it consists of the presence of a sharp minimum in the electron scattering cross-section at low energies for scattering with rare gases (such as Xe, Kr, and Ar). The RT effect has been observed experimentally in many scenarios involving quantum tunneling, including e^-–Ar scattering [44], positron–Ar scattering [71], e^-–methane scattering [43], and others.

multiple impurities are either periodically or randomly distributed within a host homogeneous chain.

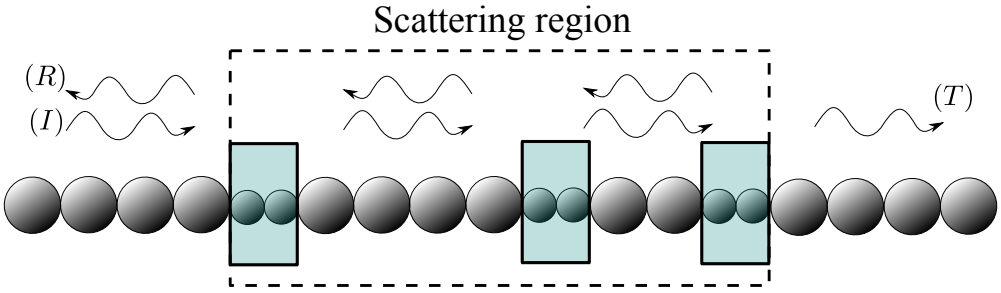


Figure 3.4: Schematic of a host homogeneous granular chain with multiple double impurities. The incident wave is (I), the reflected wave is (R), and the transmitted wave is (T). We highlight impurities in turquoise boxes, and we indicate the scattering region with the dashed box.

To examine if reflectionless modes still occur when considering multiple impurities in a host granular chain, we use the formalism of transfer matrices. This provides a useful framework to study transmission of waves through the entire system [23]. Following recent work by Zakeri et al. [158], we assume stationary plane waves $u_n(t) = w_n e^{\mathrm{i}\omega t}$ as in Sec. 3.2. Equation (2.8) then leads to

$$w_{n+1} = \frac{[(B_n + B_{n+1}) - m_n\omega^2]}{B_{n+1}} w_n - \frac{B_n}{B_{n+1}} w_{n-1}\,, \tag{3.6}$$

which generates the modes given a seed $\{w_0, w_1\}$. For $\omega = 0$, Eq. (3.6) reduces to

$$w_{n+1} = \frac{B_n}{B_{n+1}}\,(w_n - w_{n-1}) + w_n\,. \tag{3.7}$$

Thus, for any distribution of particles in the chain, the seed $w_0 = w_1$ implies that $w_n = w_0$ for all n. This explains why the reflection coefficients are exactly 0 at $\omega = k = 0$ for both single and double impurities (see Fig. 3.2).

In the absence of impurities, Eq. (3.6) generates propagating waves for any $\omega \in [0, \Omega]$. This is true in an infinite domain, while for a finite domain only the wavenumbers that conform to specified boundary conditions and the associated frequencies get selected. Once we have impurities, propagating waves can still

be generated through iterating Eq. (3.6) until we reach what we call a "scattering region" (see Fig. 3.4). In this region, multiple scatterings occur because the presence of impurities has broken discrete translation symmetry, and successive interferences can then lead to complicated dynamics that depend on the distribution of impurities.[3] When the distribution of impurities is such that impurities are well-separated from each other, one can reformulate the transmission problem [given by Eq. (3.6)] through the entire scattering region as a sequence of transfer problems from each segment of a granular chain through an impurity to the next segment. Thus, an incident plane wave $w_n = Ie^{\mathrm{i}k_r n}$ with wavenumber $k = k_r$ and amplitude I transforms into $T^{(1)}e^{\mathrm{i}k_r n}$ after a scattering event, because no reflected waves are generated during the scattering at $k = k_r$. By considering each impurity, we obtain the sequence $Ie^{\mathrm{i}k_r n} \to T^{(1)}e^{\mathrm{i}k_r n} \to T^{(2)}e^{\mathrm{i}k_r n} \to \cdots \to T^{(L)}e^{\mathrm{i}k_r n}$, where arrows denote the transmission of the wave through the impurities and $T^{(j)}$, with $j \in \{1, 2, \ldots, L\}$, denotes the transmitted-wave amplitudes, which (with rescaling such that $I = 1$) are are given by Eq. (3.4). Consequently, reflectionless modes can be supported by the chain in the form

$$w_n = \begin{cases} Ie^{\mathrm{i}k_r n}, & \text{if} \quad n \leq n_1 \\ T^{(1)}e^{\mathrm{i}k_r n}, & \text{if} \quad n_1 < n \leq n_2 \\ \vdots & \\ T^{(L)}e^{\mathrm{i}k_r n}, & \text{if} \quad n_L < n \end{cases}, \tag{3.8}$$

where n_j (with $j \in \{1, 2, \ldots, L\}$) represents the positions of the jth impurity in the host homogeneous chain. For other modes, transmission through the scattering region depends on the frequency ω. Based on our analysis in Sec. 3.2, we expect that transmission decays rapidly as one approaches the upper band edge Ω. By contrast, plane waves slowly attenuate for frequencies near 0.

To illustrate how this effect arises in strongly precompressed granular crystals, we numerically integrate Eq. (2.1) using the parameters described in Appendix B.1, but this time we randomly place double impurities in a scattering region around the middle of a chain. To implement this, we set the radii of each

[3]This phenomenon is discussed in detail in Chapter 4.

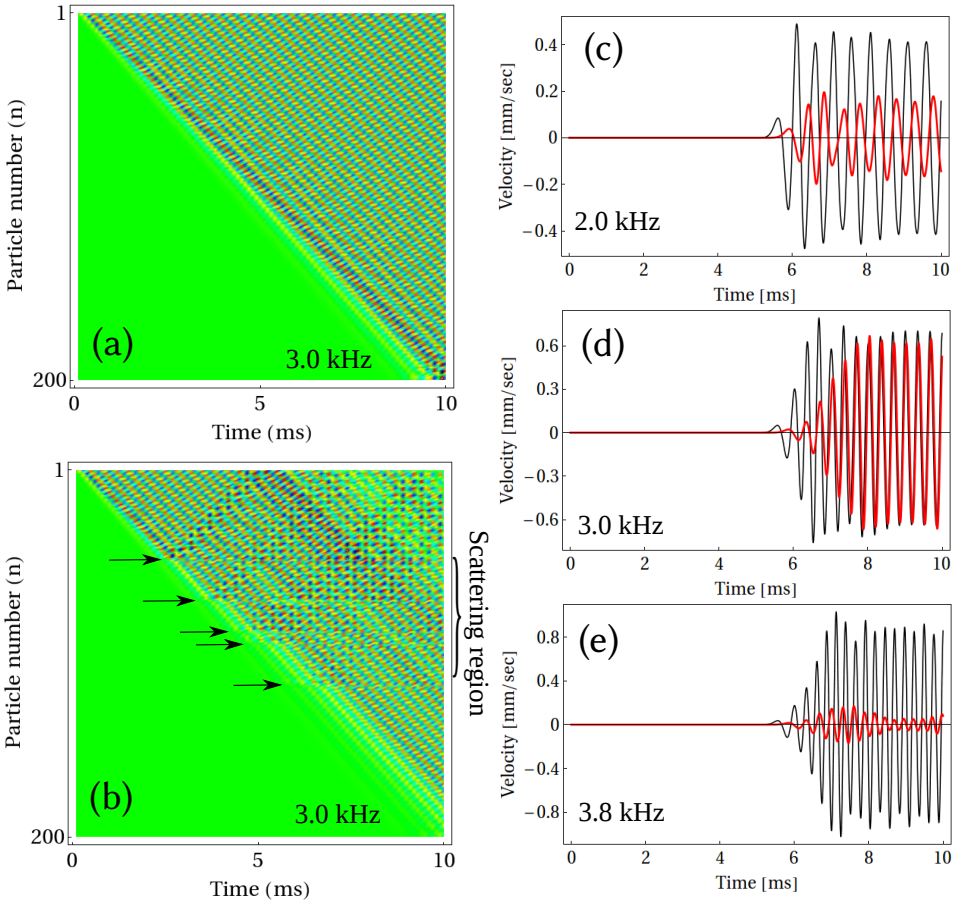


Figure 3.5: (a) Space-time contour plot of the normalized velocity for a homogeneous chain with $N = 200$ particles and an excitation frequency of 3.0 kHz. (b) The same as panel (a), but with five double impurities located at positions $n = 50$, $n = 72$, $n = 90$, $n = 96$, and $n = 118$. The radius ratio is $\alpha = 1.5$, and arrows indicate the position of the impurities. Panels (c)–(e) show the velocity at particle $n = 130$ for excitation frequencies of (c) 2.0 kHz, (d) 3.0 kHz, and (e) 3.8 kHz. The black curves are associated with the homogeneous chain [panel (a)], and the red curves are associated with the chain with the impurities [panel (b)].

pair of consecutive particles in the scattering region as r_1 with probability 1/2 and as r_2 with probability 1/2. We consider a chain with $N = 200$ particles, and we define the scattering region to be between particles $n = 50$ and $n = 120$, with radius ratio $\alpha = 1.5$. One can calculate the frequency of the RT resonance using Eq. (3.5), which in this case gives $f_r \approx 3.0$ kHz. As we predicted, when

the system is driven at this frequency, waves experience a phase shift due to the scattering, but the amplitude is consistently transmitted almost without modification through the scattering region of the random chains. However, when we move away from the frequency of the RT resonance, the transmission decays. We observe this directly by measuring the velocity of a particle right after the scattering region (see Fig. 3.5). We compare the temporal evolution of the velocities of the particles for a homogeneous chain and a chain with five double impurities. In panels (c) and (e), we observe attenuation in the magnitude of the velocity due to the presence of impurities in the chain. In panel (d), when the system is driven at 3.0 kHz, the wave is clearly delayed in the perturbed chain compared with the homogeneous one, although the magnitude of the velocity is about the same for both chains.

3.4 Conclusions

In the present chapter, we examined the scattering of waves by single impurities and double impurities in granular chains. We started by exploring the linear scattering problem, motivated by the context of strongly precompressed granular chains with either a single impurity or a double impurity. We derived analytical formulas to show that the scattering is different for the different impurity configurations. For single-impurity chains, we showed that the transmission coefficient $|T|^2$ decays monotonically with k (and hence with the frequency ω). We also found that $|T|^2 \to 0$ as one approaches the band-edge frequency of the host homogeneous chain. By contrast, for a double-impurity chain, we showed that an effect analogous to the Ramsauer–Townsend resonance takes place at $k = k_r \in [0, \pi]$ and for a specific region of parameter space. We demonstrated that one can tune the frequency of this RT resonance to any value within the transmission band of the host homogeneous chain.

We also demonstrate what happens when there are multiple double impurities distributed in a chain. We observed that the system still transmits most of the energy at the frequency of the RT resonance. This is relevant for Chapter 4,

where we will focus on chains with disorder throughout, instead of merely placing a disordered segment.

Chapter 4

DISORDERED GRANULAR CRYSTALS

In Chapter 3, we studied the scattering of linear waves with single and double impurities. We showed, in both cases, that transmission across the impurities is always possible around specific frequencies depending on the parameters. We also discussed the case where multiple impurities were added to the chain in a "low density" fashion. In this Chapter we systematically study granular chains that are completely random and in different dynamical regimes, from strongly nonlinear to linear.

We use a conservative approach, in the sense of energy conservation, as it has demonstrated its usefulness repeatedly when comparing theoretical and computational results to laboratory experiments [121, 142], including in the presence of disorder [41, 128]. Note that the proper physical form of dissipation is not known; see Refs. [15, 142] for a discussion of dissipative forces in granular crystals.

The boundary conditions of Eq. (2.1) are given by considering $u_0 = u_{N+1} = 0$ and the limits $R_0, R_{N+1} \to \infty$. It is worth noting that if one of the radii in Eq. (2.3) goes to infinity, then one recovers the interaction between an elastic plate and an elastic sphere given by Eq. (1.8). Thus, the equations of motion for

This chapter is based on two papers, one published in Physical Review E [107] and the other published in Nature Communications [78].

spheres 1 and N can be written as

$$m_1\ddot{u}_1 = A_1[\Delta_1 - u_1]_+^{3/2} - A_2[\Delta_2 + u_1 - u_2]_+^{3/2}, \quad (4.1)$$

$$m_N\ddot{u}_N = A_N[\Delta_N + u_{N-1} - u_N]_+^{3/2} - A_{N+1}[\Delta_{N+1} + u_N]_+^{3/2}. \quad (4.2)$$

Figure 4.1 shows an example of the physical set-up; it consists of a randomly distributed sequence of spheres being precompressed by an external force.

The remainder of the Chapter is organized as follows. In Sec. 4.1, we describe the three types of disorder that we consider and in Sec. 4.2 their correlation properties. The physical parameters used in the simulations are described in Sec. 4.3. Sec. 4.4 is the most extensive one as it describes all the numerical results, from localization to transport in all the different configurations and for different initial conditions.

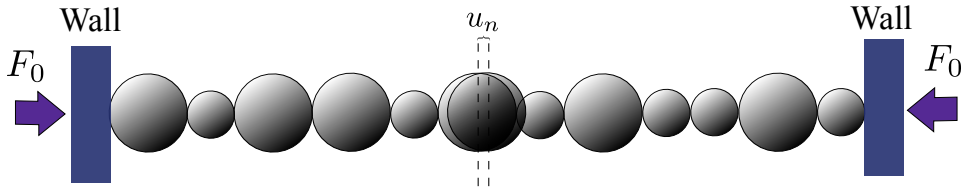


Figure 4.1: Physical set-up related to Eq. (2.1) with boundary conditions given by Eqs. (4.1) and (4.2).

4.1 Types of disorder

We now describe the three types of disordered granular chains that we study in this dissertation. First, suppose that we have two types of spheres: type 1 has radius R_1, and type 2 has radius $R_2 = \alpha R_1$, where $\alpha \in (0, 1]$. Additionally, we suppose that all of the spheres are made from the same material, so their mechanical properties are the same; that is, $E_1 = E_2 = E$, $\nu_1 = \nu_2 = \nu$, and the densities are the same. However, the masses m_1 and m_2 are different. Note that $\alpha = 1$ reduces the system to the case of a homogeneous chain. We consider three different ways of distributing the particles to produce disorder: (1) an Anderson-like distribution, (2) a random dimer distribution that follows

the choice in Ref. [30] (RDM1), and a random dimer distribution that follows the choice in Ref. [128] (RDM2).

Specifically, we construct disordered chains as follows:

1. Anderson-like (A): For each of the N particles in a chain, choose radius R_1 with probability $q \in [0, 1]$ and radius R_2 with probability $1 - q$.

2. Random dimer 1 (RDM1): For each of the $N/2$ dimers in a N-particle chain, we choose the configuration R_1R_1 (i.e., both particles have a radius of R_1) with probability $q \in [0, 1]$ and the configuration R_2R_2 with probability $1 - q$.

3. Random dimer 2 (RDM2): For each of the $N/2$ dimers in a N-particle chain, we choose the configuration R_1R_2 with probability $q \in [0, 1]$ and the configuration R_2R_1 with probability $1 - q$. (That is, we are choosing the orientation of dimer, which we imagine to be a spin with two possible states [128].)

In Figure 4.2, we show examples of configurations for each type of disordered chain.

Because these granular chains include two types of spheres (and are oriented horizontally, so we can ignore gravity) there are three types of sphere–sphere interactions:

- $A_{11} = \frac{E\sqrt{2R_1}}{3(1-\nu^2)}$ (between two spheres of radius R_1),
- $A_{22} = \frac{E\sqrt{2R_2}}{3(1-\nu^2)}$ (between two spheres of radius R_2),
- $A_{12} = \frac{2E}{3(1-\nu^2)} \left(\frac{R_1R_2}{R_1+R_2}\right)^{1/2}$ (between spheres of different radii).

As we can see, the disorder can be characterized by two parameters. The parameter q determines the amount of disorder. Thus, $q = 0$ and $q = 1$ for the ordered cases, and $q = 1/2$ is the most disordered case. The parameter α determines the strength of the disorder. The magnitude of the interactions

A_{12}, A_{22}, and the masses of the beads depend on α, which has an analogous effect in the system as the *width of the disorder* that is often used in disordered models. [38]

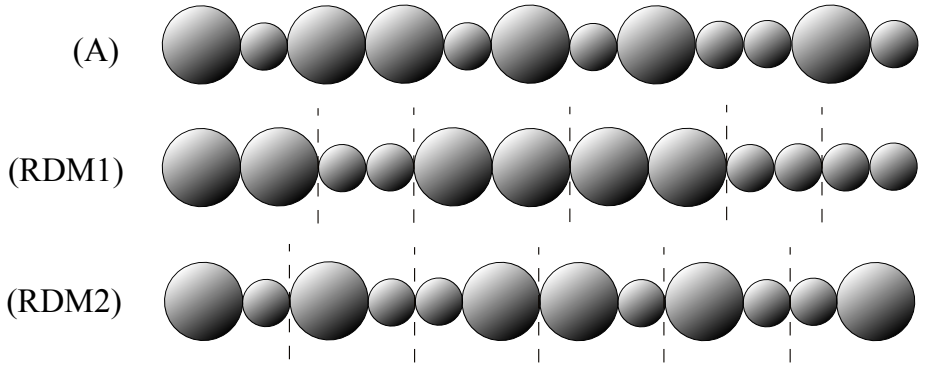


Figure 4.2: Examples of different types of disordered chains. (A) Anderson-like model, (RDM1) random dimer model 1, and (RDM2) random dimer model 2. The vertical dashed lines are for visual guidance to separate adjacent dimers from each other.

4.2 Correlations

In this section, we study the correlation properties for each type of disorder. Let $\mathbf{v_0}$ be a random vector generated by the rules that we described in Section 4.1. Without loss of generality, we label each entry $v_{0,i}$ of $\mathbf{v_0}$ as 0 or 1. Thus, for example, the Anderson-like chain has

$$v_{0,i} = \begin{cases} 0\,, & \text{with probability} \quad q\,, \\ 1\,, & \text{with probability} \quad (1-q)\,, \end{cases} \tag{4.3}$$

with $i = 1, 2, \ldots, N$. For the dimer models

$$v_{0,i} = \begin{cases} c_0\,, & \text{with probability} \quad q\,, \\ c_1\,, & \text{with probability} \quad (1-q)\,, \end{cases} \tag{4.4}$$

with $i = 1, 2, \ldots, N/2$, where $\{c_0, c_1\} = \{0\,0, 1\,1\}$ for RDM1, and $\{c_0, c_1\} = \{0\,1, 1\,0\}$ RDM2.

Let $\mathbf{v_n}$ be the n-cyclic permutation of $\mathbf{v_0}$ that satisfies

$$v_{n,i} = \begin{cases} v_{0,i-n}\,, & \text{if} \quad i > n\,, \\ v_{0,N-n+i}\,, & \text{if} \quad i \leq n\,. \end{cases} \tag{4.5}$$

To characterize the extent of correlation in each case, we use the Pearson correlation coefficient

$$\rho_{n,n'} = \frac{\mathrm{cov}\left(\mathbf{v_n}, \mathbf{v_{n'}}\right)}{\sigma_{\mathbf{v_n}}\sigma_{\mathbf{v_{n'}}}}\,, \tag{4.6}$$

where $\mathrm{cov}(\mathbf{v_n}, \mathbf{v_{v'}}) = \mathrm{E}\left[(\mathbf{v_n} - \bar{v}_n\mathbf{I})(\mathbf{v_{n'}}\mathbf{I} - \bar{v}_{n'})\right]$ is the covariance between $\mathbf{v_n}$ and $\mathbf{v_{n'}}$, the vector $\mathbf{I} = (1, 1, \ldots, 1)$ has all elements equal to 1, the standard deviation of $\mathbf{v}$ is $\sigma_\mathbf{v} = \sqrt{\mathrm{E}\left[(\mathbf{v} - \bar{v}\mathbf{I})^2\right]}$, and the mean of $\mathbf{v}$ is $\mathrm{E}\left[\mathbf{v}\right] = \bar{v}$. (Recall that E[$\mathbf{y}$] denotes the expectation of $\mathbf{y}$.) For our computations it is convenient to write the covariance as

$$\mathrm{cov}\left(\mathbf{v_n}, \mathbf{v_{n'}}\right) = \frac{1}{N}\sum_{i=1}^{N}\left[v_{n,i}v_{n',i} - \left(v_{n,i}\bar{v}_{n'} + v_{n',i}\bar{v}_n\right) + \bar{v}_n\bar{v}_{n'}\right]\,. \tag{4.7}$$

Note that some statistical properties, such as the mean and standard deviation, are independent of permutations, so we can write Eq. (4.7) as

$$\mathrm{cov}\left(\mathbf{v_n}, \mathbf{v_{n'}}\right) = \left(\frac{1}{N}\sum_{i=1}^{N} v_{n,i}v_{n',i}\right) - \bar{v}^2\,, \tag{4.8}$$

where one can calculate the term in parentheses as the sum of conditional probabilities that depend on the type of disorder. In the next three subsections, we calculate the correlation coefficients for each kind of disorder in the thermodynamic limit (i.e., $N \to \infty$ limit).

4.2.1 Anderson-like

In the granular chain with an Anderson-like disorder, the mean value of $\mathbf{v}$ is $\bar{\mathbf{v}} = (1 - q)$ and the standard deviation is $\sigma_\mathbf{v} = \sqrt{q(1-q)}$. Both quantities depend on the probability q. The correlation is

$$\rho^a_{n,n'} = \delta_{0,|n-n'|}\,, \tag{4.9}$$

and is independent of $q \in (0, 1)$. When $q = 0$ or $q = 1$, the correlation becomes $\rho_{n,n'} = 1$ because the granular chain is homogeneous. Equation (4.9) implies that the Anderson-like disorder is an uncorrelated type of disorder. This is true exactly in the thermodynamic limits (i.e. in $N \to \infty$). However, this is also

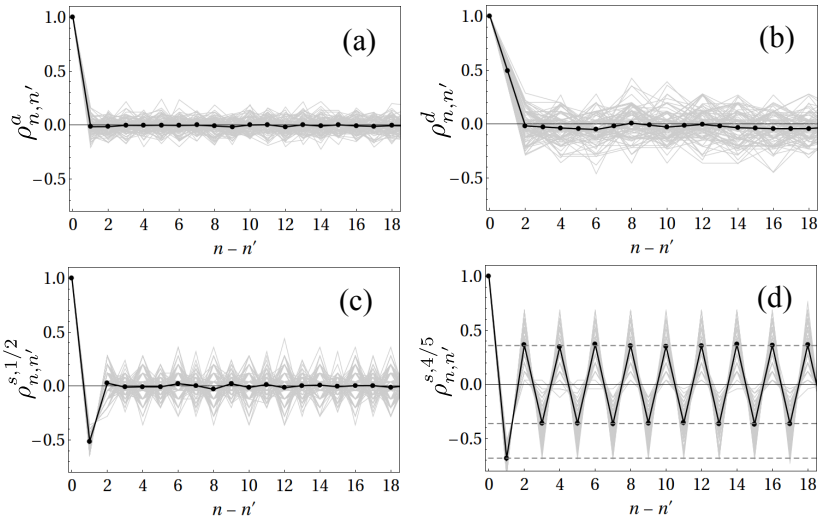


Figure 4.3: Correlation function $\rho_{n,n'}$ as a function of distance between particles for the three types of disordered granular chains: (a) Anderson-like model, (b) random dimer model 1, and (c,d) random dimer model 2. The gray curves show 100 realizations for $N = 100$ particles, and the black curves give the mean values. In panels (a)–(c), we use $q = 1/2$; in panel (d), we use $q = 4/5$. The horizontal dashed lines in panel (d) show the analytical value for the long-range correlation given by Eq. (4.11).

true in an average sense for finite systems; the mean of the correlations over the correlations of a large number $\bar{N}$ of finite systems goes to the value of the correlation for a single system in the thermodynamic limit as $\bar{N} \to \infty$. In Fig. 4.3(a), we show the Pearson correlation as function of the relative distance between spheres. The black curve shows the mean value, which tends to $\delta_{0,|n-n'|}$.

4.2.2 Random dimer model 1

As in the Anderson-like case, the mean value of $\mathbf{v}$ for the RDM1 granular chain is $\bar{\mathbf{v}} = (1-q)$ and the standard deviation is $\sigma_{\mathbf{v}} = \sqrt{q(1-q)}$. However, because an RDM1 granular chain consists of dimers, there is now a short-range correlation. We calculate the Pearson correlation

$$\rho^{d}_{n,n'} = \delta_{0,|n-n'|} + \frac{1}{2}\delta_{1,|n-n'|}\,, \tag{4.10}$$

which we note is again independent of $q \in (0,1)$. Consequently, the chain has a short-range correlation between second-nearest neighbors for any $q \in (0,1)$.

In Figure 4.3(b), we show the Pearson correlation as function of the relative distance between spheres.

4.2.3 Random dimer model 2

The RDM2 granular chain has rather different statistical properties from the other two types of disordered chains.

The mean value of $\mathbf{v}$ is $\bar{\mathbf{v}} = 1/2$, and the standard deviation is $\sigma_{\mathbf{v}} = 1/4$. Both the mean and the standard deviation are independent of the probability q, because q affects only the orientation of the dimer; the numbers of 0 values and 1 values are unchanged. This type of disorder includes a long-range correlation that one can tune with the parameter q. It is given by

$$\rho_{n,n'}^{s,q} = \delta_{0,|n-n'|} - \frac{1}{2}\left[(2q-1)^2+1\right]\delta_{1,|n-n'|} + \sum_{j=2}^{N}(-1)^j(2q-1)^2\delta_{j,|n-n'|}\,. \quad (4.11)$$

An interesting special case occurs when $q = 1/2$, as the correlation reduces to a short-range anti-correlation:

$$\rho_{n,n'}^{s,1/2} = \delta_{0,|n-n'|} - \frac{1}{2}\delta_{1,|n-n'|}\,. \quad (4.12)$$

Other interesting limits are the ordered diatomic chains that arise for $q = 0$ and $q = 1$. Because the orientation of all of the dimer units is constant in these limits, there is a perfect correlation between particles that are an even distance apart and a perfect anti-correlation between particles that are an odd distance apart:

$$\rho_{n,n'}^{s,0} = \rho_{n,n'}^{s,1} = \sum_{s=0}^{N}(-1)^s\delta_{s,|n-n'|}\,. \quad (4.13)$$

In Figures 4.3(c,d), we show the Pearson correlation as function of the relative distance between spheres.

4.3 Physical parameters

There have been numerous experimental investigations of granular crystals [142]. In this Chapter, we consider that all the spheres are made of steel, and we use the parameters given in [150] unless we specify otherwise. Additionally, we suppose that the elastic plates at the boundaries of the system have the same mechanical properties as the spheres. The elastic modulus is $E = 193$ GPa, the Poisson ratio is $\nu = 0.3$, the density is $\rho = 8027.17$ kg/m^3. To have two different types of spheres we use radii $R_1 = 4.76$ mm and $R_2 = \alpha R_1$, with $\alpha \in (0, 1]$. The static precompressive force F_0 necessary to have predominantly linear effects is on the order of 10 N [10], so we use $F_0 \in [0, 10]$ N.

4.4 Numerical results

In general, it is difficult to precisely determine localization properties in disordered systems — primarily because most tests are based on the asymptotic behavior of particular observables (e.g. energy). From a practical perspective one needs to consider long chains (and large volumes in larger dimensions) and very long integration times.[1] Such scenarios are difficult to achieve experimentally, and even numerical simulations pose considerable difficulties [144]. In particular, one is often interested in the asymptotic behavior of the energy distribution. Hence, to conduct long-time simulations without significant (and unphysical) variation in a system's total energy, it is necessary to employ carefully-chosen numerical-integration schemes. This is discussed with more detail in Appendix A. Additionally, because we are examining disordered systems and we thus need to average over a large number of realizations of a particular type of disorder to obtain appropriate statistical power, it is also necessary to employ sufficiently fast numerical-integration schemes that are also particularly accurate in their energy conservation. We thus use a symplectic integrator from Refs. [91, 144, 145].

[1] From a theoretical perspective one should let both time and system size go to infinity [80].

We also rely on indirect methods to develop intuition about the asymptotic behavior of disordered granular chains. One such method is to study the structure of the linear spectrum and the extent of localization of the linear modes. For instance, in the classical Anderson model in a 1D electronic system [3], all of the linear modes are localized exponentially for any amount of disorder. This leads to an absence of diffusion that manifests as a saturation of the second moment of the probability distribution as a function of time. In other words, excitations remain spatially localized. By contrast, the RDM1 [30] (built with double impurities) behaves differently from the Anderson model (built with single impurities) in this respect, as the former includes extended modes that transmit almost without losses of energy. This causes the second moment to grow as a function of time.

In our ensuing discussions, we investigate the influence of the three different types of disorder on the structure of the linear spectrum and the presence of localized states in both the bulk and the surface of a granular chain. We subsequently investigate transport and dynamical localization in the bulk for disordered Hertzian chains (2.1).

4.4.1 Diagonalization of Eq. (2.12)

There are various ways of measuring localization in linear modes. In finite systems, it is useful to calculate the inverse participation ratio (IPR) [80]

$$P^{-1} = \frac{\sum_{n=1}^{N} h(v_n, \dot{v}_n)^2}{\left(\sum_{n=1}^{N} h(v_n, \dot{v}_n)\right)^2}, \tag{4.14}$$

where $h(v_n, \dot{v}_n)$ in some distribution. For modal analysis, we use $h(v_n, \dot{v}_n) = v_n^2$, which allows one to measure the fraction of particles whose displacement of position from equilibrium differs markedly from 0. We can thereby measure the extent of localization. For instance, a plane wave with all sites equally excited satisfies $P^{-1} \to 0$ as the number of particles $N \to \infty$. By contrast, a strongly localized wave satisfies $P^{-1} \to 1$, and $P^{-1} = 1$ exactly when only one sphere is vibrating (i.e., when $v_n = 0$ for all $n \neq j$ and $v_j \neq 0$).

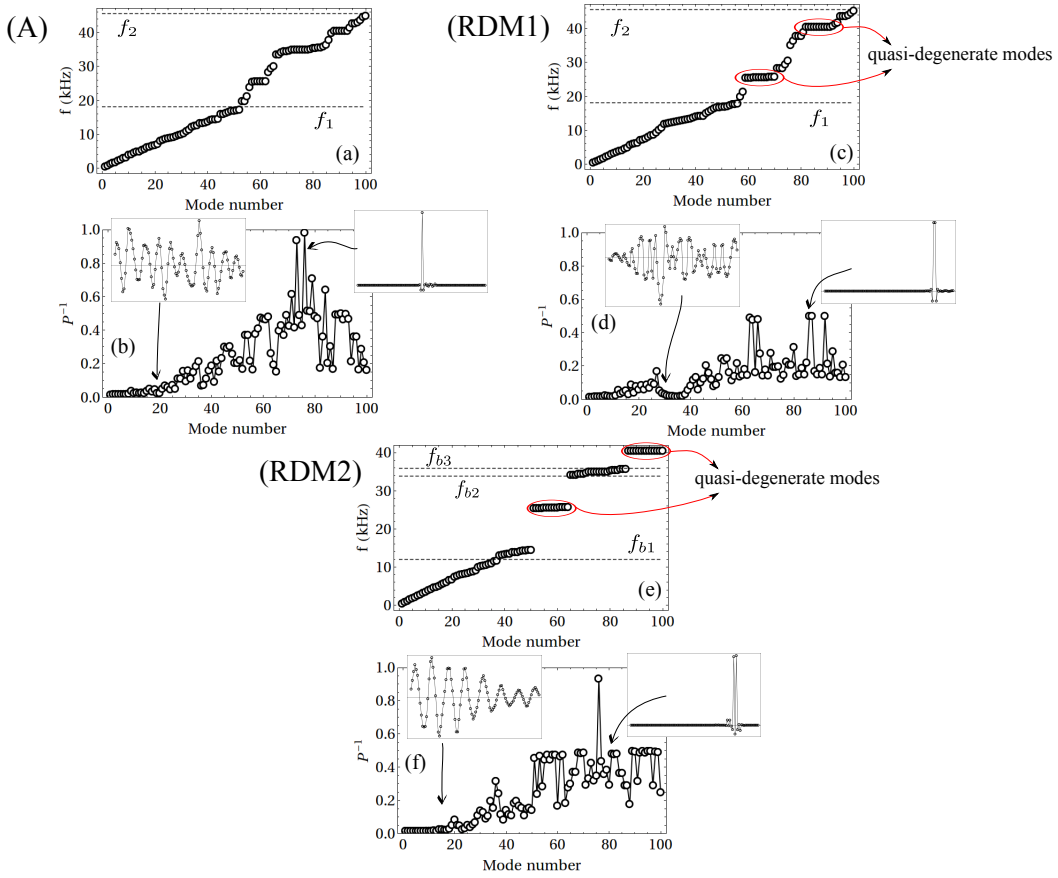


Figure 4.4: Linear spectrum and inverse participation ratio P^{-1} for different types of disorder with probability parameter $q = 0.5$ and size parameter $\xi = 0.5$. As usual, (A), (RDM1), and (RDM2) denote the Anderson-like, random dimer model 1, and random dimer model 2, respectively. The insets show examples of linear modes for both high and low frequencies. The dashed lines mark the cutoff frequency $f_i = \frac{1}{2\pi}\sqrt{\frac{4B_{ii}}{m_i}}$ associated with a homogeneous chain and the cutoff frequency $f_{bi} = \frac{1}{2\pi}\sqrt{\frac{2B_{12}}{m_i}}$ for a diatomic chain, where $m_3 = m_1 m_2/(m_1 + m_2)$. Using the parameter values described in Sec. 4.3 and $F_0 = 10$ N, we obtain $f_1 \approx 18.09$ kHz, $f_2 \approx 45.58$ kHz, $f_{b1} \approx 11.95$ kHz, $f_{b2} \approx 33.81$ kHz, and $f_{b3} \approx 35.86$ kHz.

Calculating the IPR makes it possible to directly obtain a qualitative understanding of the nature of the linear modes. In Fig. 4.4, we show the spectrum and the extent of localization (i.e., its IPR) associated with the linear modes for one realization of each of the three types of disorder. In Fig. 4.5, we show the

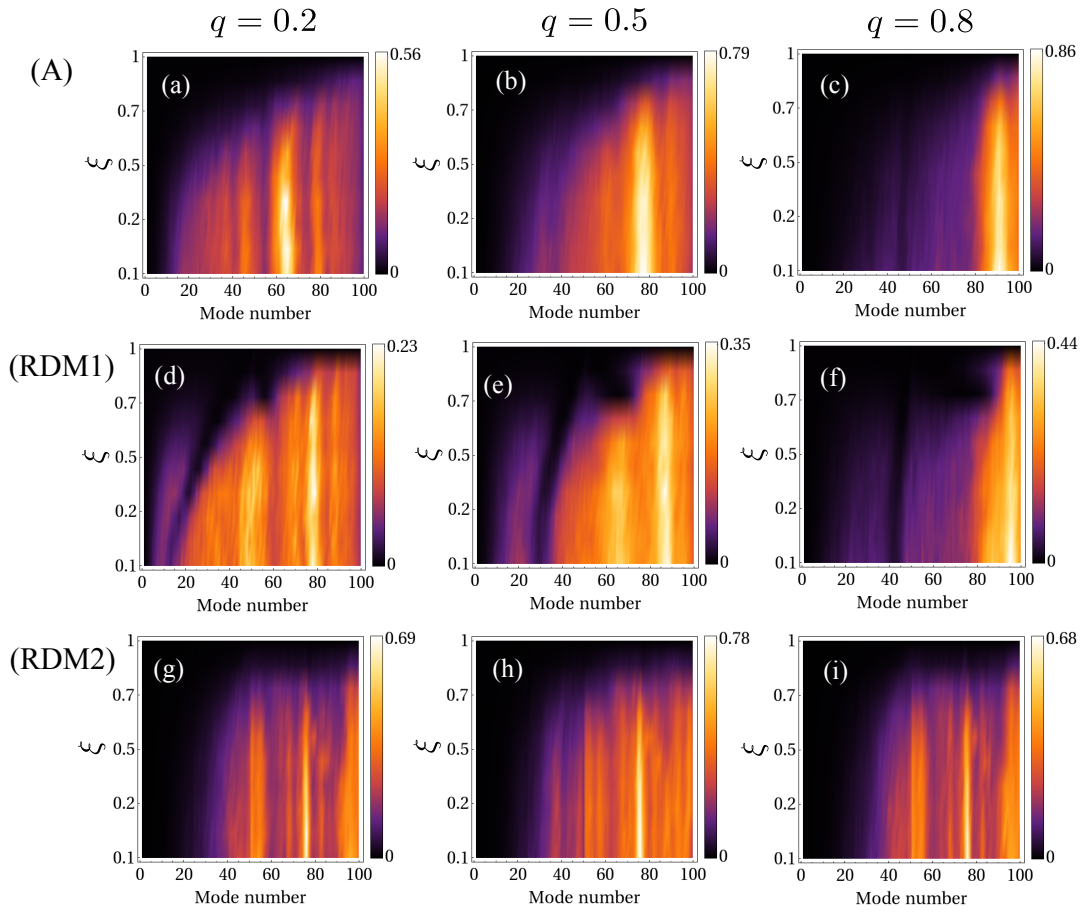


Figure 4.5: Inverse participation ratio (averaged over 100 chain configurations) as a function of the ratio $\xi = R_2/R_1$ and the mode number for different types of disordered chains and different values of the probability parameters q. The black regions are associated with delocalized waves.

mean value of the IPR over 100 realizations of each type of disordered chain as a function of the probability parameter q and the size parameter ξ. In both figures, we have sorted the modes from the one with the smallest frequency to the one with the largest frequency in an incremental way. Diagonalizing Eq. (2.12) directly yields the displacement distribution of the particles in the chain that are associated with the different modes. In this section, we use these displacement distributions to compute the IPRs that we show in Figs. 4.4 and 4.5. We also evaluate Eq. (4.14) using the energy-density distribution (given by Eq. (4.16), as we will discuss in Sec. 4.4.3), and we obtain qualitatively similar results. For

each type of disorder, we will use the energy-density distribution (see Sec. 4.4.4) to characterize the dynamical localization.

We first consider Anderson-like disorder. For frequencies $f \in (f_1, f_2)$ [see Eq. (2.10) and Fig. 4.4], we observe a complicated gap structure that includes isolated frequencies between the two band-edge frequencies. In the frequency range (f_1, f_2), there is also a small region in which P^{-1} has multiple peaks with values that are close to 1. These peaks are associated with single-node impurity modes, in which the energy oscillates primarily around one particle. As was discussed in Ref. [150], linear localized modes are bound to small particles for a single impurity, and the frequency f_{imp} of these modes is larger than the lower edge frequency f_1 of the homogeneous chain. Additionally, for a given precompression force F_0, the frequency f_{imp} depends only on the strength of the impurity, and it thus depends only on the size parameter ξ. There are also modes with $P^{-1} \approx 0.5$ that are related to double impurities. More precisely, P^{-1} is slightly *smaller* than 0.5 because the mode does not consist exactly of two particles that vibrate, as there is also a tail that decays as a function of space. Modes with a lower IPR are associated with different local configurations. For example, a mode with two small masses that vibrate with a large amplitude and are separated by a large mass that oscillates with a small amplitude has $P^{-1} \approx 0.4$. Additionally, modes with five particles effectively participating in the system dynamics have $P^{-1} \approx 0.2$, and one can make analogous statements for other values of P^{-1}.

One can interpret the probability parameter q as a measure of the density of small impurities (i.e., particles with radius R_2) in a host chain of particles with radius R_1. As $q \to 1$, the granular chain is composed almost exclusively of spheres with radius R_1, and its few small impurities generate impurity modes whose frequencies are larger than f_1. The rest of the spectrum consists mostly of an acoustic branch that is bounded above by f_1. This explains why the Anderson-like chain with $q = 0.8$ in Fig. 4.5 has an IPR whose maximum occurs near the maximum mode number (i.e., it is close to the frequency edge f_1).

When q decreases, the fraction of particles with radius R_2 increases, and the population of modes with frequencies between f_1 and f_2 increases as well. In particular, the maximum value of P^{-1} in Fig. 4.5 in the Anderson-like case (which occurs for $q = 0.2$) is about 0.55, which implies that most localized linear modes are double impurity modes instead of single impurity modes. However, the frequency of these modes does not change for a fixed value of ξ, and it is close to the frequency edge at f_1.

Another interesting feature of the Anderson-like model in granular chains is that the 0-frequency mode is extended for all values of q and ξ. In other words, it is independent of the amount of disorder and of the relative sizes of the two types of particles [27, 95]. Near $\omega = k = 0$, there is a nontrivial region in the ξ-q parameter space in which one observes extended modes in a finite-size chain. One expects the area of this region to vanish as the system size $N \to \infty$ [27]. However, the presence of this extended mode opens a channel for the transportation of energy even in a disordered chain.

For an RDM1 chain, the frequency structure is similar to that of an Anderson-like chain. However, there are several high-frequency modes, which each have frequency between f_1 and f_2, that form an almost flat structure in plots of frequency versus mode number (see Fig. 4.4). These frequencies are related to *quasi-degenerate* modes, which have almost the same frequency as each other, and such modes arise more often in RDM1 chains than in Anderson-like chains. As in the Anderson-like chain, an RDM1 chain also includes some highly localized linear modes that are related to double impurities. Nevertheless, the main difference arises in the P^{-1} distribution, which for an RDM1 chain includes an extra minimum near a frequency of $f_b \in (0, f_1)$ that depends on the parameters ξ and q. For example, when $q = \xi = 0.5$, we obtain roughly $f_b \approx 15$ kHz for $N = 100$ and the physical parameters described in Sec. 4.3. This is related to extended modes that are centered at a *nonzero* frequency. Furthermore, as one can see from Fig. 4.5, the IPR tends to be smaller for most values of ξ and q in an RDM1 chain in comparison with an Anderson-like chain. This occurs be-

cause the impurities in RDM1 chains are twice as large as those in Anderson-like chains, which implies in turn that RDM1 chains have large impurity modes.

An RDM2 chain exhibits completely different — and rather remarkable — features in its spectrum and IPR distribution from the other two types of disordered chains. To explain these differences, it is important to interpret the RDM2 system as a perturbation of a perfectly ordered diatomic chain instead of the perturbation of a monoatomic one. In fact, most of the eigenvalues for an RDM2 chain occur between the frequency edges of the ordered diatomic chain (i.e., within its pass bands). The rest of the eigenvalues are organized predominantly into almost flat distributions within the band gaps (see Fig. 4.4). An RDM2 chain tends to have more degenerate modes than an RDM1 chain. RDM2 chains also have very interesting localization properties. In Fig. 4.5, for example, we observe that the P^{-1} distributions are (on average) almost independent of the degree of disorder (i.e., on the parameter q). We also see from Fig. 4.4 that most of the degenerate modes are also equally localized. In other words, they have almost the same value of P^{-1}. To explain the features of the IPR, observe that there exist a few single impurity modes with $P^{-1} \approx 1$, but most of the localized modes consist of two (associated with $P^{-1} \approx 0.5$), three ($P^{-1} \approx 0.33$) or four ($P^{-1} \approx 0.25$) vibrating particles. Additionally, the RDM2 disorder is symmetric with respect to $q = 0.5$ by construction (so, e.g., $q = 0.2$ and $q = 0.8$ are equivalent situations).

4.4.2 Spreading and partial localization due to disorder and nonlinearity

Now, using the symplectic integrator described in Appendix A, we study the propagation of energy in long granular chains and long integration time. In this case, force distributions are particularly useful, because it is easier and more reliable to measure forces than to measure energy experimentally in granular crystals. Moreover, examining forces as a function of time allows one to indirectly measure spreading and localization. Thus, in this section, we examine how the

force evolves at specific spots in the chain and also how the force distributions are affected by changes in the precompression in homogeneous and Anderson-like disordered chains.

In Fig. 4.6, we show example force distributions from applying an excitation that consists of an initially localized displacement at the center of a homogeneous chain. For a strongly compressed chain (e.g., for $F_0 = 10$ N), the initial excitation spreads along the chain, and the dynamics arise from the decomposition of the Kronecker delta function into linear modes. However, the spreading is slightly asymmetric, because the nonlinearity cannot be neglected entirely. Increasing the nonlinearity in the system by decreasing the precompression leads to a lessening of the distribution width due a decrease in the system's sound speed. One can directly observe this effect in the force distribution, and one can also see it indirectly by examining the force at different places in the chain as a function of time. For instance, the time that it takes to detect fluctuations in the force at particles 30 and 60 sites away from the position of the initial excitation becomes longer as one decreases the precompression. Additionally, in the sonic-vacuum regime, solitary waves emerge clearly, and the energy is divided mainly into two pulses that move in opposite directions.

In the presence of disorder (see Fig. 4.7), we observe that the spatial force distribution changes abruptly (i.e., even for a small amount of disorder) from the distribution in an associated homogeneous chain. When linear effects are dominant (e.g., at $F_0 = 10$ N), the force distribution has a maximum near the position of the initial excitation, and it decays exponentially away from this point. Near the central position of the distribution, the temporal force dynamics includes large-amplitude, persistent oscillations that exist for long times. The forces in particles that are a few sites away from the center (e.g., see the particles that are 30 and 60 sites away from the center in Fig. 4.7) exhibit oscillations whose amplitudes are orders-of-magnitude lower.

When we increase the effective nonlinearity in a granular chain — in particular, in the weakly nonlinear situation, such as the one in Eq. (2.13) — resonances

of linear modes are induced by nonlinear shifts of the frequencies [38]. This leads to a nonlinear mechanism of energy exchange between the localized and extended modes in the spectrum (see Section 4.4.1), which in turn implies that energy that was previously stored in localized modes can now be carried through the system. This is done by transferring energy either to other localized modes that are spatially close or to extended modes. In short, there is more transport. Consequently, the force is distributed among a larger number of particles in the chain. This effect is analogous to phenomena that have been observed in disordered NLS and KG lattices [38], and analogous dynamics have also been observed experimentally in the context of waveguide arrays [51, 120]. Remarkably, the localization goes away completely when the precompression goes to 0, and instead a pure spreading process occurs. In other words, the localization phenomenon, in which nearly all of the energy at vanishing precompression would be partitioned into localized traveling waves (which each have a support on only a few site of the chain) [53], is modified drastically because the presence of disorder.

4.4.3 Energy distribution and second moment

As we stated in Sec. 4.4.1, characterizing whether or not dynamics is localized — and which particular transport properties can characterize localization in a quantitative way — is a difficult task [80], and it has been examined from many different perspectives by several authors. Such methods include (1) computing a localization length [134, 158], which gives information on how fast the distributions decay; (2) computing finite-time Lyapunov exponents [16, 69] to study KAM tori and chaotic dynamics; (3) directly estimating scaling properties of the energy distribution [96, 117]; and (4) calculating moments of distributions that are associated with the dynamics [27, 30, 79, 96, 120]. The calculation of moments has been especially popular, and it is particularly common to investigate the growth of the second moment of the energy distribution as a function of time, as this gives information about the width of a distribution. However, the

exclusive use of the second moment as a single-parameter description is problematic and can lead to a misunderstanding of a system's actual dynamics [38, 88], particularly in strongly nonlinear situations. Consequently, following [38, 88], we examine dynamics by computing not only the second moment but also the IPR (see Section 4.4.4).

Proceeding with our analysis, we note that the total energy of the system is conserved by the dynamics. We are thus interested in the energy distribution's second moment

$$\tilde{m}_2(t) = \frac{\sum_n (n - n_c)^2 E_n}{\sum_n E_n}\,, \tag{4.15}$$

where E_n is the energy density of the nth particle and n_c is the position of the center of the distribution. The energy density of the nth particle is given by

$$E_n(t) = K_n(t) + V_n(t)\,, \tag{4.16}$$

where

$$K_n(t) = \frac{m_n}{2}\dot{u}_n^2(t) \tag{4.17}$$

is the particle's kinetic energy and the potential energy V_n depends on the model. For example, in the linear limit, the potential energy is

$$V_n(t) = \frac{1}{2}\left[\frac{B_n}{2}\left(u_{n-1}(t) - u_n(t)\right)^2 + \frac{B_{n+1}}{2}\left(u_n(t) - u_{n+1}(t)\right)^2\right]. \tag{4.18}$$

In the weakly nonlinear regime, the potential energy is

$$V_n^W(t) = \frac{1}{2}\sum_{i=1}^{3}\left[\frac{B_n^{(i)}}{(i+1)}(u_{n-1}(t) - u_n(t))^{(i+1)} + \frac{B_{n+1}^{(i)}}{(i+1)}(u_n(t) - u_{n+1}(t))^{(i+1)}\right]. \tag{4.19}$$

Note that, for Eqs. (4.18) and (4.19), we have use regular brackets $[\dots]$ instead of $[\dots]_+$. This is because in these regimes we assume that all the particles in the granular chain remain in contact with their neighbors along the whole dynamics.

In the strongly nonlinear regime of a Hertzian potential, the potential energy is

$$V_n^H(t) = \frac{1}{2}\left\{\frac{2A_n}{5}\left[\Delta_n + u_{n-1}(t) - u_n(t)\right]_+^{5/2} + \frac{2A_{n+1}}{5}\left[\Delta_{n+1} + u_n(t) - u_{n+1}(t)\right]_+^{5/2}\right\} - \frac{1}{2}\left\{\frac{2A_n}{5}\Delta_n^{5/2} + \frac{2A_{n+1}}{5}\Delta_{n+1}^{5/2}\right\} - \frac{F_0}{2}\left\{u_{n-1}(t) - u_{n+1}(t)\right\} . \quad (4.20)$$

The two last terms in the right-hand side of the Hertzian potential energy $V_n^H(t)$ of Eq. (4.20) have minus signs, so $V_n^H(t) \to V_n^W(t)$ in the weakly nonlinear limit and $V_n^H(t) \to V_n(t)$ in the linear limit. The first term in Eq. (4.20) gives only a trivial contribution to the total energy, because it corresponds to the (constant) background energy associated with the precompression. The last term in Eq. (4.20) is a telescopic series when one considers all n, and the boundaries do not play any significant role because we are interested in the bulk dynamics. The displacement and the momentum at the edges of the chain are both exactly 0 for all times in the simulations of this Chapter.

In the linear regime and in the absence of disorder, the only possible situation after a very long time is for the system to thermalize [94, 95], so one obtains equipartition of energy between the different degrees of freedom. As a result (and as is well-known), the asymptotic spreading dynamics in a homogeneous chain is ballistic (i.e., $\tilde{m}_2(t) \sim t^2$ as $t \to \infty$) regardless of whether the initial condition is a local displacement perturbation (i.e., $\{u_n(0), \dot{u}_n(0)\} \propto \{\delta_{n,n_c}, 0\}$) or a local velocity perturbation (i.e., $\{u_n(0), \dot{u}_n(0)\} \propto \{0, \delta_{n,n_c}\}$) [27, 86]. However, introducing either disorder or nonlinearity can drastically change transport properties [38]. For example, attempting to estimate a scaling relationship for the second moment now typically produces a different exponent: $\tilde{m}_2(t) \sim t^\gamma$ as $t \to \infty$, where $\gamma \neq 2$.

However, it is not always meaningful to fit the spreading of the second moment to a power law with a single exponent [96]. When there is reasonable power-law scaling, the behavior is called "superdiffusive" when $\gamma \in (1, 2)$, "diffusive" when $\gamma = 1$, and "subdiffusive" when $\gamma \in (0, 1)$. There is no diffusion when $\gamma = 0$. Following the work by Lepri et. al. [96], we attempt to identify the

situations in which it is reasonable to construe the second moment as having a power-law scaling by using as a diagnostic the logarithmic derivative,

$$L_d = \frac{d(\ln \tilde{m}_2(t))}{d(\ln t)}\,, \tag{4.21}$$

where we calculate $\tilde{m}_2$ as a mean over some number of different realizations of the disorder. We expect that $L_d(t) \to \gamma$ when $\tilde{m}_2(t) \sim t^\gamma$ as $t \to \infty$, but that $L_d(t)$ can exhibit oscillations when the dynamics are more complicated. In our numerical computations, we estimate the logarithmic derivative using the finite-difference approximation $L_d \approx \Delta(\ln \tilde{m}_2(t))/\Delta(\ln t)$, where we discretize time as in our numerical integration. The criterion that we use to state when $\tilde{m}_2$ has a power-law scaling is

$$|L_d(t) - \gamma| < \kappa\,, \quad \text{for all} \quad t > t^*\,, \tag{4.22}$$

with κ a small parameter and t^* an arbitrary time within our observation horizon. We thereby separate the cases in which oscillations of the numerical data for the second moment are admissible as statistical fluctuations from ones in which oscillations are larger than statistical fluctuations.

It is also useful to compute the spectral density associated with the dynamics, as that allows one to identify which frequencies are involved in the dynamics [118]. We use the spatiotemporal displacement distribution to calculate the normalized spectral density

$$g(\nu) = \frac{\sum_n \bar{u}_n^2(\nu)}{\max\left\{\sum_n \bar{u}_n^2(\nu)\right\}}\,, \tag{4.23}$$

where

$$\bar{u}_n(\nu) \equiv \sum_{k=0}^{K-1} u_n(t_k) e^{-2\pi i \nu t_k / T_{\max}}\,,$$

and we use the time points $\{t_k\}_{n=0}^{K-1}$ to partition the interval $[0, T_{\max}]$ into uniform subintervals.

In Sec. 4.4.1, we discussed the effects of disorder in strongly precompressed chains of spheres, and we showed that disorder splits the spectrum into a low-frequency region (in which the modes are extended) and a high-frequency region

(in which modes tend to be localized). We now seek to explore the interplay between disorder and nonlinearity in both the strongly-precompressed (i.e., weakly nonlinear) regime and the strongly nonlinear regime (whose limiting case is a sonic vacuum). We integrate Eq. (2.1) numerically using the numerical algorithm described in Sec. 3.4.2 ("SABA$_2$C" [91, 144, 145]), which is a symplectic integrator that allows one to conserve energy and thus examine long temporal evolution. Using SABA$_2$C, the relative error in energy is between $\Delta E \approx 10^{-9}$ and $\Delta E \approx 10^{-7}$ (depending on the simulation parameters) using a reasonably small time step of $\tau \approx 1$ μs.

4.4.3.1 Displacement-perturbation initial conditions

In Fig. 4.8, we show the spatiotemporal energy distribution and the spectral density for both homogeneous and Anderson-like disordered chains for different levels of precompression and for a displacement-perturbation initial condition $\{u_n(0), \dot{u}_n(0)\}_I = \{\alpha\, \delta_{n,n_0}, 0\}$, with $\alpha = 10^{-1}$ μm. It is relevant to mention that, given an initially localized excitation, the spreading takes place within a cone $\{n_0 \pm v_g^m t, t\}$, where v_g^m is the maximum of the group velocity $\partial\omega(k)/\partial k$. Therefore, in our simulations, we consider systems that have at least $\lceil 4\Omega T \rceil$ particles, where T is the integration time and we recall that the ceiling function is $\lceil x \rceil = \min\{k \in \mathbb{Z} | k \geq x\}$. This allows us to avoid boundary effects when we investigate transport properties.

For $F_0 = 10$ N, we see that the main contribution to the dynamics comes from the linear modes (as we discussed previously). For the homogeneous case, the maximum at nonzero frequencies gives the band-edge frequencies, where the linear spectrum is denser than it is near 0 frequency. When one decreases the precompression, the band width decreases, and the spreading of waves from the linear modes becomes slower because the sound speed also decreases. One observes clear nonlinear pulses in the dynamics, and the speed of these pulses is larger than the sound speed for sufficiently small precompression. (See, for instance, the panels in Fig. 4.6 with $F_0 \leq 0.01$ N.) However, for $F_0 \to 0$, the

localized initial condition splits into traveling pulses that propagate in opposite directions. This occurs because all of the frequencies of the linear spectrum tend to 0 for $F_0 \to 0$.

The chain with Anderson-like disorder exhibits more complicated dynamics than the homogeneous chain. In Fig. 4.8, we observe Anderson-like localization for strong levels of precompression. Spikes in the spectral density indicate the modes that contribute the most to the dynamics. The highest spike is located at a high frequency, so the main contribution comes from a localized mode (see Fig. 4.4) that is presumably close to the position of the initial excitation. As we can see from the low-frequency spikes in the spectral density, the localization process occurs on top of a diffusive background pattern that arises primarily because of extended modes. As we consider weaker precompression, we observe a narrower frequency band near 0 frequency in the spectral density, analogous to our observations for homogeneous chains. Although there have been many efforts to study the interplay between disorder and nonlinearity — and their effect on spreading dynamics — most prior research has concentrated on weakly nonlinear settings. In fact, the majority of prior work has concentrated on NLS and KG lattices (see, e.g., Ref. [38] and references therein). It has been observed in these settings that transport is typically subdiffusive. A notable example in which neighboring lattice sites are not coupled linearly was investigated recently in Ref. [117], which considered strongly nonlinear lattices in which both the on-site and the inter-site interactions are nonlinear. However, those systems also exhibits subdiffusive spreading. We believe that the contribution of the on-site nonlinearity is crucial for obtaining subdiffusive spread in lattices with Anderson-like disorder, as the energy-spreading exponents in [117] differ considerably from the ones that we identify in this dissertation. Although effects from nonlinearity and disorder can separately localize energy — and, indeed, that is their general predilection, as we can see in Figs. 4.8(c,q) — exactly the opposite can occur in some situations that include both of these factors [see Figs. 4.8(o,s)]. In particular, we find when both disorder and nonlinearity are present that it is

possible for spreading to be enhanced rather than for the two features to conspire to create additional localization.

For granular chains in the strongly nonlinear regime, neither localization in the form of intrinsic localized modes nor exact localization as traveling nearly-compact waves is possible, as both of these structures are destroyed by disorder. It is also impossible to localize in an Anderson-like way, as such localization is suppressed by nonlinearity and the absence of a linear limit. Instead, the energy spreads among the particles in a peculiar but characteristic way: strongly localized (and nearly compact) waves are still present at the edges of the energy distribution during the spreading process at $F_0 = 0.001$ N [see Fig. 4.8(o)]; however, for $F_0 = 0$ N, the disorder induces multiple scattering events, which causes the wave amplitudes to decrease [see Fig. 4.8(s)].

4.4.3.2 Velocity-perturbation initial conditions

To analyze the dynamics for an initial velocity perturbation, we consider $\{u_n(0), \dot{u}_n(0)\}_{II} = \{0, \beta\,\delta_{n,n_0}\}$, and we set these perturbations to have the same energy as with the initial displacement perturbation $\{u_n(0), \dot{u}_n(0)\}_I = \{\alpha\,\delta_{n,n_0}, 0\}$. To obtain β as a function of α (or vice-versa) one needs to solve $\sum_n E_n|_I = \sum_n E_n|_{II}$. For example, to express the velocity perturbation in terms of the displacement perturbation we write

$$\beta = \sqrt{\frac{4A}{5m}\left([\Delta - \alpha]_+^{5/2} + [\Delta + \alpha]_+^{5/2} - 2\Delta^{5/2}\right)}\,. \tag{4.24}$$

Thus, in our numerical simulations we set $\beta \approx 8 \times 10^{-3}$ m/s, which is the value that we obtain for a homogeneous chain with $F_0 = 10$ N and $\alpha = 10^{-1}$ μm.

In Fig. 4.9, we show spatiotemporal energy distributions and spectral densities for both homogeneous and Anderson-like chains using an initially localized velocity perturbation. The main — and fundamental — difference compared to what we observed using displacement-perturbation initial conditions (see Fig. 4.8) comes from the spectral density. When there is strong precompression, we observe that the distribution of modes that are excited by the velocity-perturbation initial condition is denser near the 0-frequency mode than it is

elsewhere. In the disordered case, this implies that the mean contribution to the dynamics comes from extended modes rather than localized modes. This contrasts with our observations using displacement perturbations, and it leads to dynamics in which the energy spreads much faster than for displacement excitations. Moreover, for velocity perturbations, the energy that diffuses in the background is comparable to the amount of energy that remains localized. For $F_0 = 0.1$ N, we observe in both homogeneous and Anderson-like chains that a solitary wave propagates faster than the spreading pattern [see Figs. 4.9(i,k)]. For weaker precompression, the solitary wave still propagates in the homogeneous chain, but its amplitude decays in an Anderson-like chain. In particular, when $F_0 \to 0$, the solitary waves are delocalized due to scattering with defects in the disordered chain, and the energy pattern that emerges is qualitatively similar to what was observed in [128] for transport of solitary waves in the RDM2 case in a high-disorder regime.

To visualize what happens to the energy in Anderson-like granular chains, we average the energy distribution at $t = 10^{-2}$ s over 100 realizations. Fig. 4.10 shows this in logarithmic scale, where we also compare both types of initial conditions. Observe how the distribution depends on the nonlinearity. Specifically, we observe that the energy distribution grows near its edges. This happens in a narrow region (less than 30 sites) for $F_0 = 10$ and 0.1 N, and energy is localized at the edge of the distribution because traveling waves survive the disorder. This phenomenon is considerably less significant for displacement-perturbation initial conditions than for velocity-perturbation initial conditions. For $F_0 = 0$ N (sonic-vacuum regime), we also observe exponential growth of the energy distribution near its edge. In this case, however, it occurs in a wider region (about 100 and 150 sites) and with a much lower exponent than for the other two precompressed cases.

4.4.4 Transport arising from nonlinearity

To quantitatively characterize transport and localization processes, we conduct long-time simulations — up to $T_{\max} = 0.01$ s — in chains with $N = 2501$ spheres. We use long chains to avoid boundary effects during the numerical integration; no waves reach the boundary of the system in the simulation time. We compute the second moment $\tilde{m}_2$ and the IPR P^{-1} as functions of time for the three types of disorder, and we average our results over 500 realizations of a chain configuration in each case. To confirm our numerical results, we conduct several tests. For example, we compare our results from SABA_2C with those using a Runge–Kutta scheme with a very small time step (between $\tau = 0.01$ μs and $\tau = 0.001$ μs), and we obtain quantitatively the same results for the same realization of disorder.[2] We also test the SABA_2C scheme using smaller time steps ($\tau = 0.1$ μs and $\tau = 0.01$ μs) and larger system sizes ($N = 5000$ and $N = 10000$ particles), and we again obtain the same results. In the current section, we compute the IPR [see Eq. (4.14)] using the energy distribution instead of the displacement distribution. In other words, $h(v_n, \dot{v}_n) = E_n(t)$, and $\tilde{m}_2$ and P^{-1} are also based on the energy distribution.

In Fig. 4.11, we show the second moment $\tilde{m}_2$ and the IPR as functions of time for the initial condition with displacement $u_n = 10^{-1} \times \delta_{n,1251}$ μm and all particles having speeds of 0 m/s. We also show $\tilde{m}_2$ and the IPR as functions of time in Fig. 4.12, but now we use an initial condition with velocity $\dot{u}_n = 8 \times 10^{-1} \times \delta_{n,1251}$ m/s and all particles starting from the equilibrium position. For both cases, we also calculate the (discretized) logarithmic derivative of the second moment [see Eq. (4.21)] for $t \in [1, 10]$ ms as a diagnostic to test for power-law scaling. In most cases, we observe that the scaling $\tilde{m}_2 \sim t^\gamma$ persists — where the exponent γ depends strongly on the external force F_0 and on the type of disorder — according to our criterion (4.22) and within our observation time.

[2] Importantly, using SABA_2C allows much longer simulation times and a significant improvement in energy conservation in comparison to using a Runge–Kutta scheme.

However, for strong precompression and displacement-perturbation initial conditions, the second moment involves oscillations that are larger than statistical fluctuations, thereby rendering it impossible to identify a specific power-law trend for the second moment in these cases. These oscillations arise for all three types of disorder, but they are larger for Anderson-like and RMD2 chains than for RDM1 chains. Similar behavior was observed by Lepri et al. [96] for FPU chains with Anderson-like disorder. Their system is similar to our weakly nonlinear regime, but it is not precisely the same: in the FPU chains from [96], disorder arises only in the linear coupling terms; in our case, disorder arises in nonlinear coupling terms [see, e.g., Eq. (2.13)]. We estimate γ and η by taking log-log plots and fitting the numerical data between 4×10^{-3} s and 10^{-2} s with a linear function. Specifically, we use the conjugate gradient method to fit the slope for different intervals of time between 4×10^{-3} s and 10^{-2} s. We then average the slopes and calculate the standard deviation, which we estimate as the exponents and their error, respectively. We show our estimates for different values of the precompression in Table 4.1 (for γ) and Table 4.2 (for η) and also graphically in the last row of Figs. 4.11 and 4.12. We also attempt to estimate a value of γ even for the cases in which the trend of the second moment is more complicated than a power law. We highlight these cases using the symbol "*" in Table 4.1, and we stress that the reported exponents correspond to mean values of $L_d(t)$ for $t \in [4, 10]$ ms.

We also compute the second moment and IPR for several other combinations of the parameters ξ and q, and we find the same qualitative behavior: the transport is superdiffusive, and weaker precompression yields increased transport. However, we observe that the time required for the system to reach its asymptotic behavior depends on the parameters ξ and q in a nontrivial way, and it is faster for $q \geq 0.5$ in most of the cases that we tested.

A remarkable result is that, in the sonic-vacuum regime, the transport exponents are roughly independent of both the type of disorder and the type of initial condition. We obtain $\gamma \approx 1.7$ and $\eta \approx 1$. It seems that the mechanism that

underlies the superdiffusive dynamics in the sonic-vacuum regime may also be independent of the disorder and the initial condition. However, further research in this direction is necessary to truly understand the mechanisms that yield the dynamics in this regime.

We now summarize the principal results of our numerical simulations on the effect of nonlinearity on energy spreading. For all three types of disorder, the transition from strong precompression to weak precompression yields an increase in the diffusivity, as one can see from the increase of the exponent γ. Perhaps even more importantly, we find that the behavior is typically *superdiffusive*. For RDM1 and RDM2 chains, we observe superdiffusive transport for all of the precompression strengths that we consider. By contrast, for an Anderson-like chain, we observe that the spreading rate depends on the type of initial condition. It is superdiffusive for all precompression strengths for velocity perturbations, whereas we observe superdiffusive transport only for weak precompression for displacement perturbations. For strong precompression, our criterion (4.22) is not satisfied. Moreover, for sufficiently strong precompression (see, e.g., Fig. 4.11 for an Anderson-like disorder at $F_0 = 10$ N), the spreading has slowed down to the point that $L_d(t) < 1$. In other words, the spreading has become subdiffusive.

The dynamics of disordered granular chains depart substantially from the principally subdiffusive behavior that was identified previously in the KG and NLS lattices [38, 88] and even in the strongly nonlinear lattices of [117]. It is likely that the considerably enhanced diffusivity that we observe arises from the FPU nature of our lattices, as FPU and FPU-like lattices are significantly more conducive to traveling waves than, e.g., the DNLS or KG lattices that have constituted the bulk of the settings in previous studies of nonlinear disordered lattices. The observed asymptotic behavior of the IPR also illustrates a form of delocalization in which the energy is no longer split into solitary traveling waves as it is in homogeneous chains. The IPR scaling exponent η decreases as F_0 increases, which implies in turn that there is an increase in the number of particles that experience large-amplitude vibrations. This is contrary to the

expectation for the sonic-vacuum regime in the homogeneous limit, because the energy no longer is partitioned into strongly nonlinear, strongly localized waves. Instead, its spatial distribution is reasonably extended, *despite the absence of linear modes*. The delicate interplay of disorder and strong nonlinearity seems to be responsible for this intuitively unexpected outcome.

To provide reference values, Tables 4.1 and 4.2 also include our results for the computation of characteristic exponents for homogeneous granular chains. For linear homogeneous chains, one can derive analytically that $\gamma = 2$ and $\eta = -1$ [27]. The transport is ballistic for all values of F_0, but the IPR saturates below certain values of F_0. (As one can see in Figs. 4.11 and 4.12, this saturation is clear for $F_0 = 0.01$ N.) This is related to the system becoming strongly nonlinear, with no linear waves propagating, so the initial wave splits into two traveling energy-carrying pulses. These pulses are spatially localized, so P^{-1} does not grow as a function of time.

4.5 Conclusions

We characterized the localization and transport properties of one-dimensional disordered granular crystals for both uncorrelated and correlated disorders. We found, in the linear regime, that there are different extended modes that can contribute to the transport in a disordered system. We investigated the correlation properties of three types of disorder — an Anderson-like model and two random dimer models.

We showed, by direct diagonalization of the linearized granular chain in the presence of precompression, that localized linear modes are mostly impurity modes and that the spectrum of the linearized chain includes a mixture of extended and localized modes. The extended modes usually occur at low frequencies. Using a spectral perspective, we again found that RDM2 chains are rather special, as (in contrast to RDM1, which is the traditional "random dimer model") they much more closely mirror the structure of a perfectly ordered diatomic chain, instead of a homogeneous chain.

Armed with an understanding of the linear modes, we set out to quantify the nonlinear dynamics of the three different types of disordered lattices. Although the effects of nonlinearity (in the absence of disorder) in strongly nonlinear homogeneous granular crystals are known to be rather unusual — the energy tends to split into strongly localized traveling pulses, which leads to a saturation of the inverse participation ratio — we found very surprising and previously unexplored behavior when one introduces disorder into granular chains. When there is strong precompression (i.e., a very low level of nonlinearity), disorder tends to localize energy due to Anderson-like effects. Surprisingly, however, localization no longer emerges for sufficiently small precompression, as a disordered chain tends to a sort of "thermalization" as the energy spreads throughout the whole chain. In this case, neither the second moment nor the inverse participation ratio saturates, and presumably traveling waves cannot survive the presence of disorder in this regime. Nevertheless, it is conceivable in such a setting that stable localized waves may exist due to disorder. Furthermore, very recently, [148] reported that solitary-wave mobility can be enhanced in certain classes of nonlinear disordered lattices either by specific realizations of a type of disorder or with specific initial conditions. It is not clear when the joint presence of disorder and nonlinearity destroys localization, and investigating when this occurs is an important open question. In the sonic-vacuum regime of no precompression, the exponents of the temporal asymptotic scaling of the inverse participation ratio are close to -1, which is what occurs in the linear homogeneous case (in particular, for about $F_0 = 10$ N); in other words, the energy is delocalized. However, the transport remains superdiffusive rather than ballistic. In fact, we found that each of our three disordered chain models is *typically* superdiffusive, in contrast to what is known about disorder in other lattice models [38], in which a self-trapping mechanism always dominates as the strength of the nonlinearity increases (independently of the disorder).

By computing a (discretized) logarithmic derivative L_d of the second moment, we found for strongly precompressed (i.e., weakly nonlinear) chains with

initially localized displacement excitations that the spreading does not show a clear diffusive trend. In other words, the second moment behaves in a complicated way and exhibits oscillations that are larger than statistical fluctuations (analogous to what was observed in [96]). For an Anderson-like disorder and $F_0 = 10$ N, we observed that $L_d(t) < 1$ during the time interval that we consider. This behavior is clearer in Anderson-like and RDM2 chains than in RDM1 chains. By contrast, for initially localized velocity excitations, we found that L_d satisfies (4.22), and we thus observed a standard power-law growth for the second moment: $\tilde{m}_2(t) \sim t^\gamma$, with $\gamma > 1$ (i.e., superdiffusive spreading) for all types of disorder. However, for weakly precompressed (i.e., strongly nonlinear) chains, the dynamics is superdiffusive for all types of disorder and both types of initial conditions. Surprisingly, in the sonic-vacuum regime, the exponents are very similar (roughly $\gamma \approx 1.7$ and $\eta \approx 1$), and they seem to be independent of the type of disorder and of whether we use a displacement or velocity excitation as an initial condition. Moreover, granular lattices — which are inter-site interaction lattices of FPU type — appear to be far more conducive to energy transport than the previously explored KG and NLS lattices. Presumably, this situation arises from the ability of the granular lattices to transport energy in the strongly nonlinear regime in the form of robust traveling waves.

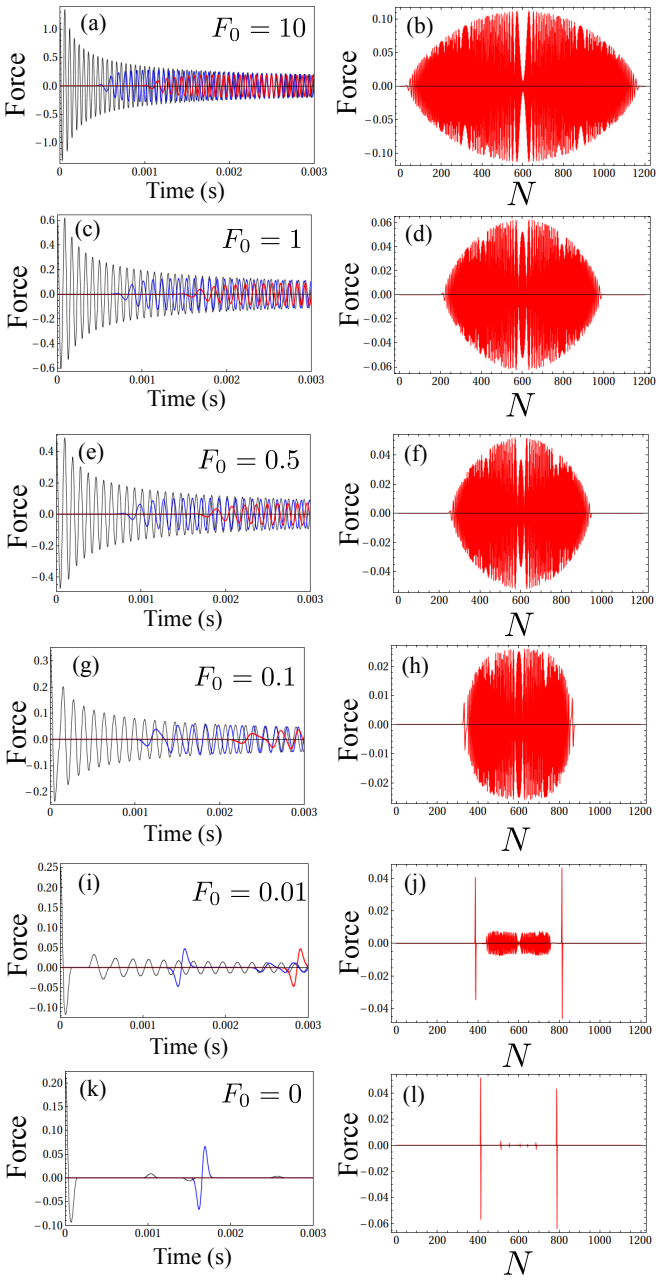


Figure 4.6: (Left) On-site force as a function of time and (right) force distribution of particles for various amounts of precompression when we apply an excitation that consists of an initially localized displacement to the center of a homogeneous granular chain. In the left panels, the black curves give the force for particle 601, the blue curves give the force for particle 631, and the red curves give the force for particle 661. The chain has $N = 1201$ particles. For each example, the initial condition is $u_n = 10^{-1} \times \delta_{n,601}$ μm. For the right panels, we give the force in Newtons at time $t = 10^{-2}$ s. In each row, the two panels show results for a chain with the same specified precompression strength.

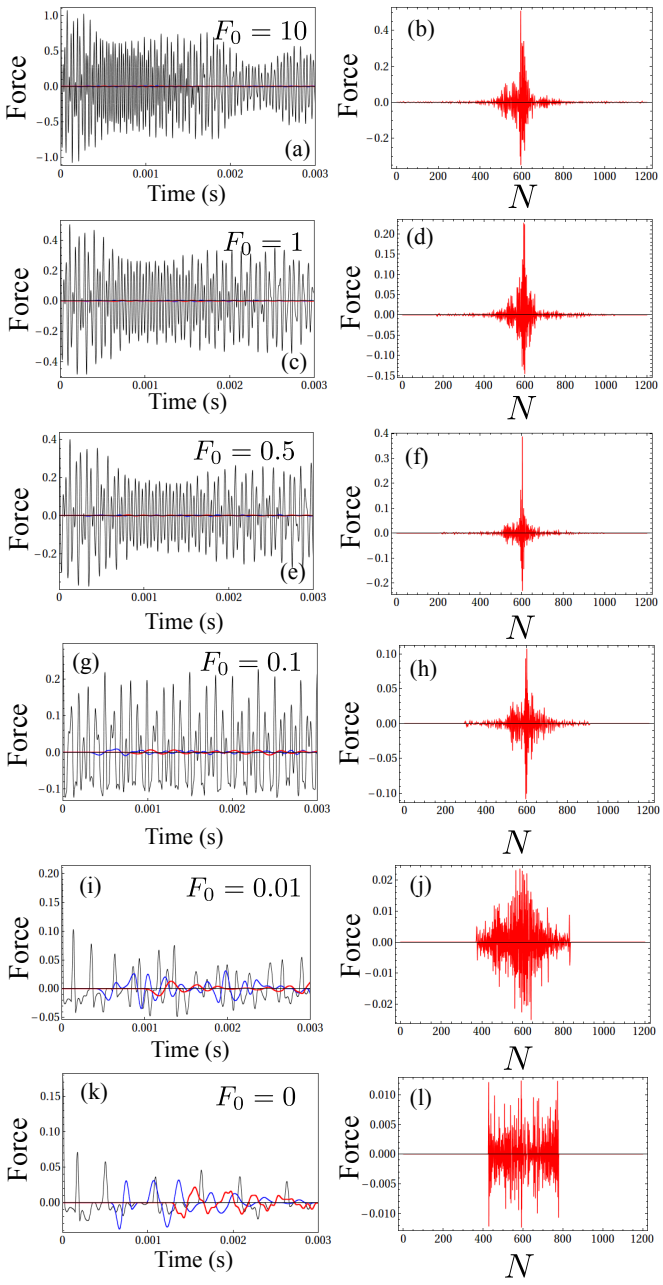


Figure 4.7: (Left) On-site force as a function of time and (right) force distribution of particles for various amounts of precompression when we apply an excitation that consists of an initially localized displacement to the center of an Anderson-like chain with a particle-size parameter of $\xi = 0.8$. In the left panels, the black curves give the force for particle 601, the blue curves give the force for particle 631, and the red curves give the force for particle 661. The chain has $N = 1201$ particles. For each example, the initial condition is $u_n = 10^{-1} \times \delta_{n,601}$ μm. For the right panels, we give the force in Newtons at time $t = 10^{-2}$ s. In each row, the two panels show results for a chain with the same specified precompression strength.

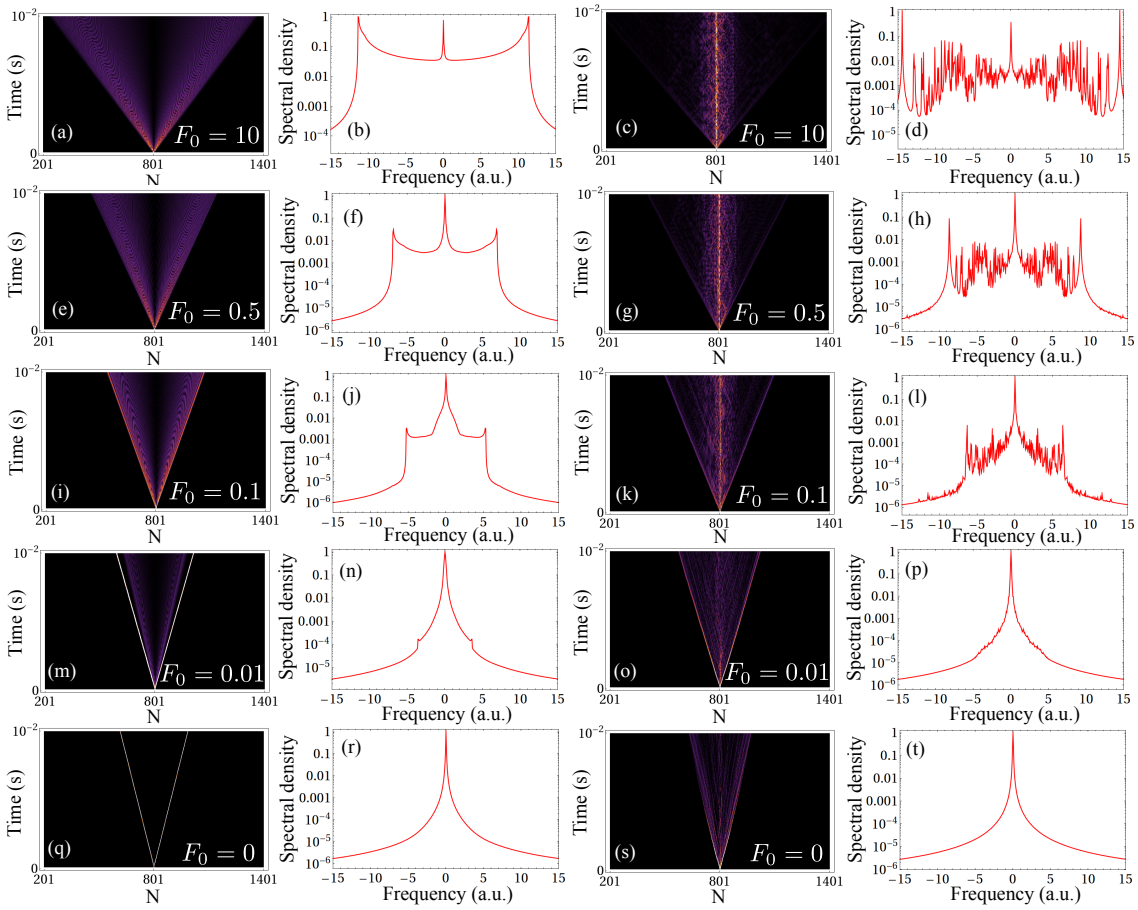


Figure 4.8: (First and third columns) Absolute values of the spatiotemporal energy distributions and (second and fourth columns) spectral density for the dynamics of an initially localized displacement perturbation $\{u_n(0), \dot{u}_n(0)\}_I = \{\alpha\, \delta_{n,801}, 0\}$, with $\alpha = 10^{-1}$ μm, for different amounts of precompression. The first two columns are for a homogeneous chain, and the last two columns are for an Anderson-like chain. Each chain has $N = 1601$ particles, though we only show the central 1201 particles in our plots of spatiotemporal energy distributions. For each example, the integration time is $T_{\max} = 10^{-2}$ s, and we give the force in units of Newtons. For each row, all panels are for a chain with the same specified precompression strength.

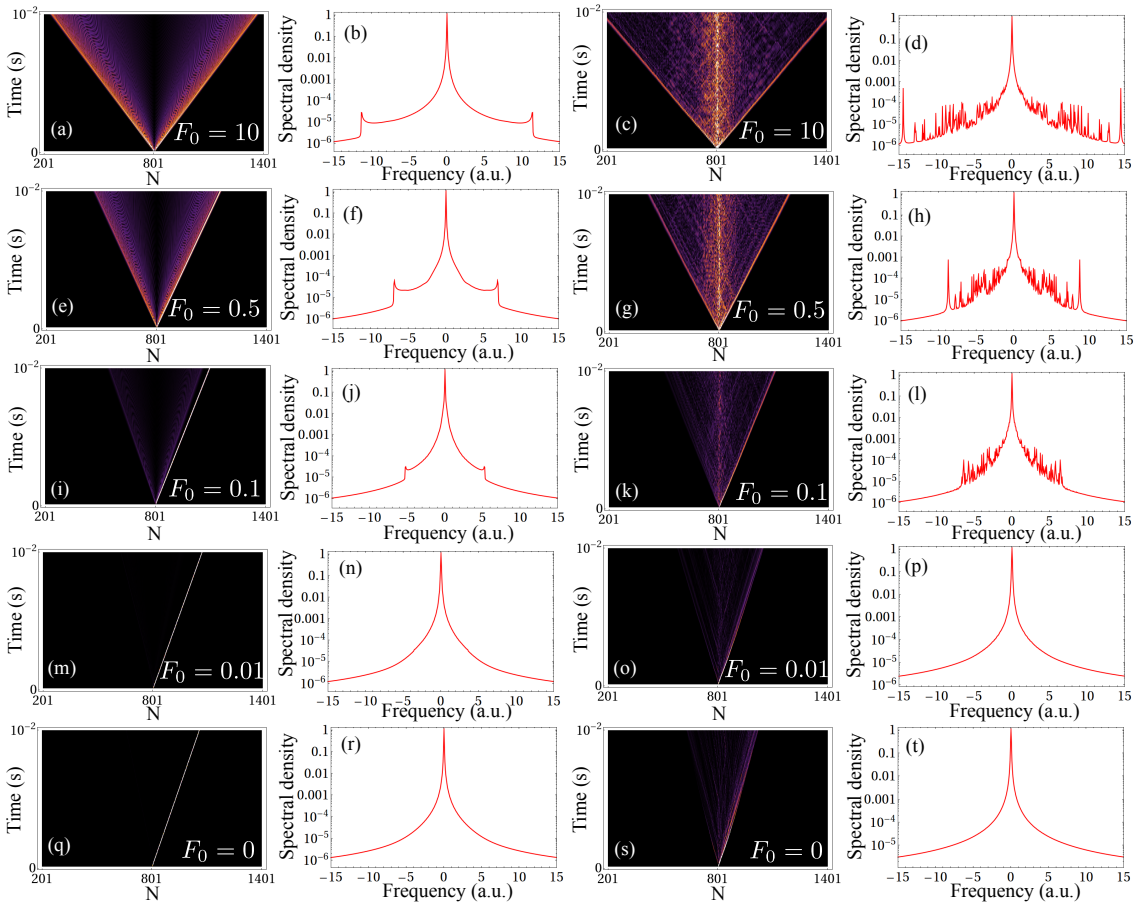


Figure 4.9: (First and third columns) Absolute values of the spatiotemporal energy distributions and (second and fourth columns) spectral density for the dynamics of an initially localized velocity perturbation $\{u_n(0), \dot{u}_n(0)\}_{II} = \{0, \beta\,\delta_{n,801}\}$, with $\beta = 8 \times 10^{-3}$ m/s, for different amounts of precompression. The first two columns are for a homogeneous chain, and the last two columns are for an Anderson-like chain. Each chain has $N = 1601$ particles, though we only show the central 1201 particles in our plots of spatiotemporal energy distributions. For each example, the integration time is $T_{\max} = 10^{-2}$ s, and we give the force in units of Newtons. For each row, all panels are for a chain with the same specified precompression strength.

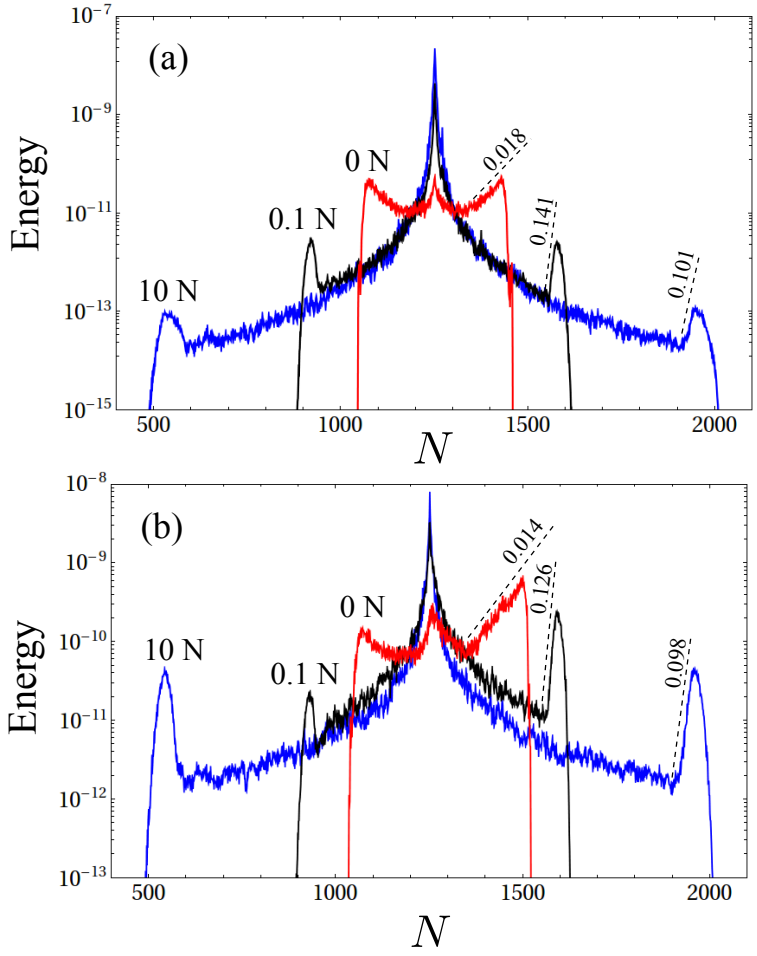


Figure 4.10: Averaged energy distribution for different levels of precompression ($F_0 = 0$, 0.1, and 10 N) at $t = 10^{-2}$ s for Anderson-like chains. We averaged the energy profiles over 100 realizations and they are shown in log-scale, for $\xi = 0.5$, $q = 0.5$, and $N = 2501$. (a) displacement-perturbation initial condition: $\{u_n(0), \dot{u}_n(0)\}_I = \{\alpha\, \delta_{n,1251}, 0\}$, with $\alpha = 10^{-1}$ μm, and (b) velocity-perturbation initial condition: $\{u_n(0), \dot{u}_n(0)\}_I = \{0, \beta\, \delta_{n,1251}\}$, with $\beta = 8 \times 10^{-3}$ m/s. Dashed lines are the exponents for the exponential growth at the edge of the energy distribution.

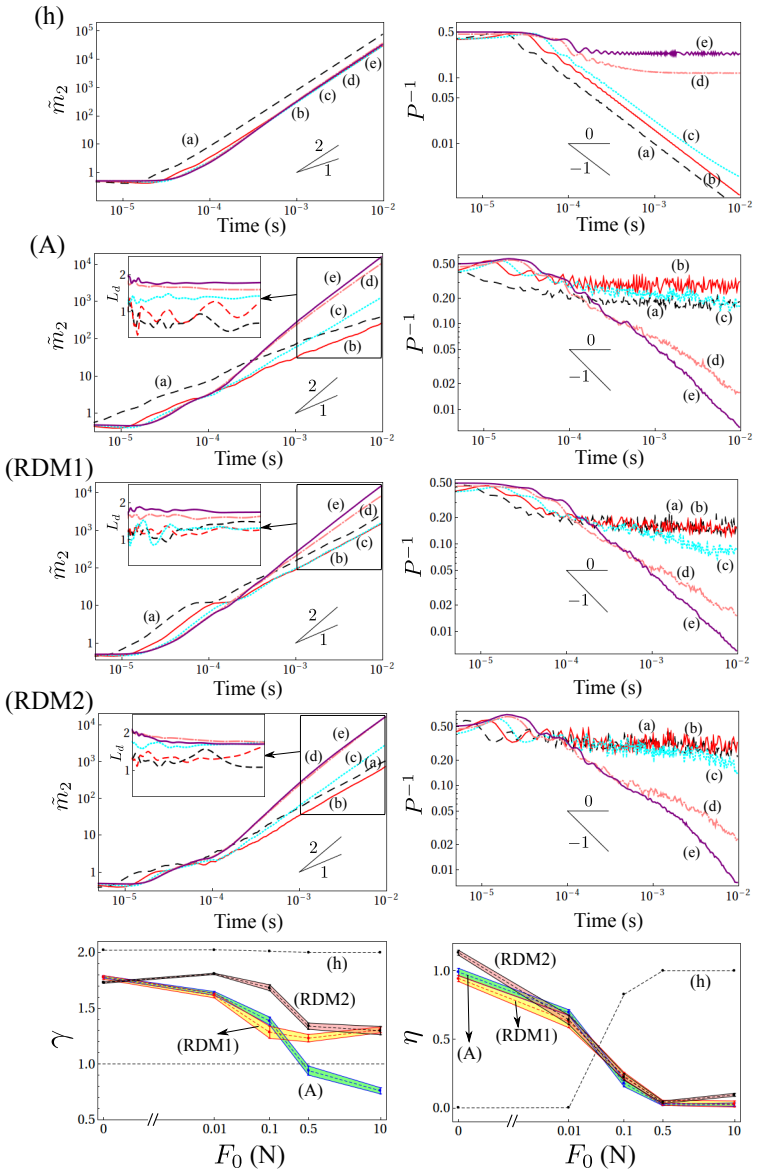


Figure 4.11: Log-log plots of (left) the second moment and (right) IPR as a function of time. Each row is associated with a certain type of disorder (or lack thereof): "h" for a homogeneous chain, "A" for the Anderson-like chain, RDM1, and RDM2. In each panel, the colors and labels indicate different amounts of precompression F_0: (a, dashed black) 10 N, (b, solid red) 0.5 N, (c, dotted cyan) 0.1 N, (d, dash-dotted pink) 0.01 N, and (e, solid purple) 0 N. To guide the eye, we show slopes of 2 (ballistic transport) and 1 (diffusive transport) for the second moment $\tilde{m}_2$ and slopes of 0 and -1 for the IPR P^{-1}. In all cases, we use chains with $N = 2501$ spheres, and the initial condition is $\{u_n(0), \dot{u}_n(0)\}_I = \{\alpha\, \delta_{n,1251}, 0\}$, with $\alpha = 10^{-1}$ μm. For the Anderson-like, RDM1, and RDM2 chains, we use the parameter values $\xi = 0.5$ and $q = 0.5$, and we average over 500 different realizations of a disordered configuration in each case. The insets in the second, third, and fourth rows show the (discretized) logarithmic derivative of the second moment for $t \in [1, 10]$ ms. In the last row, we show exponents γ and η that we obtain for $t \in [4, 10]$ ms by fitting the data using the relations $\tilde{m}_2 \sim t^{\gamma}$ and $P^{-1} \sim t^{-\eta}$.

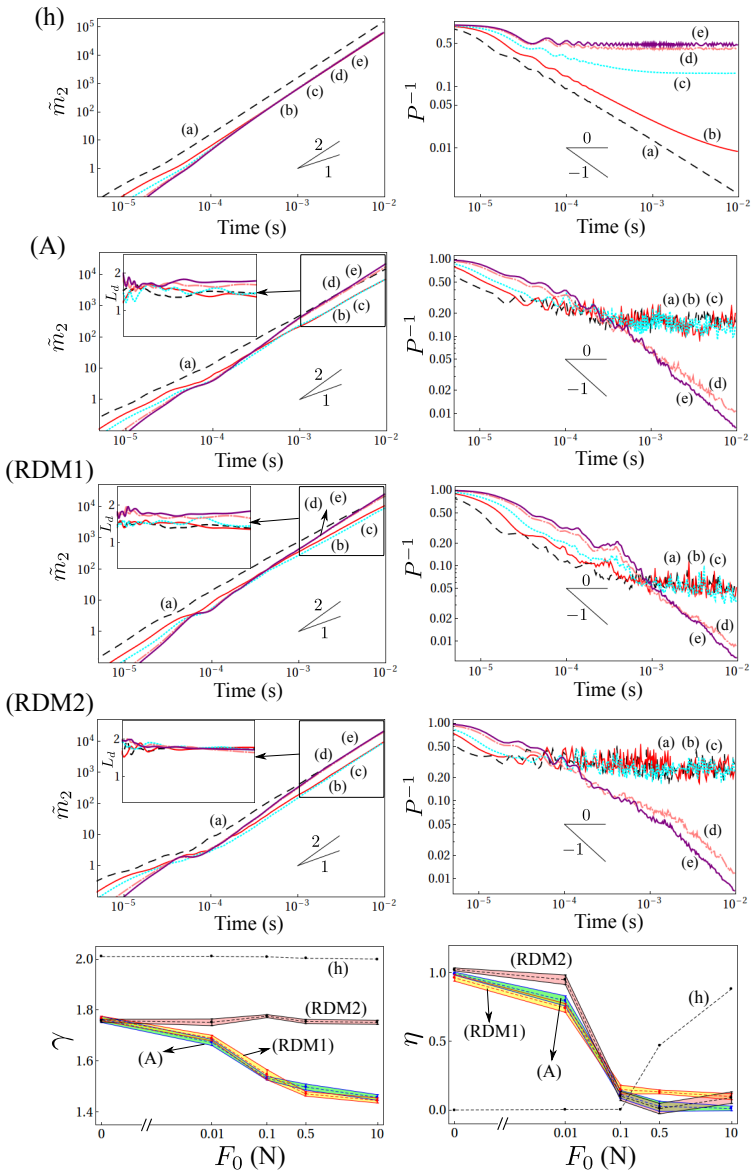


Figure 4.12: Log-log plots of (left) the second moment and (right) the IPR as a function of time. Each row is associated with a certain type of disorder (or lack thereof): "h" for a homogeneous chain, "A" for the Anderson-like chain, RDM1, and RDM2. In each panel, the colors and labels indicate different amounts of precompression F_0: (a, dashed black) 10 N, (b, solid red) 0.5 N, (c, dotted cyan) 0.1 N, (d, dash-dotted pink) 0.01 N, and (e, solid purple) 0 N. To guide the eye, we show slopes of 2 (ballistic transport) and 1 (diffusive transport) for the second moment $\tilde{m}_2$ and slopes of 0 and -1 for the IPR P^{-1}. In all cases, we use chains with $N = 2501$ spheres, and the initial condition is $\{u_n(0), \dot{u}_n(0)\}_{II} = \{0, \beta\,\delta_{n,1251}\}$, with $\beta = 8 \times 10^{-3}$ m/s. For the Anderson, RDM1, and RDM2 chains, we use the parameter values $\xi = 0.5$ and $q = 0.5$, and we average over 500 different realizations of a disordered configuration in each case. The insets in the second, third, and fourth rows show the (discretized) logarithmic derivative of the second moment for $t \in [1, 10]$ ms. In the last row, we show exponents γ and η that we obtain for $t \in [4, 10]$ ms by fitting the data using the relations $\tilde{m}_2 \sim t^{\gamma}$ and $P^{-1} \sim t^{-\eta}$.

Table 4.1: Numerical estimates for the scaling exponent γ for a homogeneous chain (h), Anderson-like chains (A), RDM1 chains (RDM1), and RDM2 chains (RDM2) using the same data as in Fig. 4.11. Recall that, we compute γ using the scaling $\tilde{m}_2 \sim t^{\gamma}$ as $t \to \infty$, and the asterisks (*) highlight the cases in which $\tilde{m}_2$ behaves markedly different from a power law. The sets of columns in the middle and right side of the table represent, respectively, the data associated with displacement-perturbation and velocity-perturbation initial conditions.

F_0 (N)	(h)	(A)	(RDM1)	(RDM2)	(h)	(A)	(RDM1)	(RDM2)
10	2.000	$0.759 \pm 0.028(*)$	1.306 ± 0.026	$1.299 \pm 0.037(*)$	2.000	1.457 ± 0.011	1.445 ± 0.010	1.752 ± 0.008
0.5	2.000	$0.941 \pm 0.041(*)$	1.231 ± 0.033	$1.339 \pm 0.028(*)$	2.003	1.498 ± 0.012	1.471 ± 0.009	1.755 ± 0.008
0.1	2.012	1.385 ± 0.035	1.284 ± 0.054	1.684 ± 0.026	2.009	1.532 ± 0.007	1.546 ± 0.020	1.776 ± 0.006
0.01	2.025	1.634 ± 0.016	1.614 ± 0.021	1.808 ± 0.006	2.011	1.673 ± 0.012	1.690 ± 0.011	1.752 ± 0.013
0	2.020	1.781 ± 0.011	1.776 ± 0.017	1.731 ± 0.007	2.010	1.763 ± 0.012	1.767 ± 0.009	1.758 ± 0.006

Table 4.2: Numerical estimates for the scaling exponent η for a homogeneous chain (h), Anderson-like chains (A), RDM1 chains (RDM1), and RDM2 chains (RDM2) using the same data as in Fig. 4.11. Recall that, we compute η using the scaling $P^{-1} \sim t^{-\eta}$ as $t \to \infty$. The sets of columns in the middle and right side of the table represent, respectively, the data associated with displacement-perturbation and velocity-perturbation initial conditions.

F_0 (N)	(h)	(A)	(RDM1)	(RDM2)	(h)	(A)	(RDM1)	(RDM2)
10	1.000	0.025 ± 0.012	0.029 ± 0.022	0.096 ± 0.011	0.882	0.011 ± 0.017	0.097 ± 0.022	0.090 ± 0.042
0.5	1.000	0.023 ± 0.006	0.037 ± 0.019	0.042 ± 0.009	0.470	0.027 ± 0.037	0.132 ± 0.014	0.010 ± 0.038
0.1	0.828	0.181 ± 0.026	0.235 ± 0.025	0.226 ± 0.024	0.004	0.114 ± 0.029	0.149 ± 0.032	0.102 ± 0.033
0.01	0.002	0.695 ± 0.021	0.631 ± 0.046	0.642 ± 0.034	0.003	0.795 ± 0.037	0.744 ± 0.032	0.949 ± 0.035
0	0.001	0.991 ± 0.027	0.944 ± 0.022	1.132 ± 0.018	0.000	0.994 ± 0.011	0.963 ± 0.024	1.025 ± 0.011

Chapter 5

QUASIPERIODIC GRANULAR CRYSTALS

5.1 Introduction

Quasicrystals are solids whose structure is ordered but not periodic [64]. For many years, it was thought that quasicrystals could only be produced artificially. However, almost a decade ago, the first natural quasicrystal was found in Russia [9]. A common type of quasicrystal arises when atoms are arranged so that they possess symmetries, such as 5-fold symmetry, that are forbidden to periodic crystals[1]. A famous two-dimensional (2D) example is a Penrose tiling [126]. More generally, quasiperiodic structures can exist in any number of dimensions as structures with a broken translational symmetry. In 1D, the most common models used in the study of quasiperiodic systems are a Fibonacci quasicrystal [97] and the Aubry–André (AA) model [5]. These models are topologically equivalent to each other [82], in the sense that it is possible to continuously deform one into another without closing any bulk gaps.

A key feature of quasiperiodic potentials, arising prominently in the study of

This chapter is based on an paper published in *Phil. Trans. Roy. Soc. A* [110].

[1]By the *crystallographic restriction*, crystals can only have certain rotational symmetries: 2-fold, 3-fold, 4-fold, or 6-fold symmetry [101].

Schrödinger equations [5], is the transition from a "metallic" phase, in which all eigenstates are delocalized, to an "insulating" phase, in which they are localized. This is analyzed in [6, 47] and the experimentally corroborated in [85]. It is of considerable interest to extend these studies in various ways, specially in nonlinear systems (see, e.g., the work of [40] and references therein), many-body systems, discrete systems, and settings with controllable interactions. For example, there have been relevant investigations in both bosonic and fermionic settings [61, 111].

In the present Chapter we study the effects of quasiperiodicity in strongly precompressed granular chains [121, 142], in which neighboring particles interact with each other according to a Hertzian potential. Our aim is to illustrate that localization of eigenmodes can occur in quasiperiodic granular chains and to explore the conditions — with respect to both models and experimental set-ups — in which it occurs. We illuminate these conditions by comparing a variety of different models with one or both of on-site and off-site quasiperiodic structures.

This Chapter is organized as follows. First, we briefly review the AA model. In Section 5.3, we present three models of 1D quasiperiodic lattices: two with on-site quasiperiodicity and one with off-site quasiperiodicity. In Section 5.4, we linearize the governing equations of our three models. In Section 5.5, we demonstrate that such models may possess a Hofstadter butterfly structure and also we propose a method to recover it from the dynamics. In Section 5.6, we examine energy transport and localization in our models.

5.2 A brief review of the Aubry–André model

The prototypical form of the Aubry–André (AA) model at the level of a tight-binding model is

$$E\Psi_n = \Psi_{n+1} + \Psi_{n-1} + \lambda V(nq + r)\Psi_n \,, \tag{5.1}$$

where Ψ is a wavefunction, n indexes the lattice site, E is energy, and V is a potential. We suppose that the on-site energy is modulated by a lattice distortion

with wave vector $q \in \mathbb{R}$, which is incommensurate with 2π and has phase r. We also suppose that $V(x) = V(x + 2\pi n)$, where $x \in \mathbb{R}$ and $n \in \mathbb{Z}$.

In [5], Aubry and André proved several fundamental properties of the eigenmodes of (5.1). They showed that a ground state exists and that it undergoes a transition from analyticity for $\lambda < \lambda_c$ to nonanalyticity for $\lambda > \lambda_c$ for certain $\lambda_c(q)$ and when q is not a Liouville number. That is, $q \in \mathbb{R} \setminus \mathbb{Q}$ and there exist γ and r such that

$$\left| \frac{q}{2\pi} - \frac{p_1}{p_2} \right| > \gamma \frac{1}{p_2^r} \tag{5.2}$$

is satisfied for any rational number p_1/p_2.

Aubry and André also showed, using a perturbative approach, that the analyticity-breaking causes the eigenmodes of (5.1) to have very rich spatial properties. Specifically, one can write the eigenmodes of the modulated system as

$$\Psi_n(k) = e^{ikn} + \lambda \sum_{m=-\infty}^{\infty} \frac{v_m e^{im(qn+h)}}{2[\cos(mq + k) - \cos(k)]}\,, \tag{5.3}$$

where v_m are the coefficients of the Fourier expansion of V. The eigenmodes and eigenvalues for $\lambda = 0$ are given by e^{ikn} and $2\cos(k)$, respectively. For the series in (5.3) to be convergent, one needs to satisfy a Diophantine condition. That is, there exist two positive constants K and β such that

$$\left| \frac{k}{\pi} + m\frac{q}{2\pi} - n \right| > \frac{K}{m^{1+\beta}} \tag{5.4}$$

for any integers m and n.

For the sake of simplicity, consider the special case in which the phase $r = 0$ and $V(\xi n) = \cos(2\pi\xi x)$, where ξ equals the golden ratio $(1+\sqrt{5})/2$. So, Eq. (5.1) takes the form: $E\Psi_n = \Psi_{n+1} + \Psi_{n-1} + \lambda\cos(2\pi\xi n)\Psi_n$. In this case, Aubry and André showed that for $\lambda > \lambda_c = 2$, all of the eigenmodes of (5.1) are exponentially localized, as in the Anderson model (in which the potential V is disordered rather than quasiperiodic)[3], with the same characteristic localization length

$$\zeta = \frac{1}{\ln\left(\frac{\lambda}{2}\right)}\,. \tag{5.5}$$

That is, Ψ_n decays asymptotically as $e^{-n/\zeta}$ as $n \to \infty$. However, when $\lambda < 2$, most eigenmodes are given by extended, modulated plane waves. Interestingly, this implies that the loss of analyticity is also associated with a transition at λ_c to spatial localization of the eigenmodes, where $\lambda_c = 2$ in this specific example. This transition is called a *localization transition* or *Aubry–André transition*. This result is a generic phenomenon in Schrödinger lattices, and it is thus relevant for a diverse variety of physical systems [85, 108, 135, 157], including photonic lattices, Bose–Einstein condensates, and many others. Additionally, the spectra of the corresponding Schrödinger operators (with two or even more frequencies) is a topic of intense mathematical interest; see, e.g., [45] and references therein.

5.3 Adding quasiperiodicity to granular chains

Several recent studies have generalized conventional granular chains in various ways. They have yielded several interesting insights, and they promise to result in a host of others in the coming years [20, 132]. One type of a generalized granular chain is a *cradle system* [62], in which particles are attached to linear oscillators, enabling the use of on-site potentials in a way that is independent of particle–particle interactions. Several potential realizations of such a setting were given in [63] (although they have yet to be implemented experimentally, to the best of our knowledge). Another fascinating variant arises from examining a chain of particles with internal resonators, such as by coupling a secondary particle inside a principal one. This leads to a locally-resonant granular chain, which is sometimes called a *mass-in-mass* (or *mass-with-mass*, if the secondary particle is external) chain [12, 59, 74]. Additionally, the use of particles with non-spherical geometries can drastically modify particle–particle interactions. For instance, with cylindrical particles, although one has the same functional relation between the force and the displacements as with spherical particles, one can tune the magnitude of such interactions by changing the contact angle between adjacent cylinders [75, 99].

We will consider granular chains with all of the above types of variations. The equations of motion in our general setting are

$$\ddot{u}_n = \underbrace{\alpha_n[\delta_n + u_{n-1} - u_n]_+^{3/2} - \alpha_{n+1}[\delta_{n+1} + u_n - u_{n+1}]_+^{3/2}}_{\text{Hertzian interaction}} - \underbrace{\beta_n u_n}_{\text{elastic restitution}} - \underbrace{\gamma_n(u_n - v_n)}_{\text{mass-in-mass interaction}} , \tag{5.6}$$

$$\ddot{v}_n = \gamma_n(u_n - v_n) , \tag{5.7}$$

where u_n is the displacement of the nth particle (where $n \in \{1, 2, \ldots, N\}$) measured from its equilibrium position in the initially compressed chain, v_n is the displacement of the nth interior mass (when one particle is located inside another).

In our subsequent discussions, we will consider various special cases of (5.6) and (5.7), depending on the type of particle that we use to construct chains. Specifically, we work with three different models: two of them have spherical particles, and one has cylindrical particles. For our analysis and computations, we assume that α_n, β_n, and γ_n vary sinusoidally in space according to the following formulas:

$$\alpha_n = \bar{\alpha}_1 + \bar{\alpha}_2 \cos(2\pi n\xi) , \tag{5.8}$$

$$\beta_n = \bar{\beta}\,[1 + \cos(2\pi n\xi)] , \tag{5.9}$$

$$\gamma_n = \bar{\gamma}\,[1 + \cos(2\pi n\xi)] , \tag{5.10}$$

where ξ is the golden mean $\frac{\sqrt{5}+1}{2}$ (unless we explicitly state otherwise), $\bar{\alpha}_1 > \bar{\alpha}_2 \geq 0$, and $\bar{\beta}$, $\bar{\gamma} \geq 0$. For simplicity, we separately examine the effects of (5.8)–(5.10). This leads to three different models in which it may be possible to observe an AA transition. In Eqs. (5.8)–(5.10), $\bar{\alpha}_2$, $\bar{\beta}$, and $\bar{\gamma}$ are the quasiperiodic parameters that determine the strengths of the modulations for the different terms in Eqs. (5.6) and (5.7).

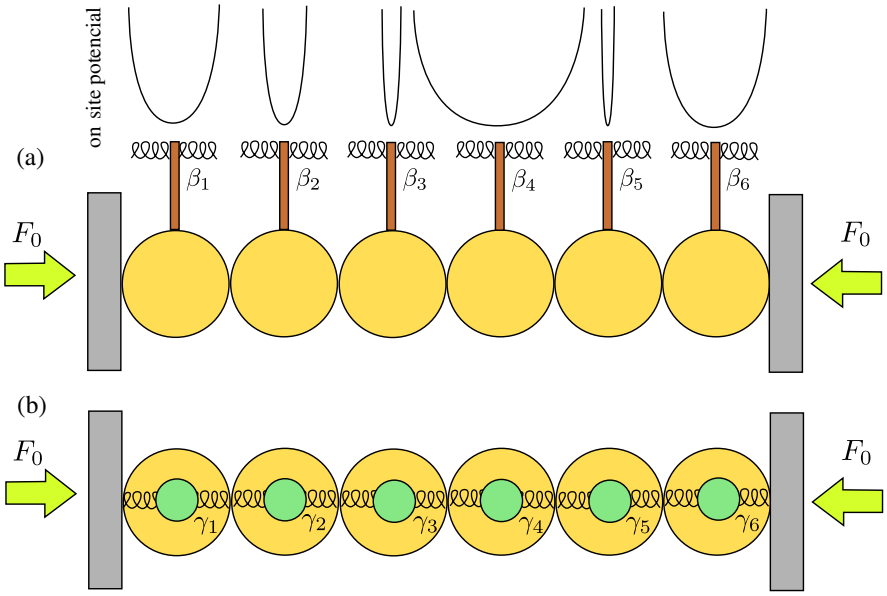


Figure 5.1: Schematics of (a) model Ia and (b) model Ib.

5.3.1 On-site quasiperiodicity: two different variants of the AA model using spherical particles

In this section, we discuss the effect of an on-site quasiperiodicity on the dynamics of a granular chain by considering chains of spherical particles with local potentials. We set $\bar{\alpha}_2 = 0$ in Eq. (5.8), so the coupling parameter α_n is given by $\alpha_n = A_n/m_n$, where

$$A_n = \frac{4E_{n-1}E_n\left(\frac{R_{n-1}R_n}{R_{n-1}+R_n}\right)^{1/2}}{3\left[E_n(1-\nu_{n-1}^2)+E_{n-1}(1-\nu_n^2)\right]}, \tag{5.11}$$

and the nth particle has elastic modulus E_n, Poisson ratio ν_n, radius R_n, and mass m_n. We assume that the particles are identical, so $E_n = E$, $\nu_n = \nu$, $R_n = R$, and $m_n = m$. This, in turn, implies that $\alpha_n = \bar{\alpha}_1$, and we let $\bar{\alpha}_1 = 1$ without loss of generality.

5.3.1.1 Model Ia: $\bar{\beta} \neq 0$ and $\bar{\alpha}_2 = \bar{\gamma} = 0$

Suppose that the particles in the chain are attached to a mechanical restitution mechanism, such that there is a linear force in the equations of motion (5.6) and

(5.7). In the limit of small angles, this can describe the well-known Newton's cradle, a system in which particles are aligned in one dimension and are suspended from a ceiling by strings so that the particles collide with each other along one dimension and oscillate. In the top panel of Fig. 5.1, we show a schematic of this system. Studies of this system have focused primarily on waves that arise by releasing one of the particles at one end with some velocity [63]. This produces a transfer of energy across the chain in the form of traveling waves [62]. Mulansky and Pikovsky studied disorder in closely related (nonlinearly coupled, and locally linear or nonlinear) oscillator systems [117], showing numerically and using a fractional-nonlinear-diffusion approach that energy transport is subdiffusive. This helps further motivate the study of modulated systems, such as the AA model, in granular chains. In our case, the equation of motions are

$$\ddot{u}_n = [\delta + u_{n-1} - u_n]_+^{3/2} - [\delta + u_n - u_{n+1}]_+^{3/2} - \bar{\beta}\,[1 + \cos(2\pi n\xi)]\,u_n\,, \qquad (5.12)$$

where $\bar{\beta} > 0$. In other words, the Hookean spring constants are positive for all n.

5.3.1.2 Model Ib: $\bar{\gamma} \neq 0$ and $\bar{\alpha}_2 = \bar{\beta} = 0$

We now consider chains composed of particles that include an internal degree of freedom (i.e., mass-in-mass particles) [59]. Previous works have focused on the generation [12, 74], of such lattices, their traveling-wave solutions [154, 155], and their (bright and dark) breather-like excitations [102, 103]. These works illustrate that coherent structures and their dynamics are enriched significantly by the presence of the internal degree of freedom (DOF). To give just one example, incorporating an internal DOF in the particles can lead to nonlocal solitary waves with non-vanishing tails (so-called "nanoptera"), which have been observed experimentally in woodpile granular chains [77]. In our setting, we envision embedding a particle in the interior of each host particle, such that a particle and its interior mass are coupled via a linear restitution mechanism (such as a Hookean spring).

The equations of motion, upon quasiperiodic modulation of the mass-in-mass (MiM) resonator, are

$$\ddot{u}_n = [\delta + u_{n-1} - u_n]_+^{3/2} - [\delta + u_n - u_{n+1}]_+^{3/2} - \bar{\gamma}\left[1 + \cos(2\pi n\xi)\right](u_n - v_n)\,, \tag{5.13}$$

$$\ddot{v}_n = \bar{\gamma}\left[1 + \cos(2\pi n\xi)\right](u_n - v_n)\,, \tag{5.14}$$

where $\bar{\gamma} > 0$.

5.3.2 Off-site quasiperiodicity: the AA model with cylindrical particles

Another approach for incorporating quasiperiodicity in a granular chain is by tuning particle–particle interactions. In existing experimental set-ups, to implement an AA model, one can use chains of cylindrical particles (rather than spherical ones). We are motivated by recent experiments [75], where it was demonstrated that cylindrical particles offer more flexibility than spherical particles for tuning particle–particle interactions, as one can change the contact angle between contiguous cylinders. Moreover, spatial and even temporal (periodic) variation of contacts between cylindrical particles has been proposed as an efficient way for implementing various functionalities, including that of an acoustic transistor in [99].

5.3.2.1 Model II: $\bar{\alpha}_2 \neq 0$ and $\bar{\beta} = \bar{\gamma} = 0$

To give equations of motion for a chain of cylindrical particles, we first need to know the form of the Hertzian coefficient in this case. For identical cylinders, the interaction coefficients are [70]

$$\alpha_n(\phi_n) = \frac{Y}{m} g_1(\phi_n)\left[g_2(\phi_n)\sqrt{g_3(\phi_n)}\right]^{1/2}\,, \tag{5.15}$$

where Y depends on the physical parameters of the particles, m is the mass of a particle, and ϕ_n is the contact angle between cylinders $n-1$ and n and it is

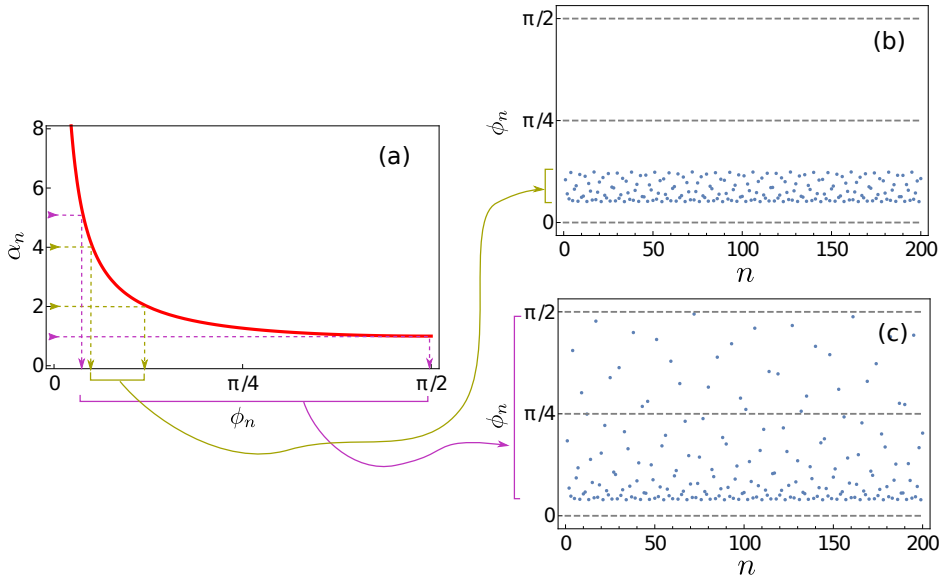


Figure 5.2: (a) Interaction coefficient α_n for model II as a function of the contact angle ϕ_n between adjacent cylinders. In panels (b) and (c), we show the contact-angle distributions for two cases: (i) $\bar{\alpha}_1 = 3$ and $\bar{\alpha}_2 = 1$ and (ii) $\bar{\alpha}_1 = 3$ and $\bar{\alpha}_2 = 3$. We use arrows to represent the mapping process that we describe in the text.

defined mod $\pi/2$. Explicit forms of Y and g_i are

$$
\begin{aligned}
Y &= \frac{2E\sqrt{R}}{3(1-\nu^2)}\,, \\
g_1(\phi_n) &= \sqrt{\frac{1}{\sin(\phi_n)}}\left(\frac{2K\left[e(\phi_n)\right]}{\pi}\right)^{-3/2}\,, \\
g_2(\phi_n) &= \frac{4}{\pi e^2(\phi)}\,, \\
g_3(\phi_n) &= \left(\frac{a^2}{b^2}E\left[e(\phi_n)\right] - K\left[e(\phi_n)\right]\right)\left(K\left[e(\phi_n)\right] - E\left[e(\phi_n)\right]\right)\,,
\end{aligned}
$$

where E is the elastic modulus, ν is the Poisson ratio, R is the radius of the circular cross section of the cylinders, and $e = \sqrt{1-(b/a)^2}$ is the eccentricity of the contact area, a is the semi-major axis length of the ellipse, and b is its semi-minor axis length. One can approximate the quotient b/a by $[(1-\cos\phi_n)/(1+\cos\phi_n)]^{2/3}$. The functions K and E, respectively, are the complete elliptical integrals of the first and second kinds [125]. They are

$$
\begin{aligned}
K(k) &= \int_0^{\pi/2} \frac{d\theta}{\sqrt{1-k^2\sin^2\theta}}\,, \\
E(k) &= \int_0^{\pi/2} \sqrt{1-k^2\sin^2\theta}\,d\theta\,.
\end{aligned}
$$

This yields the following equations of motion:

$$
\ddot{u}_n = \alpha_n(\phi_n)[\delta_n + u_{n-1} - u_n]_+^{3/2} - \alpha_{n+1}(\phi_n)[\delta_{n+1} + u_n - u_{n+1}]_+^{3/2}\,. \tag{5.16}
$$

One can then control the interactions between particles by changing ϕ_n [99]. This raises the following question of what the distribution of contact angles $\{\phi_n\}$ has to be to obtain $\alpha_n(\phi_n) = \bar{\alpha}_1 + \bar{\alpha}_2\cos(2\pi\xi n)$. We address this issue by numerically inverting Eq. (5.15), so that quasiperiodic variation of α_n yields a quasiperiodic variation of angles in the interval $(\phi_{\min}, \phi_{\max})$. In Fig. 5.2, we show the contact-angle distributions generated in two cases: (i) when $\bar{\alpha}_1 = 3$ and $\bar{\alpha}_2 = 1$ and (ii) $\bar{\alpha}_1 = 3$ and $\bar{\alpha}_2 = 3$. We also note that $\alpha(\phi_n) \to \infty$ as $\phi_n \to 0$ and that $\alpha_n(\phi_n)$ has a lower bound at $\phi_n = \pi/2$.

5.4 Linear approximation

Following the same procedure as in Section 2.1.1, we can derive linear versions of Eq. (5.16) by adding a strong precompression. This yields

$$\begin{aligned} \ddot{u}_n &= B_n u_{n-1} + B_{n+1} u_{n+1} - (B_n + B_{n+1} + \beta_n + \gamma_n) u_n + \gamma_n v_n \,, \\ \ddot{v}_n &= \gamma_n (u_n - v_n) \,, \end{aligned} \tag{5.17}$$

where

$$B_n = \frac{3}{2} \alpha_n \delta_n^{1/2} \,. \tag{5.18}$$

By considering (without loss of generality at the level of this linear approximation) a complex representation of the wavefunctions, $u_n = \phi_n e^{i\omega t}$ and $v_n = \psi_n e^{i\omega t}$, and defining $E = -\omega^2$, we obtain

$$\begin{aligned} E\phi_n &= B_n \phi_{n-1} + B_{n+1} \phi_{n+1} - (B_n + B_{n+1} + \beta_n + \gamma_n) \phi_n + \gamma_n \psi_n \,, \\ E\psi_n &= \gamma_n (\phi_n - \psi_n) \,, \end{aligned} \tag{5.19}$$

an eigenvalue problem that we can solve numerically by diagonalization. Using this linear description, we can now address the issue of a localization ("metal–insulator") transition for suitable incommensurate periodic coefficient variations of different types.

5.4.1 Linear spectrum and localization transition

In addition to the linear spectrum, which we obtain by solving (5.19), we also compute the inverse participation ratio (IPR), as in Chapter 4. For this we use

$$P^{-1} = \frac{\sum_n \left[h(u_n, \dot{u}_n)^2 + h(v_n, \dot{v}_n)^2 \right]}{\left[\sum_n h(u_n, \dot{u}_n) + h(v_n, \dot{v}_n) \right]^2} \in [0, 1] \tag{5.20}$$

as a measure of the amount of localization of the eigenmodes. For modal analysis, we use $h(u_n, \dot{u}_n) = u_n^2$ and $h(v_n, \dot{v}_n) = v_n^2$. As a reminder, a value of $P^{-1} = 1$ accounts for modes when only one particle is vibrating. In contrast, a mode is fully extended if $P^{-1} \to 0$ as $N \to \infty$. This provides a qualitative understanding

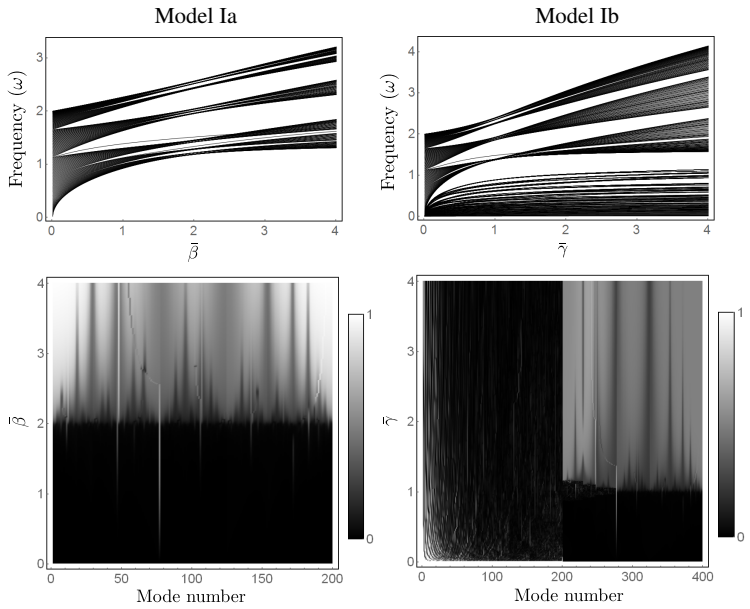


Figure 5.3: (Top) Linear spectrum as a function of the quasiperiodicity parameter and (bottom) inverse participation ratio. We show our results for model Ia in the left column and for model Ib in the right column.

of the nature of the linear modes, and a transition in the IPR also gives a way to quantitatively describe the AA transition.

In Fig. 5.3, we show the linear spectrum and IPR as a function of the quasiperiodicity parameter (which is $\bar{\beta}$ in model Ia and $\bar{\gamma}$ in model Ib) for a chain of $N = 200$ particles for models Ia and Ib. We observe that these two models have a complex structure of bands and gaps, with some frequencies that appear isolated in the gaps and others that form bands that appear to cluster. Isolated frequencies are associated with modes that are similar to impurity modes. Similar structures of bands and gaps have been observed in other physical systems, such as in optics (see, e.g., [85, 108]). Interestingly, we observe from the IPR that AA transitions occur in granular chains, most prominently in model Ia, where the transition is effectively identical to that in the original AA model. This is a consequence of modulating only the on-site potential with an external mechanism, so linearizations of the two systems yield the same equations. If $B_n = 1$ and $\gamma_n = 0$ for all n, the transition occurs at $\bar{\beta} = 2$. This differs from

the localization properties of the linear modes in the Anderson model, where low-frequency linear modes remain extended independently of the amount of disorder [107]. In Fig. 5.4(a), we show the transition to localization in the fundamental mode of model Ia. For model Ib, we double the number of modes in the system, because we double the number of DOF by incorporating the internal particles. This system has a very rich spectrum, where the upper part (half of the modes) has the same structure as in model Ia, but there is also a bottom part (the other half of the modes) associated with modes that do not undergo the localization transition and consequently are extended independently of the modulation. This is straightforward to explain by writing the system (5.17) in terms of in-phase ($x_n = u_n + v_n$) and out-of-phase ($y_n = u_n - v_n$) variables. This yields $\dot{x}_n = f(x_n, x_{n\pm1}, y_n, y_{n\pm1})$ and $\dot{y}_n = g(x_n, x_{n\pm1}, y_n, y_{n\pm1}) - 2\gamma_n y_n$. Only the equations for $\dot{y}_n$ are affected explicitly by the quasiperiodicity. In this case, $2\gamma_n$ enters as a prefactor of y_n, instead of γ_n as in model Ia. This explains why the localization transition occurs at $\bar{\gamma} = 1$ instead of at $\bar{\gamma} = 2$. Note that modes in the upper part of the spectrum also correspond to out-of-phase modes (between u_n and v_n), whereas the bottom part of the spectrum is associated with in-phase modes. The latter do not see the quasiperiodicity in practice (because they effectively satisfy the original Hertzian dynamics without the MiM contribution), so they are generically extended.

In contrast to models Ia and Ib, model II does not have a localization transition; instead, we observe that all modes are extended, except for the ones that are associated with isolated frequencies in the gaps. In Fig. 5.4(b), we show the IPR as a function of $\bar{\alpha}_2$ for model II with $\bar{\alpha}_1 = 3$. This suggests that, without an on-site potential, one cannot observe this sort of transition in granular chains of cylindrical particles. In the future, it will be particularly worthwhile to explore the generality of this conclusion. Specifically, a relevant question is whether it is generically the case that it is impossible for inter-site interactions, modulated by one or more frequencies, to induce a localization transition in a granular chain.

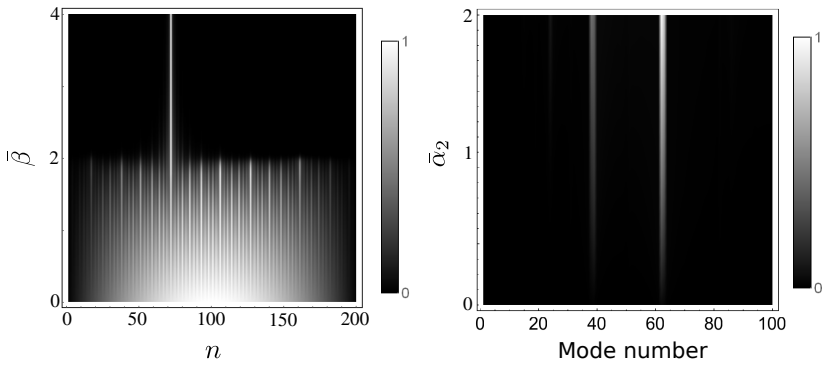


Figure 5.4: (Left) Localization transition as a function of $\bar{\beta}$ for the fundamental mode in model Ia. (Right) Inverse participation ratio P^{-1} as a function of $\bar{\alpha}_2 \in [0, 2]$ and $\bar{\alpha}_1 = 3$ for model II with $N = 100$ cylindrical particles.

5.5 Hofstadter butterfly

Another property of the AA model's spectrum is its fractal nature. To explore this, we compute the spectrum as a function of ξ (see Fig. 5.5), and we observe a structure that is known as a *Hofstadter butterfly*. The butterfly is a footprint of the spectrum's fractality, and one can see its statistical self-similarity in the figure.

The Hofstadter butterfly was first predicted in 1976 [54] in a completely different system: Bloch electrons on 2D lattices and in the presence of an orthogonal magnetic fields. In typical crystals, one needs to use magnetic fields that are at least of the order of several thousands of tesla to observe a Hofstadter butterfly. As a result, it took until 1997 — in a microwave system [83] — that a Hofstadter butterfly was observed experimentally. A Hofstadter butterfly was then observed in graphene in 2013 [28] and using interacting photons in superconducting qubits in 2017 [137]. The possibility to also observe Hofstadter butterflies in granular chains is very exciting, given the simplicity and controllability of the latter system.

To characterize the self-similarity of the spectrum in the different cases, we compute the Minkowski–Bouligand fractal dimension (D_m), which (by Moran's theorem) is the same as the Hausdorff dimension (D_h) for strictly self-similar

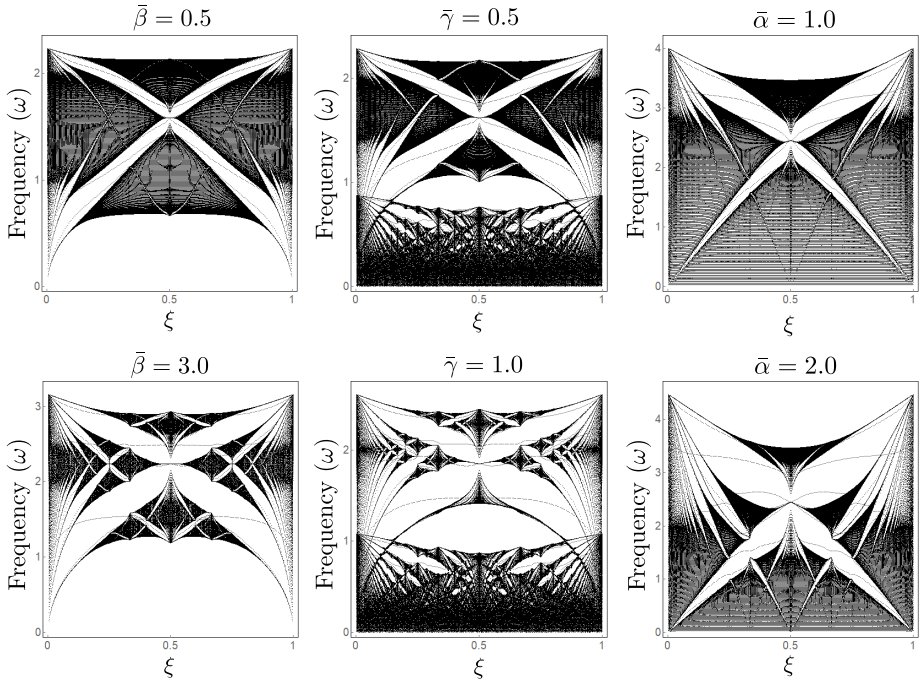


Figure 5.5: Linear spectrum, in the form of a Hofstadter butterfly, as a function of ξ for (left) model Ia, (center) model Ib, and (right) model II.

fractals [35, 140]. The procedure to numerically compute D_M is known as *box-counting*, and we proceed as follows. First, we map the Hofstadter spectrum into a square of 480×480 pixels, we then partition the square into boxes of characteristic size (side length) l_B, and finally we count the number N_B of boxes that include at least one point of the spectrum. We do this procedure for different values of l_B; if $\ln(N_B)$ scales linearly with $\ln(l_B)$, then the fractal dimension D_M satisfies the relation $N_B \propto l_B^{-D_M}$. In practice, one computes D_M as the best fit to $N_B \propto l_B^{-D_M}$. For this, we compute a linear regression of the logarithm of the data using gradient descent. In Fig. 5.6(a), we show an example of the box counting for the Hofstadter spectrum of model Ia at the localization transition (i.e., when $\bar{\beta} = 2$). To show how the band gaps are filled with boxes, we have superimposed the N_B boxes over the spectrum for different values of l_B.

We now compute the fractal dimension D_M as a function of the quasiperiodic parameters $\bar{\alpha}_2$, $\bar{\beta}$, and $\bar{\gamma}$ for our three models. We expect D_M to be between 1

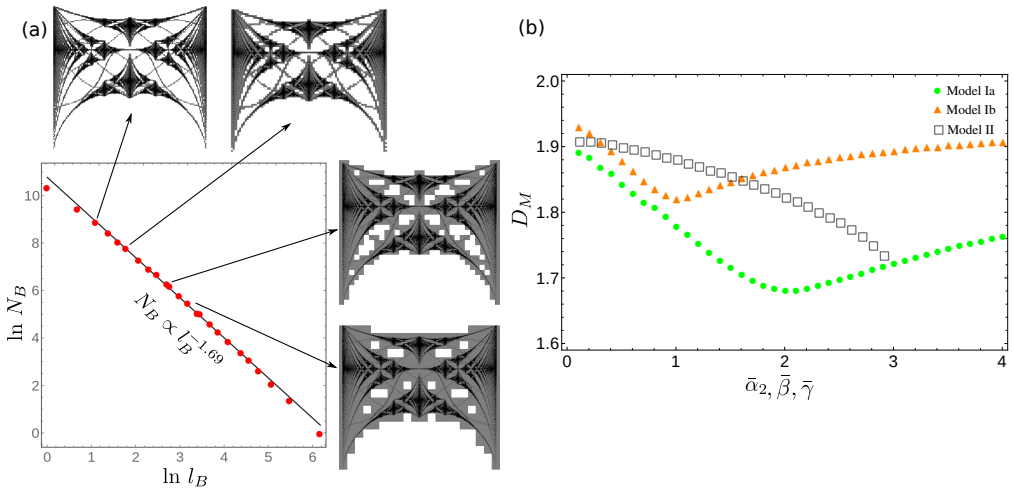


Figure 5.6: (a) Example of the box-counting process that we use to compute the fractal dimension for model Ia and $\bar{\beta} = 2$. (b) Minkowski–Bouligand fractal dimension D_M as a function of the quasiperiodic parameter $\bar{\beta}$, $\bar{\gamma}$, and $\bar{\alpha}_2$ for models Ia, Ib, and II, respectively. We use the parameter value $\bar{\alpha}_1 = 3$ for model II.

and 2, because $D_M = 1$ for a line and $D_M = 2$ for a plane. In Fig. 5.6(b), we show the results of our computations. We observe that the minimum fractal dimension occurs at the same point as the localization transition for models Ia (at $\bar{\beta} = 2$) and Ib (at $\bar{\gamma} = 1$). We calculate that $D_M \gtrapprox 1.69$ for model Ia and $D_M \gtrapprox 1.82$ for model Ib. It is interesting to note the similar non-monotonic dependence of the fractal dimension on the model parameters in models Ia and Ib. Presumably, this arises from the aforementioned similarity of the former model and the out-of-phase excitations of the latter model. In contrast, in model II, for $\bar{\alpha}_1 = 3$ and $\bar{\alpha}_2 \in (0, 3)$, we observe that the fractal dimension decreases monotonically as $\bar{\alpha}_2$ increases.

5.5.1 Recovering a Hofstadter butterfly from dynamics

We are interested in reconstructing the Hofstadter spectrum from the dynamics of our systems. We are inspired by recent results in interacting photons [137], where a technique based on a spectroscopic method and a Fourier transform was used to resolve the energy levels of a (few degrees-of-freedom) Bose–Hubbard

system. In our case, rather than focusing on resolving each energy level — which one can do in principle by following the procedure from [137] — we visualize the main band-gap structure of the Hofstadter spectrum. To do this, we apply a periodic driving at one of the boundaries of a granular chain at rest and at various frequencies between the upper and lower band edges. We then measure the energy that is absorbed by the chain after a certain time due to resonances between the excited frequencies and the chain's eigenmodes.

To illustrate our approach, we apply it to model II for a chain with $N = 21$ particles. The external driving is reflected in the first particle's equation of motion as

$$\ddot{u}_1 = \alpha_1[\delta_1 + \epsilon \sin(2\pi\nu t) - u_1]_+^{3/2} - \alpha_2[\delta_2 + u_1 - u_2]_+^{3/2}, \tag{5.21}$$

where we set $F_0 = 100$ and $\epsilon = 0.01$ in our numerical computations. We also set $u_{N+1} = 0$ for all t in Eq. (5.6), so we have a fixed boundary condition there.

We need to compute the total energy of the system. To do this, we write the particles' energy as

$$H_n = \frac{\dot{u}_n^2}{2} + \frac{\dot{v}_n^2}{2} + \frac{1}{2}\left\{\frac{2\alpha_n}{5}\left[\delta_n + u_{n-1} - u_n\right]_+^{5/2} + \frac{2\alpha_{n+1}}{5}\left[\delta_{n+1} + u_n - u_{n+1}\right]_+^{5/2}\right\} \tag{5.22}$$
$$+ \frac{\beta_n}{2}u_n^2 + \frac{\gamma_n}{2}\left(u_n - v_n\right)^2 .$$

The total energy is $H = \sum_n H_n$, which is a conserved quantity in the absence of external driving. Note that in the context of experiments, one should also consider dissipation which is neglected here; see a relevant summary of models thereof in [20]. Importantly, we expect that our results will be robust enough to be observable experimentally even in the presence of a small amount of dissipation. This claim is supported by recent experimental results on the observation of other linear phenomena [78] in granular chains.

The system starts at rest at $t = 0$, so $H(0) = \sum_n \frac{2\alpha_n}{5}\delta_n^{5/2}$ is the constant background energy associated with the precompression. Moreover, for $t > 0$, we have $H(t) \geq H(0)$, in the presence of the drive. Let $\Delta H(T) = H(T) -$

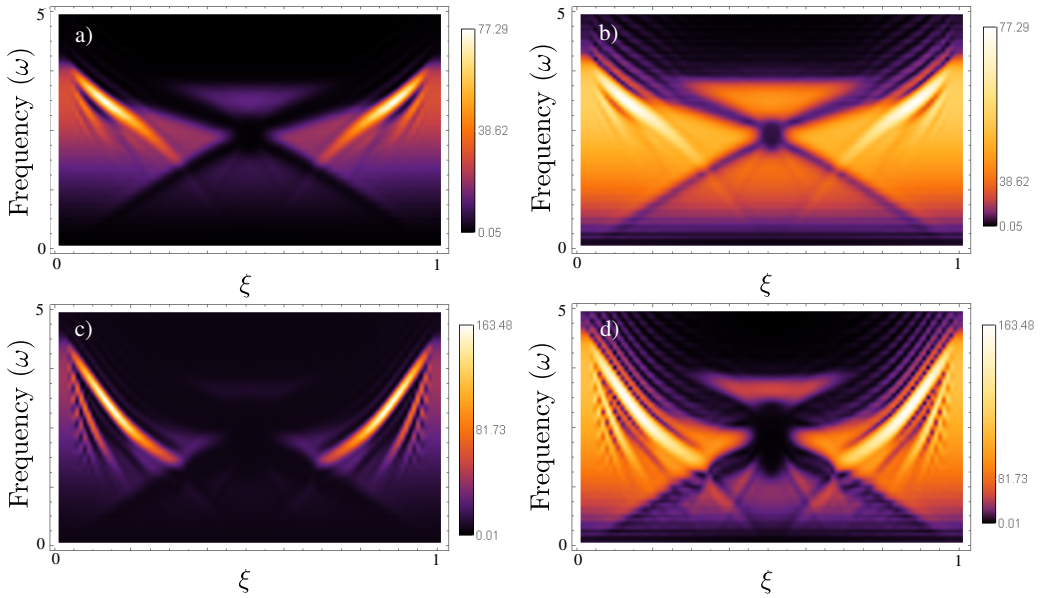


Figure 5.7: Energy absorbed in model II for (top) $\bar{\alpha}_2 = 1$ and (bottom) $\bar{\alpha}_2 = 2$ (bottom panels). We use the parameter value $\bar{\alpha}_1 = 3$ in all cases. We show the absorbed energy on a linear scale in the left panels and on a logarithmic scale in the right panels. High intensity corresponds to large absorbed energy and hence frequencies in the pass band of the system, while low intensity, respectively, corresponds to frequencies in the band gaps of the system.

$H(0) \geq 0$ denote the energy that is absorbed by the system at time $t = T$. To integrate (5.6) and (5.21), we use a fifth-order explicit Runge–Kutta (RK5) method with a step size of $\mathrm{d}t = 0.01$ and $T = 20$. Note that in this Chapter we have used non-dimensional units. In Fig. 5.7, we show the absorbed energy patterns for two sets of parameters: (i) $\bar{\alpha}_1 = 3$ and $\bar{\alpha}_2 = 1$ and (ii) $\bar{\alpha}_1 = 3$ and $\bar{\alpha}_2 = 2$. By comparing these patterns with Figs. 5.5, we see that the method performs very well towards capturing the main band-gap structure, and we are even able to successfully capture some fine structure (i.e., some minor gaps), which we can observe especially when we plot the logarithm of the absorbed energy.

5.6 Energy transport and localization

Another important issue, which one can examine in several ways, is how energy transport is affected by the quasiperiodicity [81, 90]. For instance, one can compute a second moment m_2 of the energy distribution as a function of time to quantitatively characterize the temporal evolution of the energy distribution's width [2, 27, 42, 89, 96, 107, 120, 136], as we showed in Chapter 4. Following recent studies in disordered granular chains [78], we study the evolution of the energy distribution $\{H_n\}_{n=1}^{N}$ immediately after the impact of a striker against the first particle ($n = 1$).

Following the same procedure as in Chapter 4, we compute the second moment

$$m_2(t) = \frac{\sum_n (n-1)^2 H_n}{\sum_n H_n}\,, \tag{5.23}$$

and we estimate a scaling relationship between m_2 and t. When the scaling is approximated reasonably as a power law — for which, in exact form, $m_2(t) \sim t^{\eta}$ as $t \to \infty$ for some exponent η. In a perfectly homogeneous granular chain, it is known that energy transport is ballistic. However, when disorder is added to the chain, the dynamics can change drastically, and one can observe different energy transport regimes [2, 107]. These previous studies have focused on the interplay between disorder and nonlinearity. Here, in contrast, we show that even in a strongly precompressed (i.e., almost linear) chain, one can obtain any desired exponent diffusion $\eta \in [0, 2]$ for the energy transport. However, we find that on-site potentials are essential to have localization.

One advantage of working with quasiperiodic chains instead of disordered ones is that we do not need to compute averages over a large number of realizations to obtain robust insights. Our quasiperiodic chains are produced in a deterministic way, so given a parameter ξ, one gets one specific chain. This enables us to cover the whole parameter space with considerably fewer computations than when studying disordered chains. We are also interested in characterizing energy transport in realistic frameworks, so we set $N = 21$, which gives a long

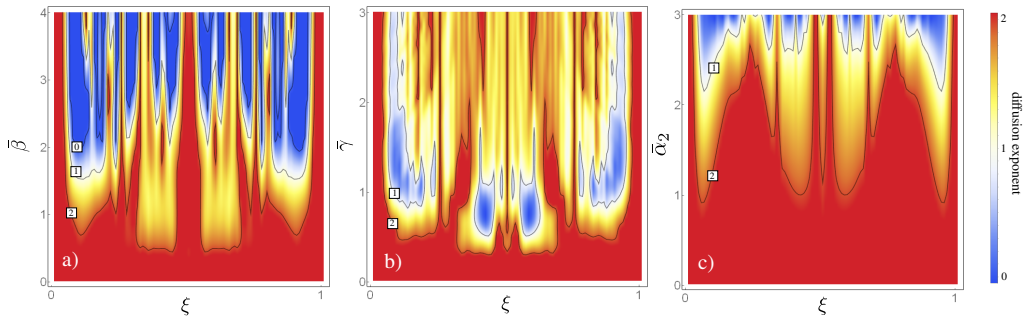


Figure 5.8: Diffusion exponent γ for (a) model Ia, (b) model Ib, and (c) model II as a function of the quasiperiodic parameters and ξ.

enough chain to qualitatively capture the nature of transport, at least in several recent experimental and theoretical explorations [78, 107].

As in section 5.5.1, we integrate Eq. (5.6) using a RK5 method and we set $u_0(t) = u_{N+1}(t) = 0$ for all t, so we have fixed boundary conditions on both sides. We use the stopping criterion for our simulations that either $T = 20$ or that energy reaches the boundary opposite to the one impacted by the striker. We use the former condition to stop the code in cases in which all of the energy is trapped in the form of localized states. In other words, there is no diffusion. This is expected, for instance, in model Ia for $\bar{\beta} > 2$ (i.e., after the localization transition occurs). However, it is an uncommon scenario in model II, which does not have a localization transition. In Fig. 5.8, we show our results for energy transport in our three models. In models Ia and Ib, we explore the parameters ranges $\bar{\beta} \in [0, 4]$ and $\bar{\gamma} \in [0, 3]$, respectively, so we can compare energy transport on both sides of the localization transition. In model II, we consider $\bar{\alpha}_1 = 3$ and $\bar{\alpha}_2 \in [0, 3]$. For all three models, and for $\xi \in [0, 1]$, we can tune the energy transport over from subdiffusive to ballistic behaviors. This allows a great deal of control of the energy-transport properties, and it is remarkable that we are able to do this using a deterministic model. In model Ia, we also observe localization (for which $\eta = 0$) in contrast with observations in disordered granular crystals [78, 107]. This suggests that the inclusion of on-site potentials is crucial for this localization phenomenon.

5.7 Conclusions

In this Chapter, we introduced different types of quasiperiodic granular chains that were inspired by the work by Aubry and André in condensed-matter physics and by recent developments (cradle and mass-in-mass systems) in the context of granular lattice systems. We studied the localization and spectral properties of such chains. To achieve each type of quasiperiodic chain, we incorporated spatial modulation (which is incommensurate with the chain's period) into one of the physical parameters. We proposed three models: models Ia and Ib use spherical particles, in which quasiperiodicity enters via an on-site potential — either in the form of a local oscillator (as in a cradle) or in the form of a local resonator (for a mass in mass system) — and model II uses cylindrical particles. In models Ia and Ib, we demonstrated the existence of an analog of the well-known AA transition. However, in model II, we showed that, without an on-site potential and with quasiperiodicity affecting only inter-site interactions, a localization transition cannot occur.

We also computed the Hofstadter spectrum for each of the models and studied their fractal properties by computing the Minkowski–Bouligand fractal dimension. In models Ia and Ib, we showed that the minimum fractal dimension D_M of the spectrum coincides with the point at which the localization transition occurs. For model II, we observed that the spectrum's fractal dimension decreases monotonically as a function of the quasiperiodic parameter.

Finally, we numerically studied energy transport by exciting the granular chains with a striker. We demonstrated the existence of different regimes — ranging from ballistic to subdiffusive transport — as well as localization. In contrast to prior work, which achieved such control using a combination of disorder and adjusting the nonlinearity strength [2, 107], we were able to control the energy transport using a deterministic model in a strongly precompressed (and almost linear) granular chain.

Chapter 6

CONCLUSIONS AND FUTURE WORK

In this thesis, we investigate various phenomena that emerge in granular crystals. We began, in Chapter 3, with the study of scattering of low-amplitude mechanical waves in chains with impurities. In this case, we derived an exact mathematical expression for the amplitudes of the transmitted and reflected waves. We showed that under certain conditions a resonance, analogs to the Ramsauer–Townsend (RT) in quantum mechanics, arises that leads to perfect transmission. We discussed the case in which multiples impurities are added to the chain, and showed how the RT resonance is behind the transport of energy at certain frequencies.

In Chapter 4, we have characterized the localization and transport properties of one-dimensional disordered granular crystals for both uncorrelated and correlated disorders. In the linear regime, there are different reflectionless modes that contribute to the energy transport. We investigated the correlation properties of three types of disorder — the Anderson-like model and two random dimer models — and we demonstrated that the rules that generate the RDM2 chain can contain either short-range or long-range correlations in the disorder. Furthermore, we showed that surprising behavior can occur when we introduce disorder into granular chains. As we expected, disorder in combination with significant precompression (i.e., a very low level of nonlinearity) tends to localize

energy due to Anderson localization effects. Unexpectedly, however, localization no longer emerges for sufficiently small precompression, as the energy tends to spread throughout the whole chain. In the sonic-vacuum regime (i.e., no precompression), the exponents of the temporal asymptotic scaling of the inverse participation ratio are close to -1, which is what occurs in the "linear" homogeneous case (in particular, about $F_0 = 10$ N). However, the transport remains superdiffusive rather than ballistic. Such dynamics are completely different from what is known about disorder in other lattice models [38], in which a self-trapping mechanism always dominates above certain amount of nonlinearity, independently of the type of disorder.

In the Anderson-like model, we find a transition from subdiffusive ($\gamma < 1$, high precompression) to superdiffusive ($\gamma > 1$, low precompression) transport that depends on the amount of precompression. For the two types of correlated disorder that we investigate, the transport is always superdiffusive for all amounts of precompression. We conclude that transport dynamics appears to depend more on the correlation properties of disorder than on the specific structure of the spectrum and the eigenfunctions. However, the scaling of the second moment and the inverse participation ratio as a function of time are almost independent of the correlation or the specific properties of the disorder in the highly nonlinear regime.

Our work opens a panorama of both theoretical and experimental research possibilities. From a theoretical perspective, future challenges involve deriving the mechanisms that relate the type of correlation in the chain disorder to the spectral and transport properties of the system, incorporating dissipation effects into disordered granular crystal, and more. Indirect experimental measures of the dynamical properties are possible using experimental techniques such as the ones in Ref. [10], and importantly recent more advanced techniques now allow one to measure the spatiotemporal properties of an entire granular chain, as the ones that are shown in the Appendices B and C of this thesis. This makes it possible to track the force at each particle as a function of time.

In Chapter 5, we study quasiperiodicity-induced localization of waves in strongly precompressed granular chains. We propose three different setups, inspired by the Aubry–André (AA) model, of quasiperiodic chains; and we use these models to compare the effects of on-site and off-site quasiperiodicity in nonlinear lattices. When there is purely on-site quasiperiodicity, which we implement in two different ways, we show for a chain of spherical particles that there is a localization transition (as in the original AA model). However, we observe no localization transition in a chain of cylindrical particles in which we incorporate quasiperiodicity in the distribution of contact angles between adjacent cylinders by making the angle periodicity incommensurate with that of the chain. For each of our three models, we compute the Hofstadter spectrum and the associated Minkowski–Bouligand fractal dimension, and we demonstrate that the fractal dimension decreases as one approaches the localization transition (when it exists). Finally, in a suite of numerical computations, we demonstrate both localization and that there exist regimes of ballistic, superdiffusive, diffusive, and subdiffusive transport. Our models provide a flexible set of systems to study quasiperiodicity-induced analogs of Anderson phenomena in granular chains that one can tune controllably from weakly to strongly nonlinear regimes.

There are several questions that are still open and they require further research. For instance, (a) is the superdiffusive regime reached by the three disordered models at $F_0 = 0$ universal? i.e., independent on the type of disorder, the correlation, initial condition, etc. Our results suggest some sort of universality, however a further development in the theory and more simulations are require to state this; (b) how is the energy transport in higher dimension (2D and 3D)?; (c) what are the dynamical properties, such as energy transport and energy localization, in quasiperiodic systems?

In the context of quasiperiodic granular crystals, naturally, it will be particularly valuable to implement some of these ideas in laboratory experiments, as one can then further explore the role that granular systems can play in the study of quasiperiodic operators [83, 28, 137]. Achieving an experimental realization of

a Hofstadter butterfly in a granular chain would also be very exciting in its own right. Among the settings that we have proposed in this dissertation, model Ib (i.e., the chain of mass-in-mass particles) is the clearest candidate for observing a localization transition (in the out-of-phase variables), given that the cradle system has yet to be experimentally realized. Arguably, the woodpile setup of [77] may also constitute an excellent playground for such studies. However, a key consideration, given experimental limitations, is that one seeks to build a chain with as few particles as possible such that one can (still) observe the relevant phenomenology. There are also numerous open issues to explore computationally and theoretically. Examples include the effect of nonlinearity (e.g., through larger excitation amplitudes) on these modes and their localization, how these phenomena differ for granular crystals in different numbers of dimensions, and others. Relevant extensions will be considered in future studies.

Appendix A

SYMPLECTIC NUMERICAL INTEGRATION SCHEME

In ideal conditions, granular crystals are considered Hamiltonian, i.e., the dynamics conserves the total energy. So, it is fundamental for us to accurately control the energy of the system during numerical integration. This is specially important in Chapter 4, where we are interested in characterizing the long-time behavior of the energy distribution in large systems. In Ref. [91], Laskar and Robutel introduced a class of symplectic integrators that are adapted to integrate a perturbed Hamiltonian system of the form[1] $H = A + \epsilon B$, where $|\epsilon| \leq 1$. They start from the Hamiltonian $H(\mathbf{q}, \mathbf{p})$, which leads to the Hamilton equations

$$\frac{dp_j}{dt} = -\frac{\partial H}{\partial q_j}\,, \tag{A.1}$$

$$\frac{dq_j}{dt} = \frac{\partial H}{\partial p_j}\,, \tag{A.2}$$

where $j \in \{1, \ldots, N\}$ indexes the degrees of freedom in the Hamiltonian. Writing $\mathbf{x} = (\mathbf{q}, \mathbf{p})$ yields

$$\frac{d\mathbf{x}}{dt} = \{H, \mathbf{x}\} = L_H \mathbf{x}\,, \tag{A.3}$$

where $\{\cdot, \cdot\}$ denotes the Poisson bracket

$$\{f, g\} = \sum_j \left(\frac{\partial f}{\partial p_j}\frac{\partial g}{\partial q_j} - \frac{\partial f}{\partial q_j}\frac{\partial g}{\partial p_j} \right)\,. \tag{A.4}$$

[1]For granular crystals $\epsilon = 1$. That is, the "perturbation" is of a comparable size to the unperturbed Hamiltonian. In this case, A is the kinetic energy and B the potential energy.

The differential operator L_H is defined by $L_\chi f = \{\chi, f\}$, and the solution $\mathbf{x}(t)$ of Eq. (A.3) with $\mathbf{x}(0) = \mathbf{x}_0$ is

$$\mathbf{x}(t) = \left(\sum_{n \geq 0} \frac{L_H^n}{n!} t^n \right) \mathbf{x}_0 = e^{tL_H} \mathbf{x}_0 \,. \tag{A.5}$$

The main idea of the symplectic integration method in [91] is to find a K that approximates the Hamiltonian H with an error that scales as some power of the temporal step size τ. Laskar and Robutel developed a scheme, called "SABA$_2$" that approximates the Hamiltonian as $K = H + \tau^2 k\{\{A, B\}, B\} + O\left(\tau^4\right)$. The SABA$_2$ method uses the following approximation:

$$\Theta = e^{c_1 \tau L_A} e^{d_1 \tau L_{\epsilon B}} e^{c_2 \tau L_A} e^{d_1 \tau L_{\epsilon B}} e^{c_1 \tau L_A} \approx e^{tL_H} \,, \tag{A.6}$$

where $c_1 = \frac{1}{2}\left(1 - \frac{1}{\sqrt{3}}\right)$, $c_2 = \frac{1}{\sqrt{3}}$, and $d_1 = \frac{1}{2}$. Thus, $\mathbf{x}(t) \approx \Theta\, \mathbf{x}_0$.

One can improve the accuracy of the SABA$_2$ when the term $C = \{\{A, B\}, B\}$ leads to an integrable system — i.e. when $\frac{d\mathbf{x}}{dt} = L_C \mathbf{x}$ is integrable — as in the common situation of A being quadratic in momentum $\mathbf{p}$ and B depending only on the displacement $\mathbf{q}$, which is what happens in granular crystals. In this case, one includes two corrector terms that consist of small backward steps to obtain

$$\Theta_{\mathrm{C}} = e^{-(\tau g/2) L_C} \Theta\, e^{-(\tau g/2) L_C} \,, \tag{A.7}$$

where we choose $g = (2 - \sqrt{3})/24$ to eliminate the τ^2 dependence in the remainder, which now becomes of order $O\left(\tau^4\right)$. This scheme is called SABA$_2$C.

It is known that SABA$_2$C is extremely effective for problems that involve both disorder and nonlinearity in Hamiltonian lattices [119]. In particular, Skokos et al. [144, 145] implemented SABA$_2$, and some variations of it, for both nonlinear Schrödinger and Klein–Gordon lattices, and they showed that there is a considerable improvement in the energy conservation in comparison with classic Runge–Kutta schemes of integration.

In our case, we have a Hamiltonian of the form

$$H(\mathbf{q}, \mathbf{p}) = A(p) + B(q) \,, \tag{A.8}$$

where $A(\mathbf{p}) = \sum_n p_n^2/2$, and $B(\mathbf{q}) = \sum_n B_n(\mathbf{q})$. Therefore,

$$\begin{aligned}
\frac{dp_j}{dt} &= -\frac{\partial H}{\partial q_j} = -\frac{\partial B}{\partial q_j} = F_j\,, \\
\frac{dq_j}{dt} &= \frac{\partial H}{\partial p_j} = \frac{\partial A}{\partial p_j} = p_j\,, \\
\frac{\partial A}{\partial q_j} &= 0\,, \\
\frac{\partial B}{\partial p_j} &= 0\,.
\end{aligned}$$

The time derivative of the equation for $\dot{q}_j$ yields

$$\ddot{q}_j = F_j\,. \tag{A.9}$$

We calculate an explicit expression for

$$\begin{aligned}
C &= \{\{A, B\}, B\} \\
&= \sum_n \frac{\partial\{A, B\}}{\partial p_n}\frac{\partial B}{\partial q_n} \\
&= \sum_{n,n'} \frac{\partial^2 A}{\partial p_n \partial p_{n'}}\frac{\partial B}{\partial q_n}\frac{\partial B}{\partial q_{n'}},.
\end{aligned}$$

Because $\partial_{p_n p_{n'}} A = \delta_{n,n'}$, we obtain

$$C = \sum_n \left(\frac{\partial B}{\partial q_n}\right)^2 = \sum_n F_n^2\,. \tag{A.10}$$

When applying the SABA$_2$C method, we need to calculate terms like $e^{\alpha\tau L_A}\mathbf{x}$, $e^{\beta\tau L_B}\mathbf{x}$, and $e^{\gamma\tau L_C}\mathbf{x}$. These terms, respectively, give the evolution of $\mathbf{x}$ under the Hamiltonians A, B, and C.

The evolution under A is

$$\frac{d\mathbf{x}}{dt} = \{A, \mathbf{x}\}. \tag{A.11}$$

Therefore,

$$\begin{aligned}
\frac{dp_j}{dt} &= 0\,, \\
\frac{dq_j}{dt} &= p_j(t)\,,
\end{aligned}$$

which yields

$$p_j(t+\alpha\tau) = p_j(t)\,, \tag{A.12}$$

$$q_j(t+\alpha\tau) = q_j(t) + p_j(t)\alpha\tau + O\left(\alpha^2\tau^2\right)\,. \tag{A.13}$$

The evolution under B is

$$\frac{d\mathbf{x}}{dt} = \{B, \mathbf{x}\}, \tag{A.14}$$

which yields

$$\frac{dp_j}{dt} = -\frac{\partial B}{\partial q_j} = F_j\,,$$
$$\frac{dq_j}{dt} = 0\,,$$

which in turn gives

$$p_j(t+\beta\tau) = p_j(t) + F_j(t)\beta\tau + O\left(\beta^2\tau^2\right)\,, \tag{A.15}$$

$$q_j(t+\beta\tau) = q_j(t)\,. \tag{A.16}$$

The evolution under C is

$$\frac{d\mathbf{x}}{dt} = \{C, \mathbf{x}\}\,, \tag{A.17}$$

which yields

$$\frac{dp_j}{dt} = -\frac{\partial C}{\partial q_j} = -2\sum_n F_n \frac{\partial F_n}{\partial q_j} = G_j\,,$$
$$\frac{dq_j}{dt} = 0,$$

which in turn gives

$$p_j(t+\gamma\tau) = p_j(t) + G_j(t)\gamma\tau + O\left(\gamma^2\tau^2\right)\,, \tag{A.18}$$

$$q_j(t+\gamma\tau) = q_j(t)\,. \tag{A.19}$$

A.1 Comparison between SABA$_2$C and a fourth-order Runge-Kutta

In this section we compare our SABA$_2$C algorithm with a fourth-order Runge-Kutta method (RK4), which is the most classical method of the Runge-Kutta family [133]. To summarize the RK4 algorithm, we re-write Eq. (A.3) as

$$\frac{d\mathbf{x}}{dt} = \mathbf{H}(\mathbf{x})\,. \tag{A.20}$$

The integration of the system from time t to time $t+\tau$ requires four evaluations of the function $\mathbf{H}$:

$$\begin{aligned}
\mathbf{k}_1 &= \tau\mathbf{H}\left(t, \mathbf{x}(t)\right)\,, \\
\mathbf{k}_2 &= \tau\mathbf{H}\left(t+\frac{\tau}{2}, \mathbf{x}(t)+\frac{\mathbf{k}_1}{2}\right)\,, \\
\mathbf{k}_3 &= \tau\mathbf{H}\left(t+\frac{\tau}{2}, \mathbf{x}(t)+\frac{\mathbf{k}_2}{2}\right)\,, \\
\mathbf{k}_4 &= \tau\mathbf{H}\left(t+\tau, \mathbf{x}(t)+\mathbf{k}_3\right)\,.
\end{aligned}$$

Then, a RK4 iteration is given by

$$\mathbf{x}(t+\tau) = \mathbf{x}(t) + \frac{1}{6}\left(\mathbf{k}_1 + 2\mathbf{k}_2 + 2\mathbf{k}_3 + \mathbf{k}_4\right)\,, \tag{A.21}$$

therefore, the local truncation error is on the order of $O\left(\tau^5\right)$.

To compare both methods we design a set of simulations of an Anderson system with a displacement initial condition, as in 4.4.3.1, for different chain's lengths. Our first experiment consists in comparing computation time for different time steps, different chain's lengths, and integrating between $t = 0$ s and $t = 10^{-2}$ s for 100 realizations. Averaged computation times are presented in Fig. A.1. We can see that SABA$_2$C consistently outperform RK4 when being compared for the same time step. This is drastic for chains with $N = 10^6$ particles and $dt = 10^{-7}$ s, where RK4 takes over 2.7 hours to complete one realization, whilst SABA$_2$C does the job in under an hour.

Our second experiment consists in measuring the total energy. A proper numerical integrator should conserve the total energy, as it is a conserved quantity of Eq. (2.1). However, RK4 is known to be a dissipative integrator, thus we expect it to behave acceptably only for small enough values of dt. On the other hand, SABA_2C was designed to conserve some approximated version of the Hamiltonian associated with Eq. (2.1). We integrate again a Anderson system with a displacement initial condition and $N = 10^6$ particles, however in this case we do not compute any statistic, because we are interested on energy conservation over a single simulation. Results are shown in Fig. A.2. As expected, for the SABA_2C the energy remains stable, with small oscillation around a constant value. However, the dissipative nature of RK4 is manifested quickly for $dt = 10^{-6}$ s and $dt = 10^{-5}$ s. Only for $dt = 10^{-7}$ s, the energy stays within acceptable values.

Note that all computations were ran in a single processor i7 7700 with 16 Gb of RAM memory.

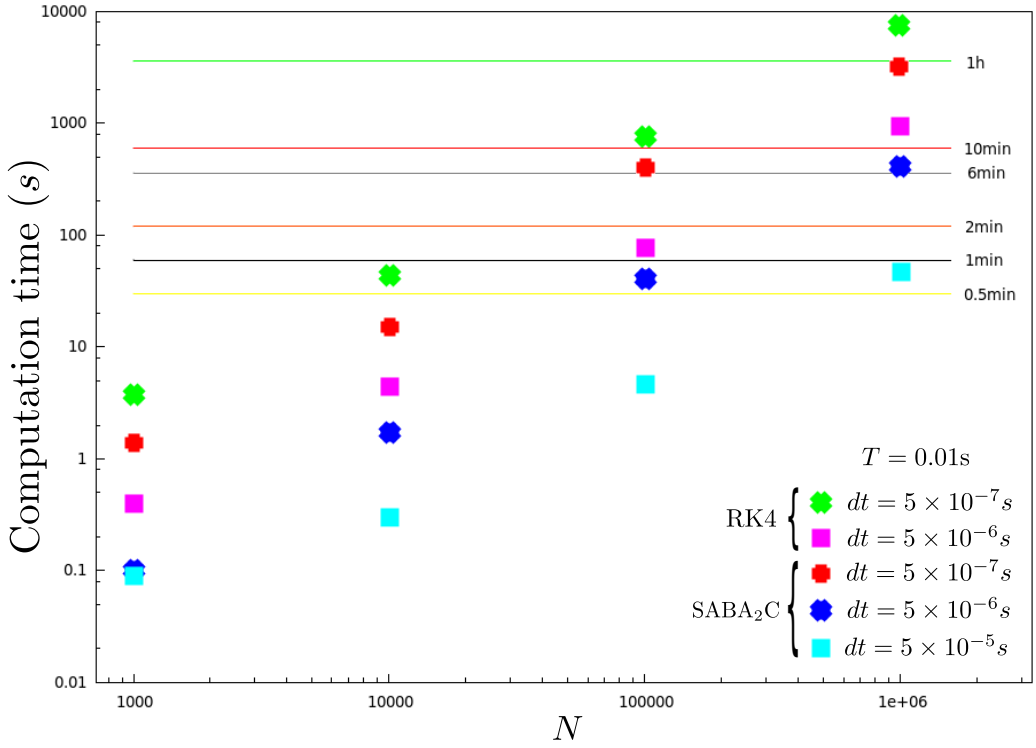


Figure A.1: Average computation time over 100 realizations for a displacement initial condition in granular crystals with Anderson-like disorder.

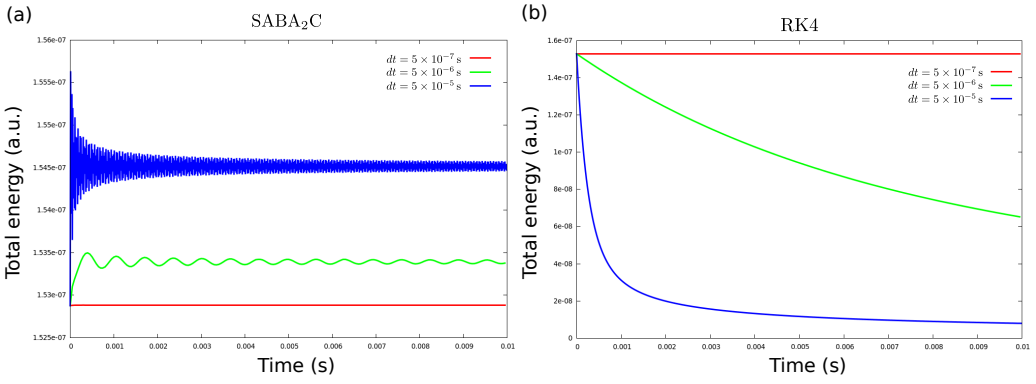


Figure A.2: Total energy as a function of time for (a) $SABA_2C$ and (b) RK4.

Appendix B

RAMSAUER–TOWNSEND EFFECT: EXPERIMENTS ON GRANULAR CRYSTALS

In this Appendix, as well as in appendix C, experimental results obtained at Prof. Jinkyu Yang's laboratory[1] from the William E. Boeing Department of Aeronautics & Astronautics at University of Washington (USA) are presented. My contribution is in terms of modeling, analyzing data, simulating, and the interpretation of experimental data. However, experiments were fully conducted by Prof. Yang's research group. Here, the direct observation of the RT resonance described analytically in Chapter 3 is shown, as well as we compare our results with numerical simulations.

B.1 Numerical simulations

For our numerical computations, we solve Eq. (2.1) directly via a Runge–Kutta method (using the ODE45 function in MATLAB)[2]. Note that, in this section we use a slight different notation regarding the suffixes. We enumerate par-

[1] http://faculty.washington.edu/jkyang/

[2] Note that, a Runge–Kutta scheme is good enough for the computations, because neither the integration time nor the length of the chains are long enough to generate any significant error. Also, due to no disorder is considered to analyze the RT effect, no extensive computations are required. In these sense, these configurations are considerably different from the ones studied in Chapter 4.

ticles from $-N$ to N, instead of from 1 to N. To quantify the transmission efficiency of the impurity-bearing chains, we analyze velocity profiles of propagating waves under harmonic excitations, i.e. we set the boundary conditions as $u_{-(N+1)} = d\sin(2\pi ft)$ and $u_{N+1} = 0$, with d the amplitude and f the frequency. In Fig. B.1(a), we show a space-time contour plot of particle velocities from numerical simulations. In this case, we consider a double impurity (with $\alpha = 1.5$) embedded between particles -2 and $+1$ [see Fig. 3.1(b)] of a chain with 63 particles.

The sinusoidal perturbation that we apply to the left end of the chain has a frequency of 4 kHz and an amplitude of 0.35 N. Given this setup, we compute the magnitude of the particles' maximum displacements to be less than 4.59×10^{-8} m. The associated oscillations are two orders of magnitude smaller than the static precompression $\Delta_n \approx 1.02 \times 10^{-6}$ from $F_0 = 10$ N, so it is reasonable to assume that the system is operating in a nearly linear regime.

To quantify transmission efficiency, we measure the velocity profiles at specific particles: $n = -27$ for incident waves and $n = +3$ for transmitted waves. We choose these particle locations to allow a sufficiently long spatial interval between the two nodes in Fig. B.1(a). The two-sided arrows (1) and (2) indicate regions over which the motion is not affected by the presence of reflections by the chain boundaries. In Fig. B.1(b), we show the velocity profiles of particles $n = -27$ (top panel) and $n = +3$ (bottom panel). The arrows (1) and (2) again correspond to the temporal domains without interference from wave reflection.

In the temporal plots of velocity profiles, we denote the maxima by $v_{\max,i}$ and the minima by $v_{\min,i}$, where $i \in \{1, 2, \dots\}$ is the index of the wave peaks in the oscillation. As indicated by the dots in Fig. B.1(b), the values of these peaks are not constant even in the designated region before the arrival of the reflected waves. Therefore, we need to extract the steady-state component from the propagating plane waves. To do this, we calculate the relative error between a pair of adjacent peaks as

$$\text{Error}_i = \frac{v_{\max,i+1} - v_{\max,i}}{v_{\max,i+1}}\,. \tag{B.1}$$

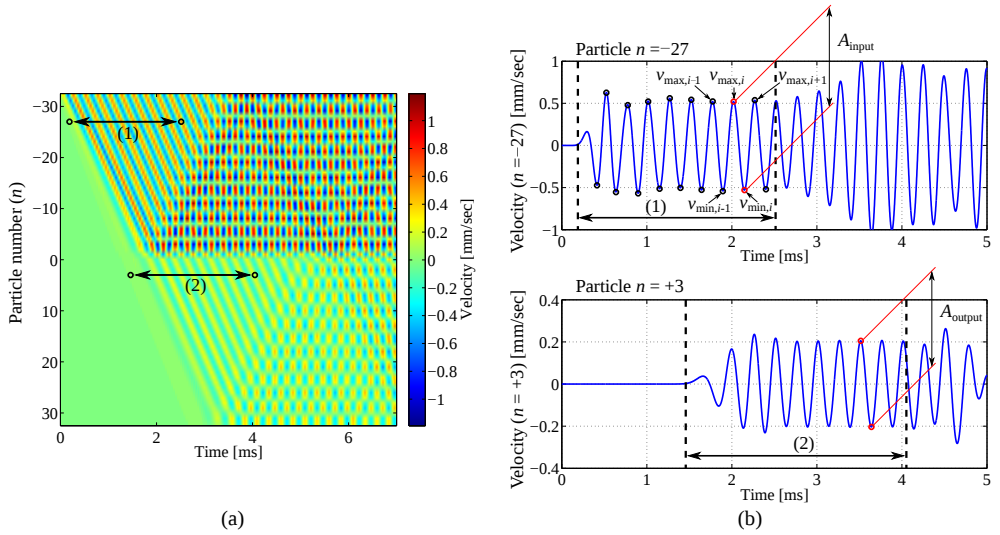


Figure B.1: (a) Space-time contour plot of particle velocity profiles in a host 63-particle chain in which a double impurity has been inserted between particles -2 and $+1$. We use $\alpha = 1.5$ and the parameters in Table B.1 for this numerical simulation. Arrows (1) and (2) indicate the regions that we consider for the calculation of the transmission coefficient. These regions are not affected by the plane waves that reflect from the left or right walls. We also show velocity profiles for particles (b) $n = -27$ and (c) $n = +3$. The dots indicate the maximum and minimum peaks of oscillatory velocity profiles, and the domains of (1) and (2) correspond to the temporal regions marked with (1) and (2) in panel (a).

We identify the steady-state component of the waves by finding a wave packet with a minimal error. The amplitude $\tilde{A}_i$ of the steady-state velocity component is then

$$\tilde{A}_i = v_{\max,i} - v_{\min,i}\,. \tag{B.2}$$

By calculating $\tilde{A}_i$ for each peak i, we measure the incident wave amplitude A_{input} and transmitted wave amplitude A_{output} [see Fig. B.1(b)]. Finally, we quantify the transmission coefficient by calculating the ratio of the transmitted wave's velocity amplitude to that of the incident wave:

$$\bar{T}_{(i),(ii)} = \frac{A_{\text{output};\,(i),(ii)}}{A_{\text{input};\,(i),(ii)}}\,, \tag{B.3}$$

where the subscripts (i) and (ii), respectively, indicate cases with a single impurity and a double impurity. The transmission coefficient $\bar{T}$, which is written in terms of velocity amplitudes, should be equivalent to the displacement ratios introduced in Eq. (3.1) in the ideal situation of harmonic responses of the particles.

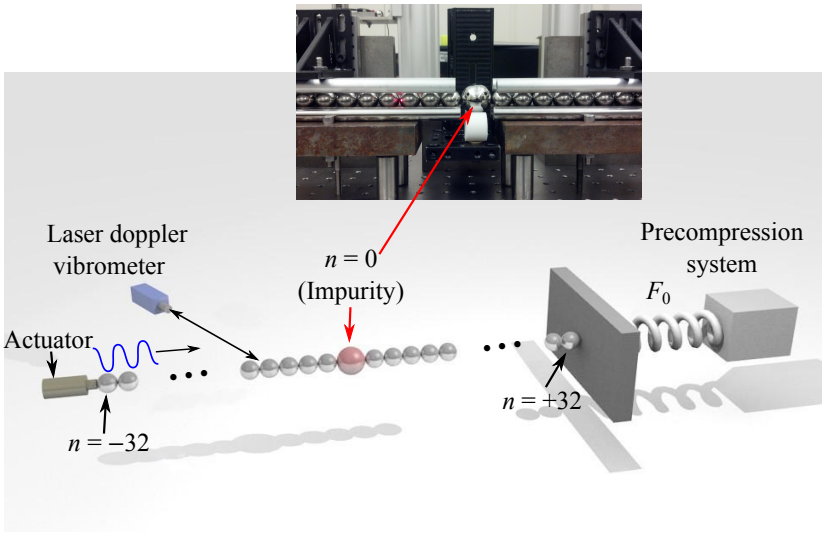


Figure B.2: Schematic of the experimental setup for a granular chain with a single impurity. In the inset, we show an image of the experimental setup.

B.2 Experimental setup and diagnostics

We now discuss the results of experiments in granular chains with a single impurity and a double impurity. In Fig. B.2, we show a schematic to illustrate the experimental setup. A granular chain with 65 spheres is considered: there are 64 type-1 spheres and one impurity in the single-impurity chain, and there are 63 type-1 spheres and 2 impurities in the double-impurity chain. Because of availability limitations, distinct materials are used for type-1 and type-2 particles. However, their material properties are sufficiently similar (see Table B.1) so that it is permissible to treat them as identical materials. As it is shown in the inset of Fig. B.2, one aligns the type-1 particles by using four stainless steel rods, and the impurity particle is held in place by an external holder that ensures that its center is aligned with the other particles in the chain.

To excite the granular chain, one positions a piezoelectric actuator on the left side of the chain in direct contact with particle $n = -32$. To generate plane waves in the granular system, harmonic excitations are used with a frequency ranging from 1.0 to 7.0 kHz with a 200 Hz increment. The right end of the chain is compressed by the wall with a static precompression of F_0 using a spring and linear-stage system. To visualize the propagation of stress waves by measuring the velocity profiles of particles via a non-contact laser Doppler vibrometer (Polytec, OFV-534). See Refs. [100, 19] for the details of this full-field visualization technique.

Similar to our numerical approach, the transmission coefficient is measured by estimating the amplitude of the incident (A_{input}) and transmitted (A_{output}) waves. Unlike our numerical simulations, however, the experimental results are susceptible to noticeable attenuation because of dissipation, friction, and slight particle misalignment. Therefore, experimental results are calibrated by normalizing them with respect to the measurement results obtained from a homogeneous particle chain. The calibrated transmission coefficient is thus

$$\bar{T}^{\text{cal}}_{(i),(ii)} = \frac{\bar{T}_{(i),(ii)}}{\bar{T}_{\alpha=1}} = \frac{A_{\text{output};\,(i),(ii)}}{A_{\text{output};\,\alpha=1}}\,, \tag{B.4}$$

where $\bar{T}_{(i),(ii)}$ is the transmission coefficient for single-impurity and double-impurity chains based on Eq. (B.3), and $\bar{T}_{\alpha=1}$ is the transmission coefficient for a homogeneous chain (i.e., for $\alpha = 1$).

Table B.1: Properties of type-1 and type-2 particles.

	Type-1	Type-2 (impurity)
Material	440C	AISI 52100
Elastic modulus	$E_1 = 204$ GPa	$E_2 = 210$ GPa
Poisson ratio	$\nu_1 = 0.28$	$\nu_2 = 0.30$
Density	$\rho_1 = 7.80$ g/cm^3	$\rho_2 = 7.81$ g/cm^3
Radius	$r_1 = 9.525$ mm	$r_2 = \alpha r_1$

B.3 Comparison between analytical, numerical, and experimental results

We now compare our analytical results with numerical simulations and experimental data for the radius ratios $\alpha = 0.7$ and $\alpha = 1.5$. In Figs. B.3(a,b) are shown the results for the transmission coefficients for a single-impurity chain. Whilst, in Figs. B.3(c,d) the ones for a double-impurity chain. In these plots, black solid curves indicate the analytical predictions from Eqs. (3.3) and (3.4), blue dots indicate the results of simulations obtained by solving Eq. (2.1), and red squares give the experimental results after calibration using Eq. (B.4).

For a single-impurity chain, the transmission coefficient has a decreasing trend as the excitation frequency is increased. This supports our prediction from Fig. 3.2(a). The slope of the decrease depends on the mass ratio. When $\alpha = 0.7$, the decreasing trend starts slow, but there is a rapid drop around the cutoff frequency of 7.25 kHz that we obtained analytically from the formula $\Omega = \sqrt{\frac{4B}{m}}$. For $\alpha = 1.5$, the decrease has a near-linear trend throughout the frequency pass band. In Figs. B.3(a,b), we observe these trends in both numerics and experiments. However, there are some differences in the experiments as compared to the simulations and theoretical predictions.

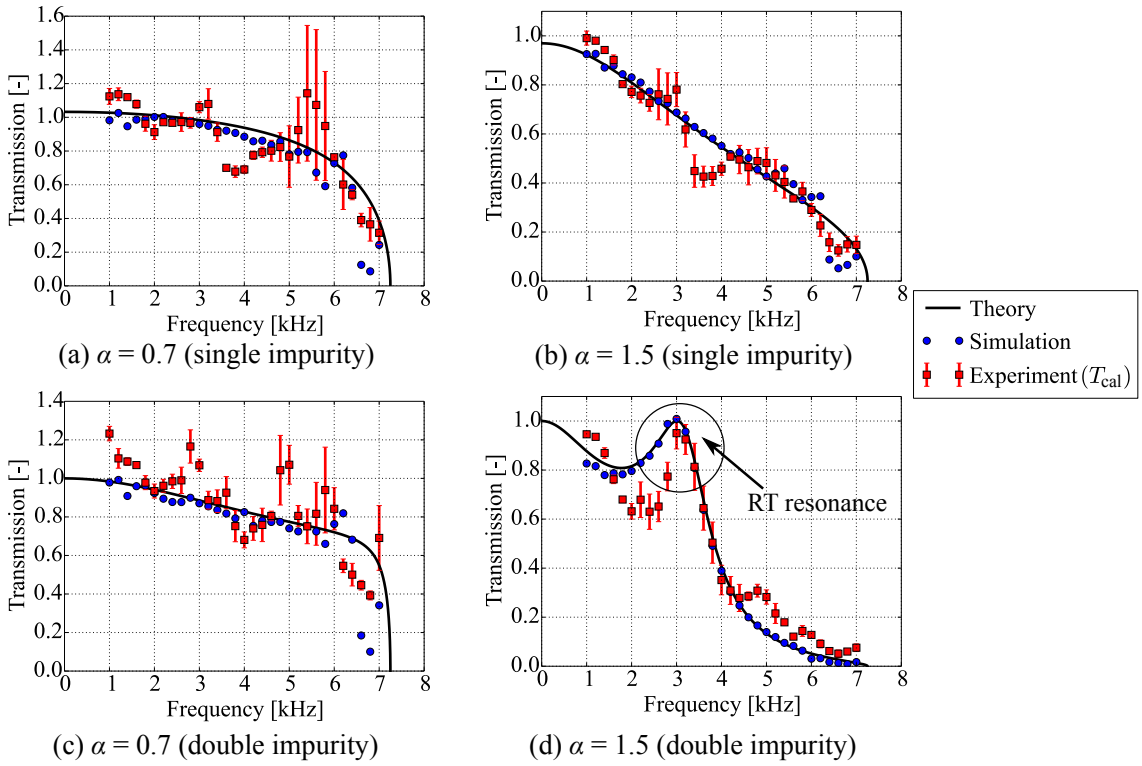


Figure B.3: Transmission of plane waves in a granular chain with impurities. The radius ratio of the impurity radius to the host particle radius in the host chain is (left) $\alpha = 0.7$ and (right) $\alpha = 1.5$. Results for chains with (top) a single impurity and (bottom) a double impurity.

For a double-impurity chain, we obtain more interesting, potentially non-monotonic behavior. When $\alpha = 0.7$, we observe, broadly speaking, a decrease of transmission efficiency as the frequency increases; this is reminiscent of the single-impurity chain. However, for the mass ratio $\alpha = 1.5$, the transmission coefficient has a pronounced double-peak shape in the frequency pass band. In particular, our analytical results for transmission predict a resonant mode at an excitation frequency of about 3.0 kHz. This leads to complete transmission of plane waves despite the existence of impeding double impurities. This mode is notable, and it is observed in both experiments and numerical simulations [see Figs. B.3(c,d)]. However, we again note that quantitative differences exist despite the accurate qualitative description of the experiment and the numerical

corroboration.

As we have just discussed, our analytical predictions match reasonably well with the results of numerical simulations and experimental findings, especially for frequencies between 1.0 and 4.0 kHz. By comparing analytical predictions and experimental results around 3.0 and 4.0 kHz, however, we observe some discrepancies that are not noticeable when comparing analytical and numerical calculations. They probably stem from experimental errors, such as a potential slight misalignment of the external holder and, perhaps more notably, an intrinsic frequency response of a piezo actuator.

For higher frequencies, especially between 6.0 and 7.0 kHz, we observe an especially noticeable discrepancy when comparing the theoretical predictions to the numerical and experimental results. [For example, see Figs. B.3(b,c).] We believe that this arises due to transient waveforms — and specifically due to wave localization — in the vicinity of the excitation particle (i.e., at the left end of the chain). If one excites a granular chain from a stationary state, the propagating waves include a wide range of frequencies near the excitation frequency. If the excitation frequency is close to the cutoff frequency, then incident waves whose frequencies are larger than the cutoff frequency will not propagate but will instead be localized at the excitation particle in the form of evanescent waves. Such perturbations result in transience in the form of propagating waves, often in modulated waveforms in the time domain. This, in turn, affects the calculation of transmission coefficients in numerical simulations and experiments. In both cases, we examine the dynamics in subsets of the chains for small propagation times to avoid the effects of reflection from the right boundary.

Appendix C

TRANSPORT ON DISORDERED GRANULAR CRYSTALS: EXPERIMENTAL RESULTS

In this Appendix, we show experimental results on transport in disordered granular crystals. The experimental setup in Figure C.1. The granular chain consists of 32 spherical particles, which results to be long enough to validate energy localization and transport properties in granular crystals. To introduce disorder to a granular crystal, we use various combinations of aluminum and tungsten-carbide particles, which have drastic disparities in density and elastic modulus. The right end of the chain is constrained by a steel plate with a hole in the center; through this hole, a spherical impactor released from a ramp hits and excites the first particle of the chain. The left end of the chain is blocked by a large sliding mass, which applies a static precompression F_0 to the chain through a linear spring. We measure the dynamics of the chain by recording each particle's velocity as a function of time via a laser Doppler vibrometer (LDV).

In the homogeneous chain, we observe a localized wave packet in the form of a strongly nonlinear solitary wave in the absence of precompression (i.e., for $F_0 = 0$ N). When we apply a nonzero precompression to the chain, we start to observe the generation of linear oscillatory waves, which propagate behind

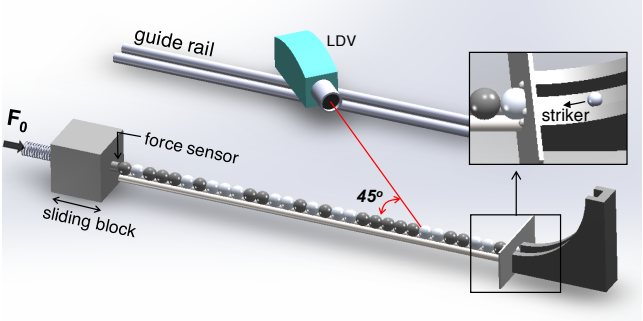


Figure C.1: Schematic of the experimental setup. The inset shows details of the boundary condition in the front of a granular chain.

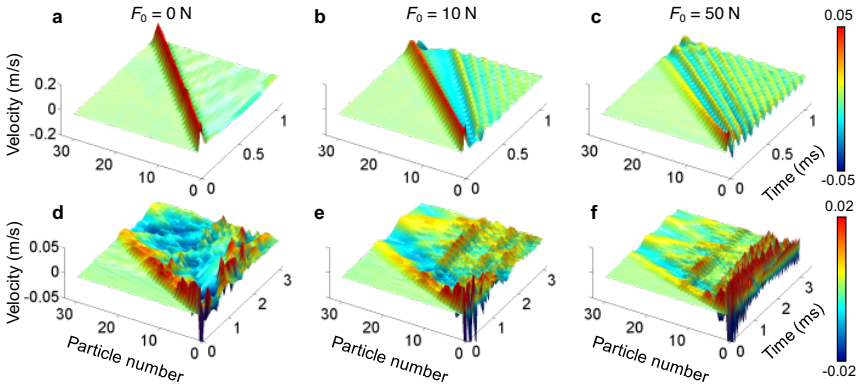


Figure C.2: Wave propagation in homogeneous and disordered chains. Spatiotemporal distributions of particle velocities in (a–c) a homogeneous chain and (d–f) a disordered chain with static precompressions of (a, d) 0 N, (b, e) 10 N, and (c, f) 50 N.

the supersonic leading nonlinear wave packet. These ripples arise from oscillations of the first particle after an impact and consequently from the excitation of oscillatory modes. The frequency of these oscillatory waves increases as the precompression increases (compare Figures C.2b and C.2c), as the contact stiffness increases with strong precompression because of the nonlinearity in the contact interaction.

In Figure C.2d–f, we show experimental results for wave propagation in a disordered chain for various precompression strengths. Comparing our results for disordered chains with the ones from the homogeneous chain, we find that the presence of disorder causes significant scattering of propagating waves in both time and space. The scattering is most drastic in the absence of precompression (see Figure C.2d). However, for increased precompression, the wave packet tends to become more localized in the front of the chain and the amplitude of propagating waves decrease significantly as a function of distance (see Figures C.2f).

To characterize the localization phenomenon near the excitation point in the linear regime (i.e., $F_0 = 50$ N), we compute the kinetic-energy distribution. Given the velocity $v_i(t)$ of the ith particle, we compute its kinetic energy $K_i(t) = (1/2)m_i v_i^2(t)$, where m_i is the particle's mass. We then average our results over the different realizations of disorder, obtaining $\langle K_i(t)\rangle$. Initially, the pattern's amplitude decreases due to the spreading associated with non-scattered modes. It then oscillates near the edge of the chain for a long time (up to 3.5 ms). To better visualize the kinetic-energy profile, we compute a temporal mean between $t_s = 1.5$ ms and $t_f = 3.5$ ms. We define the mean kinetic energy as $\bar{K}_i = \int_{t_s}^{t_f} \langle K_i(t)\rangle \, dt/(t_f - t_s)$, and we then normalize the distribution by letting $\bar{K}_i \to \bar{K}_i / \sum_{j=1}^{N} \bar{K}_j$. In Figure C.3, we show normalized mean kinetic energy profiles for the different precompression strengths. In our experiments, we observe for $F_0 = 50$ N that the kinetic-energy distribution decays at a roughly exponential rate: $\bar{K}_i \propto e^{-0.54i}$ for $i \in \{2, \ldots, 10\}$ (see the inset of Figure C.3). Due to this exponential decay, the kinetic energy is reduced by two orders of magnitude over

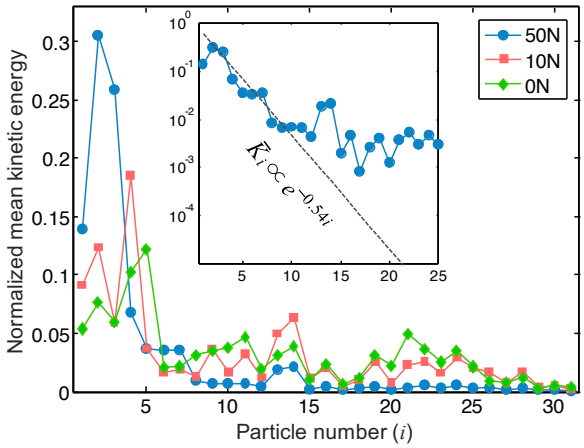


Figure C.3: Experimental observation of Anderson-like localization. Normalized kinetic energy profile, averaged between 1.5 ms and 3.5 ms, for different levels of precompression. In the inset, we show the kinetic energy on a logarithmic scale when the static precompression is 50 N. The dashed line shows the slope associated with $e^{-0.54i}$, where i denotes particle number.

a range of about 10 sites of the chain. We also observe localization around the second particle. This particular location arises from a combination of dissipation effects and the particular disordered configurations that we examine (a sub-ensemble in which the first particle is always aluminum). We have observed numerically that for the sub-ensemble in which the first particle is tungsten-carbide, the localization phenomenon instead tends to occur around the first particle. For $i \in \{11, \ldots, 15\}$, we observe the excitation of a secondary mode that emerges and decays in an irregular manner as function of time (see Figure C.3). For $i \gtrapprox 15$, very low-amplitude waves, which are associated primarily with low-frequency linear modes, reach the right side of the chain and are reflected.

To investigate the energy transport characteristics of the granular chains, we quantify energy localization and the speed of energy spreading using the inverse participation ratio (P^{-1}) and the second moment of the energy (m_2), respectively. To calculate these quantities, we use the kinetic energy instead of the total energy of the particles in a chain, because we can directly calculate the former experimentally by measuring particle velocities. The P^{-1} based on the

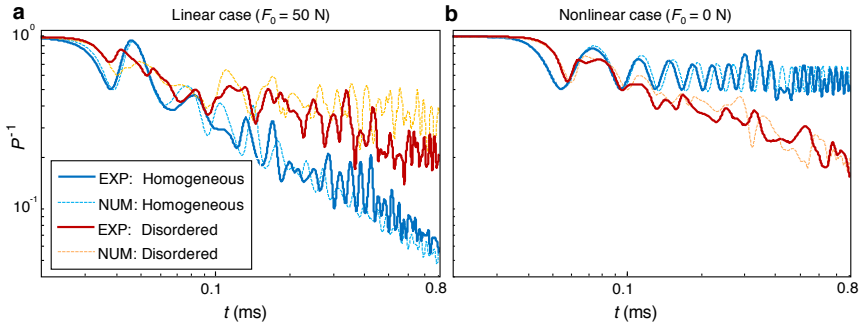


Figure C.4: Inverse participation ratio (P^{-1}) of the kinetic energy in homogeneous (blue curves) and disordered (red curves) chains for (a) linear and (b) nonlinear regimes. In both cases, we compare numerical calculations (dashed curves) with experimental data (solid curves).

kinetic energy is

$$P^{-1}(t) = \frac{\sum_{i=1}^{N} \left(m_i v_i^2\right)^2}{\left(\sum_{i=1}^{N} m_i v_i^2\right)^2}. \tag{C.1}$$

When all energy is confined to a single particle, $P^{-1} = 1$, and P^{-1} approaches $1/N$ (where N is the total number of particles in a chain) as a wave disperses. In Figure C.4, we show P^{-1} as a function of time in both the linear and nonlinear regimes. Because of the customary exchange between kinetic and potential energies, we observe oscillations in the temporal profile of P^{-1}.

In a homogeneous chain with precompression (solid blue curve in Figure C.4a), we observe experimentally that P^{-1} decreases in time, because the linear waves disperse as they propagate. However, in a disordered chain (solid red curve in Figure C.4a), this decreasing trend is less pronounced. This implies that the disorder tends to favor wave localization, confirming the effect of Anderson localization. Our numerical simulations corroborate the experimental results. Strikingly, we observe completely different qualitative behavior in the nonlinear regime (see Figure C.4b). The nonlinearity favors wave localization in a homogeneous chain, as indicated by the higher value P^{-1}. In this case, a localized solitary wave propagates in a highly localized manner, and P^{-1} retains a value of 0.6.

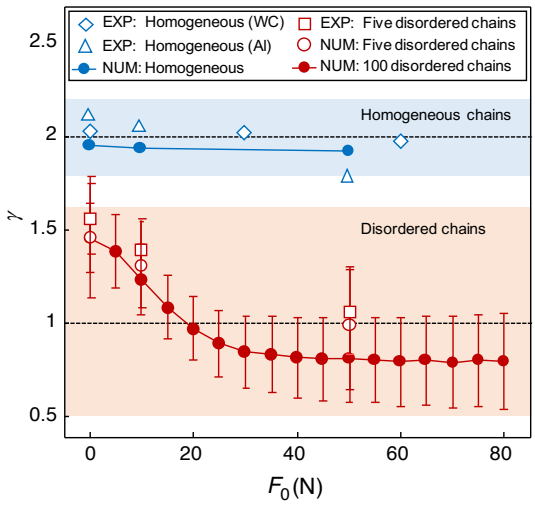


Figure C.5: Exponents (γ) of the second moment m_2 of kinetic energy as a function of precompression strength. The exponents 1 and 2 (horizontal dashed lines) represent diffusive and ballistic transport, respectively. The diamond, triangular, and square marks are based on experimental data obtained, respectively, from a homogeneous tungsten-carbide (WC) chain, a homogeneous aluminum (Al) chain, and a mean over five disordered chains. We mark the numerical data with circles. We do computations for homogeneous chains (blue circles), the five disordered chains (hollow red circles), and 100 randomly generated disordered chains (red circles with error bars).

We obtain the second moment of kinetic energy distribution by calculating

$$m_2(t) = \frac{\sum_{i=1}^{N} i^2 \left(m_i v_i^2\right)}{\sum_{i=1}^{N} m_i v_i^2} \,. \tag{C.2}$$

It is well-known that asymptotic energy spreading in a homogeneous chain is ballistic (i.e., $m_2(t) \sim t^2$ as $t \to \infty$). To investigate energy spreading in detail, we estimate the exponent γ of the second moment in the scaling relationship $m_2(t) \sim t^\gamma$ during the time period from 0.1 ms to 1 ms. We compare the estimated exponents from the experimental data to those from numerical simulations in Figure C.5. The exponents in homogeneous chains (the upper shaded area in Figure C.5a) are about $\gamma = 2$ (corresponding to ballistic spreading). For larger precompression, the exponents are slightly smaller, but they remain near the ballistic regime.

For disordered chains, we observe drastic changes in γ as we increase F_0. Specifically, the mean values of the exponents for the disordered chains diminish gradually from superdiffusive ($1 < \gamma < 2$) to subdiffusive ($0 < \gamma < 1$) for chains with progressively stronger static precompressions. This is remarkably more noticeable in our numerical simulations than in the experimental data, where in the later we observe an average value for γ slightly above subdiffusion. This difference between experiments and simulations is arguable in terms of the number of samples and consequently the superior statistic in the simulations. Our experimental results (red squares) corroborate our numerical computations (red circles).

Appendix D

DRIVEN DAMPED MAGNETIC CHAINS

In this Appendix, we consider a chain of dipolar magnets under the effects of a external magnetic field and intrinsic dissipations. Although this system is not physically equivalent to a granular crystal, we show that its equations of motion are in the same category of FPU-like chains. An advantage of working with magnetic chains compare with granular chains is that it results easier to introduce perturbations in the bulk of the system, by means of an external magnetic field, however the dynamics is a bit more complicated because the magnetic interaction has long-range, thus different properties for the linear and nonlinear waves are expected [7, 37, 114].

D.1 Equations of motion

Under driving and damping effects, the equation of motion for the magnets can be written as

$$M_n\ddot{u}_n = \sum_{n'<n} V'(u_n - u_{n'}) - \sum_{n'>n} V'(u_{n'} - u_n) - \eta\dot{u}_n + F(u_n, t)\,, \qquad \text{(D.1)}$$

where F represents an external magnetic force acting over the magnets, so in general it can depend parametrically on the displacement u_n of each magnet and also on t. η is the dissipation parameters, and for the sake of simplicity dissipation affects the magnets proportional to their speed. V is the potential

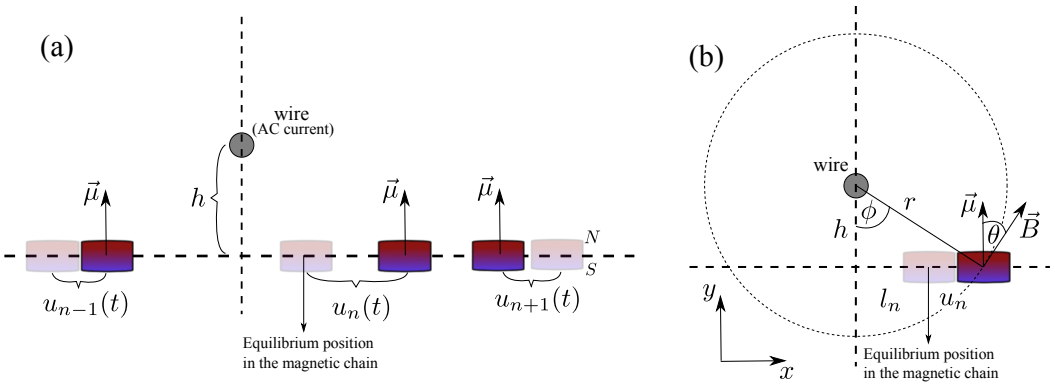


Figure D.1: (a) Scheme for the chain of magnets. (b) Scheme for the interaction between the magnetic field generated by the current on the wire and the magnets in the chain.

associated to the dipolar interaction. The way how we introduce an external magnetic field is by means of an AC current running over a wire, which is placed above the chain and orthogonal to the magnets (see Fig. D.1), thus its interaction with the chain of magnets can be considered as a periodic driving at the the frequency of the AC current. The precise form of the interaction will be discussed in the following section. Eq. (D.1) for $\eta = 0$ and $F = 0$ is remarkable similar to equations present in granular crystals. The main differences are the specific form of V, which differs only by a exponent from granular crystals, and also because the interaction is through magnetic fields, then we consider long-range effects instead of nearest neighbors interaction.

As we assume the magnets as magnetic dipoles, then the leading order in the interaction between the external magnetic field and the magnetic moment generated by the dipoles will dipole-dipole. A standard way to model the interaction between the magnetic moment generated by the current and the magnets is

$$\vec{F}_l = \nabla \left(\vec{\mu} \cdot \vec{B} \right) . \tag{D.2}$$

If we consider the magnetic moment as $\vec{\mu} = (0, m, 0)$ and the external field $\vec{B} = (B_x(x, y), B_y(x, y), 0)$, then the force (D.2) can be written as

$$\vec{F}_l = m \left(\partial_x B_y, \partial_y B_y, 0 \right) . \tag{D.3}$$

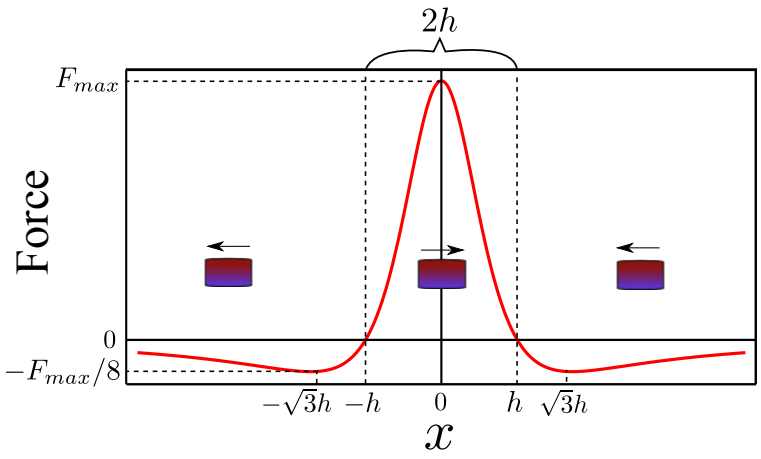


Figure D.2: Magnetic driving.

Following the scheme from Fig. D.1(b) and considering the magnet position in the xy-plane relative to the wire as $(x, y) = (l_n + u_n, -h)$, then the components of the magnetic field can be written as

$$\begin{aligned} B_x &= \frac{\alpha(t)\sin\theta}{r} = \frac{\alpha(t)y}{x^2+y^2}\,, \\ B_y &= \frac{\alpha(t)\cos\theta}{r} = \frac{\alpha(t)x}{x^2+y^2}\,, \end{aligned}$$

thus, the force, which is acting over the magnet, will be

$$\begin{aligned} \vec{F}_l &= \frac{m\alpha(t)}{\left(x^2+y^2\right)^2}\left(y^2-x^2,-2xy,0\right)\Big|_{x=l_n+u_m,\,y=-h}\,, \\ &= \frac{m\alpha(t)}{\left((l_n+u_n)^2+h^2\right)^2}\left(h^2-(l_n+u_n)^2,2h(l_n+u_n),0\right)\,. \end{aligned} \tag{D.4}$$

In our setup, we consider an oscillatory driving, which implies that $\alpha(t)$ oscillates, in particular with consider that oscillates as $\cos(\omega t)$ on time, in this way, we can write

$$\begin{aligned} M_n\ddot{u}_n &= \sum_{n'<n} A(\delta_0+u_n-u_{n'})^p - \sum_{n'>n} A(\delta_0+u_{n'}-u_n)^p \\ &\quad -\eta\dot{u}_n + m\alpha(t)\frac{h^2-(l_n+u_n)^2}{\left((l_n+u_n)^2+h^2\right)^2}\,. \end{aligned} \tag{D.5}$$

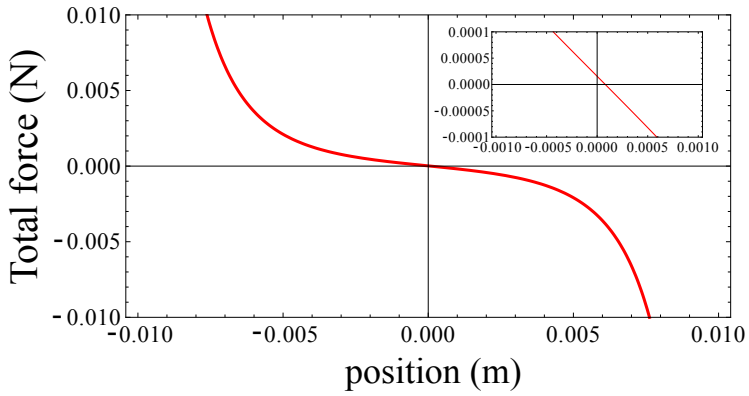


Figure D.3: Total force at $t = 0$ over a magnet with equilibrium position (before driving) exactly below to the wire and between two fixed magnets positioned at $x = -\delta_0$ and $x = \delta_0$.

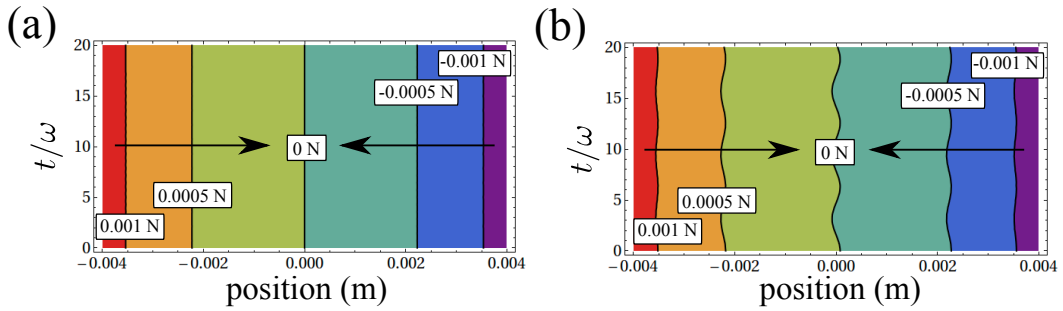


Figure D.4: Force map as a function of time and the position for a magnet between two fixed magnets positioned at $x = -\delta_0$ and $x = \delta_0$. (a) Hamiltonian case. (b) Forced case.

D.2 Physical quantities and estimation of the magnitude of the interactions

We consider a current $I(t) = I_0 \cos(\omega t)$, so the magnetic field takes the form

$$\vec{B} = \frac{\mu_0 I_0}{2\pi r} \cos(\omega t)\hat{\phi} = \frac{\alpha(t)}{r}\hat{\phi}\,. \tag{D.6}$$

Thus, the maximum driven on Eq. (D.5) will be given when the magnet pass just below the wire and it magnitude will be

$$F_{max} = \frac{m\mu_0 I_0}{2\pi h^2}\,. \tag{D.7}$$

Now, if we consider realistic values for the physical parameters: $m = 7.8 \times 10^{-3}\,[\mathrm{A\,m^2}]$, $I_0 = 1\,[\mathrm{A}]$, $h = 0.01\,[\mathrm{m^2}]$, and the vacuum permeability $\mu_0 = 4\pi \times 10^{-7}\,\left[\mathrm{N\,A^{-2}}\right]$, then the maximum value for the force is $F_{max} = 1.56 \times 10^{-5}\,[\mathrm{N}]$. Figure D.2 shows how the force decays as a function of the relative distance between the magnets and the wire.

On the other hand, the force between magnets is given by

$$V'(x) = A(\delta_0 + x)^p \tag{D.8}$$

where the experimental values for the parameters are: $A = e^{-27.181}\,[\mathrm{N\,m^{-}}^p]$, $\delta_0 = 0.337/24\,[m]$, and $p = -4.473$.

In order to illustrate how the external driving affects the dynamics, we study a simple configuration with only one magnet free and we consider its equilibrium position just below the wire. We also place two fixed magnets at distances $\pm\delta_0$ relative to the equilibrium of the free magnet. When the external driving is turned on, the equilibrium position of the free magnet changes in a periodic way, with frequency ω. In figures D.3 and D.4, we show, respectively, the total force for this configuration at $t = 0$ and as a function of time. From here we can see, for the current experimental parameters, that the interval where the external force has some effect over the free magnet is approximately $(-2, 2)$ mm around the equilibrium position of the unperturbed case.

Bibliography

[1] E. Abrahams. *50 Years of Anderson Localization.* World Scientific Publishing Co., 2010.

[2] V. Achilleos, G. Theocharis, and Ch. Skokos. Energy transport in one-dimensional disordered granular solids. *PRE*, 93:022903, 2016.

[3] P. W. Anderson. Absence of Diffusion in Certain Random Lattices. *Phys. Rev.*, 109:1492, 1958.

[4] J. F. R. Archilla, R. S. Mackay, and J. L. Marin. Discrete breathers and Anderson modes: two faces of the same phenomenon? *Physica D*, 134:406, 1999.

[5] S. Aubry and G. André. Analyticity Breaking and Anderson Localization in Inconmmensurate Lattices. *Ann. Israel Phy. Soc.*, 3:133, 1980.

[6] C. Aullbach, A. Wobst, G-L. Ingold, P. Hänggi, and I. Varga. Phase-space visualization of a metal-insulator transition. *New J. Phys.*, 6:70, 2004.

[7] C. Baesens and R. S. MacKay. Algebraic localisation of linear response in a network with algebraically decaying interaction, and application to breathers in dipole-dipole networks. *Helv. Phys. Acta*, 72:23, 1999.

[8] J. Billy, V. Josse, Z. Zuo, A. Bernard, B. Hambrecht, P. Lugan, D. Clément, L. Sanchez-Palencia, P. Bouyer, and A. Aspect. Direct Observation of Anderson Localization of Matter Waves in a Controlled Disorder. *Nature*, 453:891, 2008.

[9] L. Bindi, PJ. Steinhardt, Yao, N., and PJ. Lu. Natural quasicrystals. *Science*, 324:1306, 2009.

[10] N. Boechler, G. Theocharis, S. Job, P. G. Kevrekidis, M. A. Porter, and C. Daraio. Discrete Breathers in One-Dimensional Diatomic Granular Crystals. *Phys. Rev. Lett.*, 104:244302, 2010.

[11] N. Boechler, J. Yang, G. Theocharis, P. G. Kevrekidis, and C. Daraio. Tunable Vibrational Band Gaps in One-Dimensional Diatomic Granular Crystals with Three-Particle Unit Cells. *J. App. Phys.*, 109:074906, 2011.

[12] L. Bonanomi, G. Theocharis, and C. Daraio. Wave propagation in granular chains with local resonances. *Phys. Rev. E*, 91:033208, 2015.

[13] W. Cai, U. K. Chettiar, A. V. Kildishev, and V. M. Shalaev. Optical Cloaking with Metamaterials. *Nat. Photon.*, 1:224, 2007.

[14] D. K. Campbell, S. Flach, and Yu. S. Kivshar. Localizing Energy Through Nonlinearity and Discreteness. *Phys. Today*, 57(1):43, 2004.

[15] R. Carretero-González, D. Khatri, M. A. Porter, P. G. Kevrekidis, and C. Daraio. Dissipative Solitary Waves in Granular Crystals. *Phys. Rev. Lett.*, 102:024102, 2009.

[16] A. C. Cassidy, D. Mason, V. Dunjko, and M. Olshanii. Threshold for Chaos and Thermalization in the One-Dimensional Mean-Field Bose–Hubbard Model. *Phys. Rev. Lett.*, 102:025302, 2009.

[17] A.-L. Chen and Y.-S. Wang. Study on Band Gaps of Elastic Waves Propagating in One-Dimensional Disordered Phononic Crystals. *Physica B*, 392:369, 2007.

[18] H. Chen and C. T. Chan. Acoustic Cloaking in Three Dimensions Using Acoustic Metamaterials. *Appl. Phys. Lett.*, 91:183518, 2007.

[19] C. Chong, F. Li, J. Yang, M. O. Williams, I. G. Kevrekidis, P. G. Kevrekidis, and C. Daraio. Damped-Driven Granular Chains: An Ideal Playground for Dark Breathers and Multibreathers. *Phys. Rev. E*, 89:032924, 2014.

[20] C. Chong, MA. Porter, PG. Kevrekidis, and C. Daraio. Nonlinear coherent structures in granular crystals. *J. Phys.: Condens. Matter*, 29:413003, 2017.

[21] C. Conti and A. Fratalocchi. Dynamic Light Diffusion, Three-Dimensional Anderson Localization and Lasing in Inverted Opals. *Nat. Phys.*, 4:794, 2008.

[22] C. Coste, E. Falcon, and S. Fauve. Solitary Waves in a Chain of Beads under Hertz Contact. *Phys. Rev. E*, 56:6104, 1997.

[23] A. Crisanti, G. Paladin, and A. Vulpiani. *Products of Random Matrices*. Springer, 1993.

[24] C. Daraio, V. F. Nesterenko, E. B. Herbold, and S. Jin. Energy Trapping and Shock Disintegration in a Composite Granular Medium. *Phys. Rev. Lett.*, 96:058002, 2006.

[25] C. Daraio, V. F. Nesterenko, E. B. Herbold, and S. Jin. Tunability of Solitary Wave Properties in One-Dimensional Strongly Nonlinear Photonic Crystals. *Phys. Rev. E*, 73:026610, 2006.

[26] C. Daraio, V. F. Nesterenko, and S. Jin. Strongly Nonlinear Waves in a Chain of Teflon Beads. *Phys. Rev. E*, 72:016603, 2005.

[27] P. K. Datta and K. Kundu. Energy Transport in One-Dimensional Harmonic Chains. *Phys. Rev. B*, 51:6287, 1995.

[28] CR. Dean, L. Wang, P. Maher, C. Forsythe, F. Ghahari, Y. Gao, J. Katoch, M. Ishigami, P. Moon, M. Koshino, T. Taniguchi, K. Watanabe,

KL. Shepard, J. Hone, and P. Kim. Hofstadter's butterfly and the fractal quantum Hall effect in moiré superlattices. *Nature*, 497:598, 2013.

[29] R. Doney and S. Sen. Decorated, Tapered, and Highly Nonlinear Granular Chain. *Phys. Rev. Lett.*, 97:155502, 2006.

[30] D. H. Dunlap, H-L Wu, and P. W. Phillips. Absence of Localization in a Random-Dimer Model. *Phys. Rev. Lett.*, 65:88, 1990.

[31] N. K. Efremidis and K. Hizanidis. Disordered Lattice Solitons. *Phys. Rev. Lett.*, 101:143903, 2008.

[32] D. Hutchins et al. Evolution of ultrasonic impulses in chains of spheres using resonant excitation. *Europhys Lett*, 109:54022, 2015.

[33] D. Hutchins et al. Generation of impulses from single frequency inputs using nonlinear propagation in spherical chains. *Physics Proc*, 70:131 – 134, 2015.

[34] J. Yang et al. Analysis of solitary wave impulses in granular chains using ultrasonic excitation. *Physical Review E*, 93:063002, 2016.

[35] K. Falconer. *Fractal geometry: mathematical foundations and applications.* 1990.

[36] E. Fermi, J. Pasta, and S. Ulam. Studies of Nonlinear Problems. i. *(Los Alamos National Laboloratory, Los Alamos, N. M.)*, Tech. Rep.:LA–1940, 1955.

[37] S. Flach. Breathers on lattices with long range interaction. *Phys. Rev. E*, 58:R4116, 1998.

[38] S. Flach. Nonlinear Lattice Waves in Random Potentials. In C. Besse and J. C. Garreau, editors, *Nonlinear Optical and Atomic Systems*, volume 2146 of *Lecture Notes in Mathematics*, page 1. Springer, 2015.

[39] S. Flach and A. Gorbach. Discrete Breathers: Advances in Theory and Applications. *Phys. Rep.*, 467:1, 2008.

[40] S. Flach, M. Ivanchenko, and R. Khomeriki. Correlated metallic two-particle bound states in quasiperiodic chains. *EPL*, 98:66002, 2012.

[41] F. Fraternali, M. A. Porter, and C. Daraio. Optimal Design of Composite Granular Protectors. *Mech. Adv. Mat. Struct.*, 17(1):1, 2010.

[42] I. Garcia-Mata and D. L. Shepelyansky. Delocalization Induced by Nonlinearity in Systems with Disorder. *Phys. Rev. E*, 104:103904, 2009.

[43] F. A. Gianturco and D. G. Thompson. The Ramsauer–Townsend Effect in Methane. *J. Phys. B: Atom. Molec. Phys.*, 9:L383, 1976.

[44] D. E. Golden and H. W. Bandel. Low-Energy e^-–ar Total Scattering Cross Sections: The Ramsauer–Townsend Effect. *Phys. Rev.*, 149:58, 1966.

[45] M. Goldstein, W. Schlag, and M. Voda. On the spectrum of multi-frequency quasiperiodic Schrödinger operators with large coupling. *arXiv*, 1708:09711, 2017.

[46] B. Grémaud and T. Wellens. Speckle Instability: Coherent Effects in Nonlinear Disordered Media. *Phys. Rev. Lett.*, 104:133901, 2010.

[47] DR. Grempel, S. Fishman, and RE. Prange. Localization in an incommensurate potential: An exactly solvable model. *PRL*, 49:833, 1982.

[48] V. Gurarle, G. Rafael, and J. T. Chalker. Excitations of One-Dimensional Bose–Einstein Condensates in a Random Potential. *Phys. Rev. Lett.*, 101:170407, 2008.

[49] U. Harbola, A. Rosas, A. H. Romero, M. Esposito, and K. Lindenberg. Pulse Propagation in Decorated Granular Chains: An Analytical Approach. *Phys. Rev. E*, 80:051302, 2009.

[50] E. Hascoet and H. J. Herrmann. Shocks in Non-Loaded Bead Chains with Impurities. *Eur. Phys. J. B*, 14:183, 2000.

[51] M. Heinrich, R. Keil, Y. Lahini, U. Naether, F. Dreisow, A. Tünnermann, S. Nolte, and A. Szameit. Disorder-Enhanced Nonlinear Delocalization in Segmented Waveguide Arrays. *New J. Phys.*, 14:073026, 2012.

[52] E. B. Herbold, J. Kim, V. F. Nesterenko, S. Y. Wang, and C. Daraio. Pulse Propagation in a Linear and Nonlinear Diatomic Periodic Chain: Effects of Acoustic Frequency Band-Gap. *Acta Mechanica*, 205:85, 2009.

[53] E.J. Hinch and S. Saint-Jean. The Fragmentation of a Line of Balls by an Impact. *Proc. R. Soc. Lond. A*, 455:3201, 1999.

[54] D.R. Hofstadter. Energy levels and wavefunctions of bloch electrons in rational and irrational magnetic fields. *Phys. Rev. B*, 14:2239, 1976.

[55] J. Hong. Universal Power-Law Decay of the Impulse Energy in Granular Protectors. *Phys. Rev. Lett.*, 94:108001, 2005.

[56] J. Hong and A. Xu. Nondestructive Identification of Impurities in Granular Medium. *Appl. Phys. Lett.*, 81:4868, 2002.

[57] C. Hoogeboom, G. Theocharis, and P. G. Kevrekidis. Discrete Breathers at the Interface between a Diatomic and a Monoatomic Granular Chain. *Phys. Rev. E*, 82:061303, 2010.

[58] H. Hu, A. Strybulevych, J. H. Page, S. E. Skipetrov, and B. A. Van Tiggelen. Localization of Ultrasound in a Three-Dimensional Elastic Network. *Nat. Phys.*, 4:945, 2008.

[59] H. Huang, C. Sun, and G. Huang. On the negative effective mass density in acoustic metamaterials. *Ing. J. Eng. Sci.*, 47:4, 2009.

[60] D.A. Hutchins, J. Yang, O. Akanji, P.J. Thomas, L.A.J. Davis, S. Freear, S. Harput, N. Saffari, and P. Gelat. Ultrasonic propagation in finite-length granular chains. *Ultrasonics*, 69:215 – 223, 2016.

[61] S. Iyer, V. Oganesyan, G. Refael, and DA. Huse. Many-body localization in a quasiperiodic system. *Phys. Rev. B*, 87:134202, 2013.

[62] G. James. Nonlinear waves in Newton's cradle and the discrete p-Schrödinger equation. *Math. Models methods Appl. Sci.*, 21:2335, 2011.

[63] G. James, P.G. Kevrekidis, and J. Cuevas. Breathers in oscillator chains with hertzian interactions. *Physica D*, 251:39, 2013.

[64] C. Janot. *Quasicrystals: A Primer. 2nd edition.* 1994.

[65] K. R. Jayaprakash, Y. Starosvetsky, A. F. Vakakis, and O. V. Gendelman. Nonlinear Resonances Leading to Strong Pulse Attenuation in Granular Dimer Chains. *Journal of Nonlinear Science*, 23:363, 2013.

[66] K. R. Jayaprakash, Yuli Starosvetsky, and Alexander F. Vakakis. New Family of Solitary Waves in Granular Dimer Chains with no Precompression. *Phys. Rev. E*, 83:036606, 2011.

[67] K. R. Jayaprakash, Alexander F. Vakakis, and Yuli Starosvetsky. Solitary Waves in a General Class of Granular Dimer Chains. *J. App. Phys.*, 112:034908, 2012.

[68] S. Job, F. Santibanez, F. Tapia, and F. Melo. Wave Localization in Strongly Nonlinear Hertzian Chains with Mass Defect. *Phys. Rev. E*, 80:025602(R), 2009.

[69] M. Johansson, G. Kopidakis, and S. Aubry. KAM Tori in 1D Random Discrete Nonlinear Schrödinger Model? *Europhys. Lett.*, 91:50001, 2010.

[70] K. L. Johnson. *Contact Mechanics.* Cambridge University Press, New York, 1987.

[71] W. E. Kauppila, T. S. Stein, and G. Jesion. Direct Observation of a Ramsauer–Townsend Effect in Positron–Argon Collisions. *Phys. Rev. Lett.*, 36:580, 1976.

[72] P. G. Kevrekidis. *The Discrete Nonlinear Schrödinger Equation: Mathematical Analysis, Numerical Computations and Physical Perspectives*. Springer-Verlag, New York, NY, 2011.

[73] P.G. Kevrekidis. Non-Linear Waves in Lattices: Past, Present, Future. *IMA J. Appl. Math.*, 76:389, 2011.

[74] P.G. Kevrekidis, A. Vainchtein, M. Serra Garcia, and C. Daraio. Interaction of traveling waves with mass-with-mass defects within a hertzian chain. *Phys. Rev. E*, 87:042911, 2013.

[75] D. Khatri, D. Ngo, and C. Daraio. Highly Nonlinear Solitary Waves in Chains of Cylindrical Particles. *Granular Matt.*, 14:63, 2012.

[76] D. Khatri, P. Rizzo, and C. Daraio. Highly Nonlinear Waves' Sensor Technology for Highway Infrastructures. *SPIE*, 6934:69340U, 2008.

[77] E. Kim, F. Li, C. Chong, G. Theocharis, J. Yang, and P.G. Kevrekidis. Highly nonlinear wave propagation in elastic woodpile periodic structures. *Phys. Rev. Lett.*, 114:118002, 2015.

[78] E. Kim, A.J. Martínez, SE. Phenisee, P.G. Kevrekidis, M.A. Porter, and J. Yang. Direct measurement of superdiffusive energy transport in disordered granular chains. *Nat. Commun.*, 9:640, 2018.

[79] G. Kopidakis, S. Komineas, S. Flach, and S. Aubry. Absence of Wave Packet Diffusion in Disordered Nonlinear Systems. *Phys. Rev. Lett.*, 100:084103, 2008.

[80] B. Kramer and A. MacKinnon. Localization: Theory and Experiment. *Rep. Prog. Phys.*, 56:1469, 1993.

[81] B. Kramer and A. MacKinnon. Localization: Theory and experiment. *Rep. Prog. Phys.*, 56:1469, 1993.

[82] YE. Kraus and O. Zilberberg. Topological equivalence between the Fibonacci quasicrystal and the Harper model. *PRL*, 109:116404, 2012.

[83] U. Kuhl and H-J. Stöckmann. Microwave realization of the Hofstadter butterfly. *Phys. Rev. Lett.*, 80:3232, 1998.

[84] V. N. Kuzovkov. The Anderson Localization Problem, the Fermi-Pasta-Ulam Paradox and the Generalized Diffusion Approach. *Phys. Scr.*, 84:065002, 2011.

[85] Y. Lahini, R. Pugatch, F. Pozzi, M. Sorel, R. Morandotti, N. Davidson, and Y. Silberberg. Observation of a Localization Transition in Quasiperiodic Photonic Lattices. *Phys. Rev. Lett.*, 103:013901, 2009.

[86] L. D. Landau and E. M. Lifshitz. *Statistical Physics*. Oxford: Butterworth-Heinemann, 1980.

[87] T. V. Laptyeva, J. D. Bodyfelt, D. O. Krimer, Ch. Skokos, and S. Flach. The Crossover from Strong to Weak Chaos for Nonlinear Waves in Disordered Systems. *Europhys. Lett.*, 91:30001, 2010.

[88] T. V. Laptyeva, M. V. Ivanchenko, and S. Flach. Nonlinear Lattice Waves in Heterogeneous Media. *J. Phys. A: Math. Theor.*, 47:493001, 2014.

[89] T.V. Laptyeva, J.D. Bodyfelt, D.O. Krimer, Ch. Skokos, and S. Flach. The crossover from strong to weak chaos for nonlinear waves in disordered systems. *Europhys. Lett.*, 91:30001, 2010.

[90] TV. Laptyeva, MV. Ivanchenko, and S. Flach. Nonlinear lattice waves in heterogeneous media. *J. Phys. A*, 47:493001, 2014.

[91] J. Laskar and P. Robutel. High Order Sympletic Integrators for Perturbed Hamiltonian Systems. *Celest. Mech. Dyn. Astron.*, 80:39, 2001.

[92] A. N. Lazaridi and V. F. Nesterenko. Observation of a new type of solitary waves in one-dimensional granular medium. *J. Appl. Mech. Tech. Phys.*, 26:405, 1985.

[93] F. Lederer, G. I. Stegeman, D. N. Christodoulides, G. Assanto, M. Segev, and Y. Silberberg. Discrete Solitons in Optics. *Phys. Rep.*, 463:1, 2008.

[94] S. Lepri, R. Livi, and A. Politi. Heat Conduction in Chains of Nonlinear Oscillators. *Phys. Rev. Lett.*, 78:1896, 1997.

[95] S. Lepri, R. Livi, and A. Politi. Thermal Conduction in Classical Low-Dimensional Lattices. *Phys. Rep.*, 377:1, 2003.

[96] S. Lepri, R. Schilling, and S. Aubry. Asymptotic Energy Profile of a Wave Packet in Disordered Chains. *Phys. Rev. E*, 82:056602, 2010.

[97] D. Levine and PJ. Steinhardt. Quasicrystals: A new class of ordered structures. *PRL*, 53:2477, 1984.

[98] F. Li, P. Anzel, J. Yang, P. G. Kevrekidis, and C. Daraio. Granular Acoustic Switches and Logic Elements. *Nat. Comm.*, 5:5311, 2014.

[99] F. Li, C. Chong, J. Yang, P.G. Kevrekidis, and C. Daraio. Wave transmission in time- and space-variant helicoidal phononic crystals. *Phys. Rev. E*, 90:053201, 2014.

[100] F. Li, L. Zhao, Z. Tian, L. Yu, and J. Yang. Visualization of Solitary Waves via Laser Doppler Vibrometry for Heavy Impurity Identification in a Granular Chain. *Smart Mater. Struc.*, 22:035016, 2013.

[101] R. Lifshitz. Quasicrystals: A matter of definition. *Foundations of Physics*, 33:1703, 2003.

[102] L. Liu, G. James, P. Kevrekidis, and A. Vainchtein. Breathers in a locally resonant granular chain with precompression. *Physica D*, 331:27, 2016.

[103] L. Liu, G. James, P. Kevrekidis, and A. Vainchtein. Strongly nonlinear waves in locally resonant granular chains. *Nonlinearity*, 29:3496, 2016.

[104] B. Luk'yanchuk, N. I. Zheludev, S. A. Maier, N. J. Halas, P. Nordlander, H. Giessen, and C. T. Chong. The Fano Resonance in Plasmonic Nanostructures and Metamaterials. *Nat. Mater.*, 9:707, 2010.

[105] RS Mackay. Solitary waves in a chain of beads hertz contact. *Phys Lett A*, 251:191, 199.

[106] Y. Man, N. Boechler, G. Theocharis, P. G. Kevrekidis, and C. Daraio. Defect Modes in One-Dimensional Granular Crystals. *Phys. Rev. E*, 85:037601, 2012.

[107] A. J. Martínez, P. G. Kevrekidis, and M. A. Porter. Superdiffusive Transport and Energy Localization in Disordered Granular Crystals. *Phys. Rev. E*, 93:022902, 2016.

[108] A. J. Martínez and M. I. Molina. Surface Solitons in Quasiperiodic Nonlinear Photonic Lattices. *Phys. Rev. A*, 85:013807, 2012.

[109] A. J. Martínez, H. Yasuda, E. Kim, P. G. Kevrekidis, M. A. Porter, and J. Yang. Scattering of Waves by Impurities in Granular Crystals. *Phys. Rev. E*, 93:052224, 2016.

[110] A.J. Martínez, M.A. Porter, and P.G. Kevrekidis. Quasiperiodic granular chains and Hofstadter butterflies. *Phil. Trans. R. Soc. A*, 376:20170139, 2018.

[111] V. Mastropietro. Localization of interacting fermions in the aubry–andré model. *PRL*, 115:180401, 2015.

[112] A. E. Miroshnichenko, S. Flach, and Yu. S. Kivshar. Fano Resonances in Nanoscale Structures. *Rev. Mod. Phys.*, 82:2257, 2010.

[113] A. E. Miroshnichenko and Y. S. Kivshar. Fano Resonances in All-Dielectric Oligoners. *Nano Lett.*, 12:6459, 2012.

[114] M. Molerón, C. Chong, A. J. Martínez, M. A. Porter, P. G. Kevrekidis, and C. Daraio. Nonlinear excitations in magnetic lattices with long-range interactions. *New J. Phys.*, 21:063032, 2019.

[115] A. Molinari and C. Daraio. Stationary Shocks in Periodic Highly Nonlinear Granular Chains. *Phys. Rev. E*, 80:056602, 2009.

[116] M. Mulansky, K. Ahnert, A. Pikovsky, and D. L. Shepelyansky. Dynamical Thermalization of Disordered Nonlinear Lattices. *Phys. Rev. E*, 80:056212, 2009.

[117] M. Mulansky and A. Pikovsky. Energy Spreading in Strongly Nonlinear Disordered Lattices. *New J. Phys.*, 15:053015, 2013.

[118] U. Naether, A. J. Martínez, D. Guzmán-Silva, M. I. Molina, and R. A. Vicencio. Self-Trapping Transition in Nonlinear Cubic Lattices. *Phys. Rev. E*, 87:062914, 2013.

[119] U. Naether, C. Mejía-Cortés, and R. Vicencio. Pseudo-Two-Dimensional Random Dimer Lattices. *Phys. Lett. A*, 379:988, 2015.

[120] U. Naether, S. Rojas-Rojas, A. J. Martínez, S. Stützer, A. Tünnermann, S. Nolte, M. I. Molina, R. A. Vicencio, and A. Szameit. Enhanced Distribution of a Wave-Packet in Lattices with Disorder and Nonlinearity. *Opt. Express*, 21:927, 2013.

[121] V. F. Nesterenko. *Dynamics of Heterogeneous Materials*. 2001.

[122] V. F. Nesterenko, C. Daraio, E. B. Herbold, and S. Jin. Anomalous Wave Reflection at the Interface of Two Strongly Nonlinear Granular Media. *Phys. Rev. Lett.*, 95:158702, 2005.

[123] Roger G. Newton. *Scattering Theory of Waves and Particles, 2nd ed.* Dover Piblications Inc., USA, 2013.

[124] D. Ngo, D. Khatri, and C. Daraio. Highly Nonlinear Solitary Waves in Chains of Ellipsoidal Particles. *Phys. Rev. E*, 84:026610, 2011.

[125] National Institute of Standards and Technology. *Digital Library of Mathematical Functions (release 1.0.10).* Available at http://dlmf.nist.gov/, 2015.

[126] R. Penrose. Pentaplexity. *Eureka*, 39:16, 1978.

[127] A. S. Pikovsky and D. L. Shepelyansky. Destruction of Anderson Localization by a Weak Nonlinearity. *Phys. Rev. Lett.*, 100:094101, 2008.

[128] L Ponson, N Boechler, Y. M. Lai, M. A. Porter, P. G. Kevrekidis, and C. Daraio. Nonlinear Waves in Disordered Diatomic Granular Chains. *Phys. Rev. E*, 82:021301, 2010.

[129] V Popov. *Contact Mechanics and Friction.* Springer-Verlag, New York, NY, 2010.

[130] M. A. Porter, C. Daraio, E. B. Herbold, I. Szelengowicz, and P. G. Kevrekidis. Highly Nonlinear Solitary Waves in Periodic Dimer Granular Chains. *Phys. Rev. E*, 77:015601(R), 2008.

[131] M. A. Porter, C. Daraio, I. Szelengowicz, E. B. Herbold, and P. G. Kevrekidis. Highly Nonlinear Solitary Waves in Heterogeneous Periodic Granular Media. *Physica D*, 238:666, 2009.

[132] Mason A. Porter, Panayotis G. Kevrekidis, and Chiara Daraio. Granular Crystals: Nonlinear Dynamics Meets Materials Engineering. *Physics Today*, 68:44, 2015.

[133] William H. Press, Saul A. Teukolsky, William T. Vetterling, and Brian P. Flannery. *Numerical Recipes in C (2Nd Ed.): The Art of Scientific Computing*. Cambridge University Press, New York, NY, USA, 1992.

[134] K. Ø. Rasmussen, D. Cai, A. R. Bishop, and N. Grønbech-Jensen. Localization in a Nonlinear Disordered System. *Europhys. Lett.*, 47:421, 1999.

[135] G. Roati, C. D'Errico, L. Fallani, M. Fattori, C. Fort, M. Zaccanti, G. Modugno, M. Modugno, and M. Inguscio. Anderson Localization of Non-Interacting Bose–Einstein Condensate. *Nature*, 453:895, 2008.

[136] S. Rojas-Rojas, L. Morales-Inostroza, U. Naether, G.B. Xavier, S. Nolte, R.A. Szameit, R. Vicencio, G. Lima, and A. Delgado. Analytical model for polarization-dependent light propagation in waveguide arrays and applications. *Phys. Rev. A*, 90:063823, 2014.

[137] P. Roushan, C. Neill, J. Tangpanitanon, VM. Bastidas, A. Megrant, R. Barends, Z. Chen, Y. andd Chen, B. Chiaro, A. Dunsworth, A. Fowler, B. Foxen, M. Giustina, E. Jeffrey, J. Kelly, E. Lucero, J. Mutus, M. Neeley, C. Quintana, D. Sank, A. Vainsencher, J. Wenner, T. White, H. Neven, D.G. Angelakis, and J. Martinis. Spectroscopic signature of localization with interacting photons in superconducting qubits. *Science*, 358:1175, 2017.

[138] R.S. Mackay S. Kim, C. Baesens. Phonon scattering by localized equilibria of nearest neighbour chains. *Phys Rev E*, 56:R4955, 1997.

[139] J. J. Sakurai. *Modern Quantum Mechanics*. Addison Wesley, 1994.

[140] M. Schroeder. *Fractals, Chaos, Power Laws: Minutes from an Infinite Paradise*. 1991.

[141] T. Schwartz, G. Bartal, S. Fishman, and M. Segev. Transport and Anderson Localization in Disordered Two-Dimensional Photonic Lattices. *Nature*, 446:52, 2007.

[142] S. Sen, J. Hong, J. Bang, E. Avalos, and R. Doney. Solitary Waves in the Granular Chain. *Phys. Rep.*, 462:21, 2008.

[143] Surajit Sen, Marian Manciu, and James D. Wright. Solitonlike Pulses in Perturbed and Driven Hertzian Chains and their Possible Applications in Detecting Buried Impurities. *Phys. Rev. E*, 57:2386, 1998.

[144] Ch. Skokos, D. O. Krimer, S. Komineas, and S. Flach. Delocalization of Wave Packets in Disordered Nonlinear Chains. *Phys. Rev. E*, 79:056211, 2009.

[145] Ch. Skokos, D. O. Krimer, S. Komineas, and S. Flach. Erratum: Delocalization of Wave Packets in Disordered Nonlinear Chains [Phys. Rev. E 79, 056211 (2009)]. *Phys. Rev. E*, 89:029907, 2014.

[146] A. Sokolow and S. Sen. Exact Solution to the Problem of Nonlinear Pulse Propagation through Random Layered Media and its Connection with Number Triangles. *Ann. Phys.*, 322:2104, 2007.

[147] A. Spadoni and C. Daraio. Generation and Control of Sound Bullets with a Nonlinear Acoustic Lens. *Proc. Nat. Acad. Sci.*, 107(16):7230, 2010.

[148] Z. Sun, S. Fishman, and A. Soffer. Soliton Mobility in Disordered Lattice. *Phys. Rev. E*, 92:040903(R), 2015.

[149] I. Szelengowicz, M. A. Hasan, Y. Starosvetsky, A. Vakakis, and C. Daraio. Energy Equipartition in Two-Dimensional Granular Systems with Spherical Intruders. *Phys. Rev. E*, 87:032204, 2013.

[150] G. Theocharis, M. Kavousanakis, P. G. Kevrekidis, C. Daraio, M. A. Porter, and I. G. Kevrekidis. Localized Breathing Modes in Granular Crystals with Defects. *Phys. Rev. E*, 80:066601, 2009.

[151] Existence theorem for solitary waves on lattices. Localizing Energy Through Nonlinearity and Discreteness. *Commun. Math. Phys.*, 161:391, 1994.

[152] S. Tietsche and A. Pikovsky. Chaotic Destruction of Anderson Localization in a Nonlinear Lattice. *Europhys. Lett.*, 84:10006, 2008.

[153] L Vázquez, R. S. MacKay, and M. P. Zorzano. Localization and Energy Transfer in Nonlinear Systems. *Proceedings of the Third Conference*, World Sci., 2002.

[154] K. Vorotnikov, Y. Starosvetsky, G. Theocharis, and P.G. Kevrekidis. Wave propagation in a strongly nonlinear locally resonant granular crystal. *Physica D*, 365:27, 2018.

[155] H. Xu, P.G. Kevrekidis, and A. Stefanov. Traveling waves and their tails in locally resonant granular systems. *J. Phys. A*, 48:195204, 2015.

[156] B. Yousefzadeh and A. S. Phani. Supratransmission in a Disordered Nonlinear Periodic Structure. *J. Sound and Vibration*, 380:242, 2016.

[157] C. Yuce. PT Symmetric Aubry–Andre Model. *Phys. Lett. A*, 378:2024, 2014.

[158] S. S. Zakeri, S. Lepri, and D. S. Wiersma. Localization in One-Dimensional Chains with Lévy-Type Disorder. *Phys. Rev. E*, 91:032112, 2015.

[159] Y. Zhang, M. A. Hasan, Y. Starosvetsky, D. M. McFarland, and A. F. Vakakis. Nonlinear Mixed Solitary—Shear Waves and Pulse Equi-Partition in a Granular Network. *Physica D: Nonlinear Phenomena*, 291:45, 2015.